THE MODELLING OF GO_2/GH_2 FUEL TYPE PROPELLANT IN COAXIAL INJECTOR DYNAMICS AND COMBUSTION PROCESSES

Prepared by

Byron Parrott (781971)

7 August 2020

School of Mechanical, Aeronautical and
Industrial Engineering, Faculty of Engineering
and the Built Environment, University of the
Witwatersrand, Johannesburg, South Africa

Supervisor:

Professor Craig Law (University of the Witwatersrand)

A dissertation submitted to the Faculty of Engineering and the Built Environment, University of Witwatersrand, in fulfilment of the requirements of the degree of Masters of Science in Mechanical Engineering

Declaration

I declare that this dissertation is my own unaided work except where acknowledged and referenced. It is being submitted to the Faculty of Engineering and the Built Environment, University of Witwatersrand, in fulfilment of the requirements of the degree of Masters of Science in Mechanical Engineering. It has not been submitted before for any degree or examination at any other university.

Byron Parrott

Acknowledgements

I would like to thank God for getting me to this point in my life safely according to His will. I would like to thank Professor Law for giving me this opportunity and the continuous guidance through extremely difficult times in my life. I would like to thank him for having faith in me throughout the process. I would like to thank Christiaan de Wet at Aerotherm for the training and willingness to always assist through all the simulation challenges. I would like to thank him for his patience and insight into CFD applications. I would like to thank Randall Paton for allowing me access to the Centre for High Performance Computing that allowed me the processing power to reduce the computational time significantly of all the investigated cases.

I would like to thank my family for the continuous support and pushing me to limits I never knew existed in me. And finally I would like to thank my wife Kherisha, without whom none of this study would be possible. Her love, support and unwavering faith in me has been my constant reminder that I am more than what I have become and is my inspiration to continuously strive to be better.

Abstract

A study has been conducted that involved the modelling of gaseous oxygen – gaseous hydrogen propellants in a single element coaxial injector. The fluid flow domain and combustion dynamics were investigated to determine the key design parameters. The study investigated the optimisation of the key design parameters to improve the injector performance in terms of combustion length and combustion efficiency. The numerical model captured the complex chemical combustion interactions and gas mixture variations in the combustion chamber. Mixing in the numerical model was achieved by the shear layer development between the propellants. The flame anchored in the head end region, where the axial distance is less than 0.1m directly influence the combustion length which was used to evaluate the injector performance. High turbulence intensity was developed in the head end region while combustion products were routed to the combustion chamber wall. The turbulent eddy currents that were developed are responsible for the fluid motion and consequently energy transfer to enhance mixing and the combustion process. At the combustion chamber wall heat is transferred from the hot gas mixture to the wall. The species, temperature and velocity non-uniformity in the axial direction produces the various distributions that were used for model comparison. The modelling of the phenomenon poses challenges that include grid resolution, turbulence modelling, chemical kinetic modelling and wall boundary layer modelling: all of which influence the accuracy of the predicted heat flux. A base case numerical solution was developed and compared to a physical model result. It was found that the base case simulation compared well to the physical model and produced a 95% confidence interval with an error percentage of less than 5%. Using the base case results, further design optimisation was applied by variation in oxidiser post recess length and application of swirl directional flow. An improvement of combustion length of 21.7% was achieved when the base case momentum ratio simulated at a recess length was 30% of the oxidiser post inner diameter. Applying swirl flow at the base case momentum ratio by varying the oxidiser flow improved the combustion efficiency by 1.7% to achieve 98.2%. The swirl test case produced a combustion length of 0.065m with $\pi_1 = 12.4$ and $\pi_4 = 0.06$. This is a 40.9% improvement in combustion length when compared to the base case. In all test case variations the flame pattern, flame length, temperature distribution profile, velocity profile and species concentration varied when injector design optimisation was applied.

Table of Contents

List of Figures

List of Tables

1. Introduction

1.1 Background

There has been an increase in attention given to the combustion process in high pressure coaxial rocket injectors. The design, development and testing process of coaxial rocket injectors have included software tools which can accurately predict the three dimensional fluid mechanics, reaction kinetics and effects on the design material due to high temperature combustion. An improved and reliable design can therefore be produced. The increasing interest in shear coaxial injectors for the application in rocket engines focuses on Computational Fluid Dynamics (CFD) to meet the design requirements before the physical model is assembled and tested. In the study by Vaidyanathan, et al. (2003) it is illustrated that CFD is replacing the empirically based design tools of coaxial injectors. The empirically based design tools found in Clayton, et al. (1967) are limited when considering the design space, specific to the tested element performance, Calhoon, et al. (1973). The following citations; Fujita, et al. (1996), Tamura, et al. (1997), Immich, et al. (2002), Haeseler, et al. (2006) and Berque, et al. (1999) have illustrated that there is increased focus on reducing the total number of injector elements which simplifies the design, lowers cost and in certain cases produces higher reliability.

1.2 Motivation

This study is directed at rocket engines utilising oxygen (O_2) and hydrogen (H_2) propellants in a shear coaxial design. The applications of rocket engines include satellites, space exploration and human spaceflight. Thus, illustrating the continuous improvement drive for more reliable, safer and cheaper rocket engines. To achieve this goal, a better understanding is required of the rocket engine thermo – chemical dynamics. Rocket engines inherently makes this goal challenging due to their nature of operation. The conditions of operation include high temperature and pressure, thus making online measurements inside the combustion environment challenging. The operational cost of a full size prototype, including cost of construction material and complete project development, can be expensive, and development of a full size prototype can be time consuming.

One solution to these challenge outlined, is the use of CFD. This allows for the numerical modelling of the rocket engine to determine design flaws and identify improvements thereby eliminating time and cost of manufacturing and testing of physical prototypes. Therefore, allowing the rocket engine to be safely designed to a near completion stage prior to the requirement of a physical model for hot – fire testing.

CFD solutions are computer power intensive and time consuming to produce valid results. The challenge of these numerical solutions are compounded by the complicated multi – element injector and cooling systems. The current available computer technology has improved to such an extent that challenges of power intensive computational time and power are becoming less. This means that CFD numerical models can be produced and solved faster.

Calhoon, et al. (1973) proved that injectors incorporating swirl and impingement have increased mixing efficiency but produced a high rate of heat flux on the injector faceplate and point of entry into the combustion chamber. The study determined the degree of mixing as a function of combustion when considering the swirl and impingement designs.

Studies by Schumaker, et al. (2006) highlighted that while mixing at discrete points of a gas – gas injector have been addressed, further study is required to address the variation in injection parameters. This is able to be achieved with CFD modelling. The experimental and numerical work by Soteriou, et al.,1995, Rehab, et al.,1997, Villermaux, et al., 2000 and Murakami, et al., 2002 on the effect of coaxial jets and shear layers on near and far field mixing have investigated the parameters and physics that affect the flow field. These include the inner jet diameter, stoichiometric mixture fraction, velocity ratio, density ratio, and jet momentum. However, the link between the flow characteristics and thermo chemical kinetics were not completely characterised.

Dahm, et al. (1990), Dahm, et al. (1998) and P. Dimotakis (1986) have provided a theory critical description of the evolution of the flow field and stoichiometric mixing lengths specific to the coaxial injector design. The concerns raised from these studies include the effects of high pressure chemistry while extending the density ratio range to include hydrogen and oxygen.

As discussed by Vaidyanathan, et al., 2003 the physical complexities such as high temperature and pressure environment are more complicated for supercritical, turbulent reacting flows and combustion dynamics. These complexities have caused the application of CFD to injector design to lag behind areas such as turbo machinery. Furthermore, the extremely high pressure and temperature environments applicable to an injector flow field increases the required computational time to solve equations for multiphase reacting flow to a high resolution. This study develops a CFD based model for a single element coaxial injector. A base element design case has been developed as starting point based on empirical design. The key operating indicators such as propellant flow rate, combustion chamber pressure and mixture ratio are specific to the base design case. To determine the variation in the injector performance, the selected design variables are varied based on the base case design and the resultant flow field is determined. This illustrates that the starting point of the development of a full scale multi – element rocket injector can be initiated at the single element level by using the CFD model.

It has been proven that the slightest change in the injector geometry can have significant impact on the injector performance (Ping, et al., 2013) and environmental variables such as combustion chamber wall temperature, injector face temperature and developed heat fluxes. The injector geometry manipulates the velocity at which the propellants enter the combustion chamber. This further influences the mass flow rate and contact area between the fuel and oxidiser which has a significant impact on the combustion performance. Therefore if an injector with high combustion performance at a specific characteristic length and with high mass flow rate can be established, the total number of required injectors can be decreased that effectively reduces fabrication costs.

In the study by Roth, et al. (2015) different computational tools were used for the same numerical simulations of the flow domain and combustion in a single – element coaxial injector. From the study it was shown that large discrepancies were evident in the prediction of relevant validations and design parameters of the different tools for a common operating point. The numerical results were compared to the experimental data at the Institute for Flight Propulsion at the Technische Universität München. The study highlighted that further investigation is required into the 3D – effects of the inherently transient fluid flow characteristics without the assumption of symmetry within the flow domain. The study concluded that for accurate numerical prediction to complete the design validation. Parameters that include the heat transfer, combustion reaction kinetics and the degree of mixing must be predicted with sufficient accuracy.

To obtain a high performance injector and to better understand the complex thermo - chemistry involved in shear mixing type injectors with gaseous fuel-oxidiser fluid, it is necessary to develop an accurate CFD model that compares well to the physical experimental model.

Noting the above points; the question to be answered by this Project is:

“How can the coaxial injector performance be enhanced by identifying the key design parameters and flow variables that exert strong influence on the injector behaviour of rocket engines through numerical modelling?”

To increase the reliability, safety and reduce cost of rocket engines the enhancement of the single injector performance aids as initiation to achieve this goal. The characteristic geometrical design of the injector and manipulation of propellant characteristics serves as input to outline the key design parameters. The adjustment and relation of these parameters are what gives rise to the question answered by this Project.

1.3 Objectives

The objectives of this research are:

- Determine and establish a theoretical and numerical framework that entails the conservation laws, turbulence quantification, accurate fluid thermodynamics and transport phenomena over the temperature and pressure regimes in its entirety for a highly rotational flow field
- Systematically analyse the physiochemical mechanisms at near and or supercritical conditions in order to establish the coaxial injector geometry design influence
- Investigate and determine the quantitative basis for optimising and enhancing the fuelling variations and simulated performance
- Establish a numerical model on a quantitative basis and prioritising the key design variables which influence injector behaviour

2. Literature Review

Techniques for numerical simulation that include a high degree of turbulence in the flow field can be categorised into direct numerical simulation (DNS), Reynolds-averaged Navier-Stokes (RANS) equations and large-eddy-simulation (LES). Work done by the University of Michigan provided LES simulation results of a Shear Coaxial GO_2/GH_2 Rocket Injector (Thakur, et al., 2012) with good insight into the variation of different computational grids in a three dimensional computational domain. Similarly, the potential use of LES in the modeling of flow through an injector was illustrated in the study focusing on high-pressure GO_2/GH_2 combustion of a single-element injector (Wang, et al. 2012). These studies have shown that LES modelling may be useful in modelling the highly turbulent flow field environment.

2.1 Governing Equations for a Flow with Combustion

CFD is based on the fundamental governing equations of fluid dynamics that include continuity, momentum and energy. These equations elaborate the applicable physics and can be applied to any system to develop mathematical statements of the flow domain. For the current study these equations will be used to explain the processes of interest. The theoretical formulation as outlined by Yang (2004), Anderson (1995) and Huo (2011) is based on the full conservation equation of mass, momentum, energy and species concentration are given as:

Mass:

$$\frac{\partial \rho}{\partial t} + \frac{\partial \rho u}{\partial x_i} = 0 \tag{2.1}$$

Momentum:

$$\frac{\partial \rho u_i}{\partial t} + \frac{\partial \rho u_i \rho u_j}{\partial x_j} = -\frac{\partial p}{\partial x_i} + \frac{\partial \tau_{ij}}{\partial x_j} \tag{2.2}$$

Energy:

$$\frac{\partial \rho E}{\partial t}+\frac{\partial[(\rho E+\rho)u_i]}{\partial x_i}=\frac{\partial q_i}{\partial x_i}+\frac{\partial(u_i\tau_{ij})}{\partial x_j} \tag{2.3}$$

Chemical Composition (Species Concentration):

$$\frac{\partial \rho Y_k}{\partial t}+\frac{\partial \rho Y_k u_j}{\partial x_j}=\dot{\omega}_k-\frac{\partial \rho Y_k U_{k,j}}{\partial x_j}, k=1,\ldots,N-1 \tag{2.4}$$

Where, the summation of indices are determined by the repeated indices. N, is the total species while Y_k and $U_{k,j}$ represent mass fraction and velocity of diffusion for species k, respectively. The detailed derivation by applying the conservations laws to the fundamental equations of mass, momentum and energy to an infinitesimal fluid element can be found in Anderson (1995). The viscous stress tensor τ_{ij} for a Newtonian fluid including the Stokes assumption and heat flux q_i are given as, Yang (2004):

$$\tau_{ij}=\mu(\frac{\partial u_i}{\partial x_j}+\frac{\partial u_j}{\partial x_i}-\frac{2}{3}\delta_{ij}\frac{\partial u_j}{\partial x_i}) \tag{2.5}$$

$$q_j=-\lambda\frac{\partial T}{\partial x_j}+\rho\sum_{k=1}^{N}\hat{h}_k Y_k U_{k,j} \tag{2.6}$$

The coefficients of viscosity and thermal conductivity are represented by μ and λ respectively. The λ term should not be mistaken as the second viscosity in the momentum equation. The sum of kinetic energy and specific internal energy is the specific total energy represented as, Yang (2004):

$$E=e+\frac{u_j u_j}{2} \tag{2.7}$$

The specific internal energy is represented as, Yang (2004):

$$e = h - \frac{p}{\rho} \tag{2.8}$$

h, is defined as the specific enthalpies and determined by the fluid mixture and partial mass based enthalpy $\hat{h}$, represented as, Yang (2004):

$$h = \sum_{k=1}^{N} \hat{h}_k \tag{2.9}$$

The chemical source term can be determined by considering an elementary reaction mechanism (which is defined by the chemical reaction mechanism), with L-step reaction mechanisms and N number of species which can be identified as, Yang (2004):

$$\sum_{k=1}^{N} v'_{ki}\chi_k \leftrightarrow^{k_{fi}}_{k_{bi}} \sum_{k=1}^{N} v^{n}_{ki}\, \chi_k, i = 1,2, \ldots, L \tag{2.10}$$

Where, v'_{ki} and v^{n}_{ki} are the stoichiometric coefficients based on the selected chemical reaction, reactants and products respectively for species k in the ith reaction, in the χ_k molecular formula of species k. While k_{fi} and k_{bi} are the forward reaction rate constant and backward reaction rate constant respectively. By using the Arrhenius equation these rate constants may be defined as, Yang (2004):

$$k_i(T) = A_i T^b e^{\frac{E}{RT}} \tag{2.11}$$

The net production rate, $\dot{\omega}$, of each species in a multi-step mechanism can be expressed by the following relationship as illustrated by Yang (2004):

$$\dot{\omega}_k = W_k \sum_{i=1}^{L}(v_{ki}^{n} - v_{ki}^{\prime}) \left[k_{fi} \prod_{k=1}^{N}[\chi_k]^{v_{ki}^{\prime}} - k_{bi} \prod_{k=1}^{N}[\chi_k]^{v_{ki}^{n}}\right], k = 1,2, \dots, N \quad (2.12)$$

Where,

- $W_k$represents the molecular weight
- $[\chi_k]$ represents the molar concentration of species k

Equation 2.12 can only be applied to the elementary chemical reactions of the interaction species. Section 2.4 outlines the reaction rates selected for the current study. In this section the associated exponents are outlined for the molar concentrations based on the stoichiometric coefficients.

2.2. Equation of State

The equation of state and thermodynamic data should be defined in order to evaluate the thermo physical properties as listed in the previous section. In the analysis of GO_2/GH_2 combustion in a rocket injector, the propellants experience physical and chemical changes above the critical point of the gases. At super critical conditions the behaviour of the propellants are not defined by the ideal-gas law. Therefore an equation of state should be considered that can accommodate real fluid behaviour. Cubic equations of state are commonly used to characterise real fluid behaviour that include, Koretsky (2004):

- Van der Waals
- Peng Robinson
- Modified Soave-Redlich-Kwong
- Redlich-Kwong

2.2.1 Modified Soave-Redlich-Kwong Equation of State

The modified Soave-Redlich-Kwong (SRK) is adopted for the thermodynamic property characterisation that includes the quantum gas behaviour of hydrogen. The modified SRK equation of state can be applied with a good degree of accuracy and can be represented by the findings in the study by H. Huo (2011) as:

$$p = \frac{\rho R_u T}{(W - b\rho)} - \frac{a\alpha(T)}{W}\frac{\rho^2}{(W + b\rho)} \qquad (2.13)$$

Where, ρ represents the gas mixture density and R_u represents the universal gas constant. The parameters “a” and “b” accounts for attractive and repulsive forces respectively. The symbol “α” is a function of acentric factor and temperature. The parameters “a” and “b” can be expressed as a function of critical temperature and pressure as outlined by Koretsky (2004):

$$a = \left(\frac{1}{9(\sqrt[3]{2}-1)}\right)\frac{R^2 T_c^2}{P_c} = \frac{0.42748 R^2 T_c^2}{P_c} \qquad (2.14)$$

$$b = \left(\frac{\sqrt[3]{2}-1}{9}\right)\frac{R T_c}{P_c} = \frac{0.08664 R T_c}{P_c} \qquad (2.15)$$

For fluid mixtures, since “a” and “b” are parameters which are functions of mole fractions, these parameters can be expressed by the following mixing rules, Koretsky (2004):

$$\alpha a = \sum_{i=1}^{N} \sum_{j=1}^{N} x_i x_j \alpha_{ij} a_{ij} \qquad (2.16)$$

$$b = \sum_{i=1}^{N} x_i b_i \qquad (2.17)$$

Where $\alpha_{ij}a_{ij}$ is a cross parameter given by Koretsky (2004):

$$\alpha_{ij}a_{ij} = \sum_{i=1}^{N}\sum_{j=1}^{N}\sqrt{\alpha_i\alpha_j a_i a_j}(1-\kappa_{ij}) \tag{2.18}$$

Where, κ_{ij} , is the binary coefficient with, x_i ,the mole fraction of species, i. The symbol “α” can be expressed as, Koretsky (2004):

$$\alpha_i = [1 + S_i(1-\sqrt{T_r})]^2 \tag{2.19}$$

With,

$$S_i = 0.48508 + 1.5517\omega_i - 0.15613\omega_i^2 \tag{2.20}$$

To accurately account for H_2 systems quantum behaviour, Equation 2.19 can be expressed as outlined in the study by H. Huo (2011) referring to the study by Graboski, et al. (1978):

$$\alpha_{H2} = 1.20e^{(-0.30228Tr)} \tag{2.22}$$

The gas mixture behaviour defined by the equation of state, in terms of the pressure and temperature, requires that the specie properties be fully defined in order to accurately represent the fluid behaviour.

2.2.2 Species Thermodynamic Properties

To achieve closure for the conservation equations outlined in Section 2.1, additional thermodynamic properties that are functions of temperature and pressure need to be defined. The thermodynamic properties can be derived directly from the laws of thermodynamics. For the gaseous oxygen – gaseous hydrogen (GO_2/GH_2) system the properties that will be evaluated will include density, specific energy, enthalpy, entropy and specific heat. These properties can be defined as, Huo (2011):

$$e(T,\rho) = e_0(T) + \int_{\rho_0}^{\rho} \left[\frac{\rho}{\rho^2} - \frac{T}{\rho}\left(\frac{\partial p}{\partial T}\right)_{\rho}\right]_T dp \tag{2.23}$$

$$h(T,\rho) = h_0(T) + \int_{\rho_0}^{\rho} \left[\frac{1}{\rho} - \frac{T}{\rho^2}\left(\frac{\partial p}{\partial T}\right)_{\rho}\right]_T dp \tag{2.24}$$

$$s(T,\rho) = s_0(T,\rho_0) - \int_{\rho_0}^{\rho} \left[\frac{1}{\rho^2}\left(\frac{\partial p}{\partial T}\right)_{\rho}\right]_T dp \tag{2.25}$$

$$C_p(T,\rho) = C_{V0}(T) - \int_{\rho_0}^{\rho} \left[\frac{T}{\rho^2}\left(\frac{\partial^2 p}{\partial T^2}\right)_{\rho}\right]_T dp + \frac{T}{\rho^2}\left(\frac{\partial p}{\partial T}\right)^2_{\rho} / \left(\frac{\partial p}{\partial \rho}\right)_T \tag{2.26}$$

The integral terms identify the departure functions with the subscript “0” referring to the ideal gas state at low pressure. Using the modified Soave-Redlich-Kwong equation of state all partial derivatives included in the defined thermodynamic properties outlined in Equation 2.23 to Equation 2.26 can be calculated as, Yang (2004):

$$\left(\frac{\partial p}{\partial T}\right)_{\rho,j} = \frac{\rho R_u}{(M_w - b\rho)} - \frac{1}{M_w}\left[\frac{\partial}{\partial T}(a\alpha)\right]_{\rho,Y_i} \frac{\rho^2}{(M_w + b\rho)} \tag{2.27}$$

$$\left(\frac{\partial \rho}{\partial \rho_i}\right)_{T,\rho j\neq i} = \frac{M_w RT}{M_{wi}(M_w - b\rho)^2}\left[M_w + \rho(b_i - b)\right] - \frac{2\rho\sum_j x_j a_{ij}\alpha_{ij}}{M_{wi}(M_w + b\rho)} + \frac{a\alpha\rho^2 b_i}{M_{wi}(M_w + b\rho)^2} \tag{2.28}$$

2.2.3 Partial Molar and Partial Density Properties of the GO_2/GH_2 system

The GO_2/GH_2 system is a high pressure system with the species characteristic not behaving like an ideal gas mixture. It is therefore necessary to define the mixture properties such as internal energy, specific enthalpy and specific volume as a function of temperature, pressure and chemical species. The CFD models define flow properties based on mass or density. As discussed by Huo (2011), the study by Lafon et al. (1995) introduced the concept of partial mass and partial density properties. A partial mass property ϕ in a mixture is dependent on the temperature, pressure and species mass fraction. This is defined Huo (2011) as:

$$m\phi = m\phi(p, T, m) \qquad (2.29)$$

Therefore,

$$\widehat{\phi_i} = \left(\frac{\partial m\phi}{\partial m_i}\right)_{P,T,m_{j\neq i}} \qquad (2.30)$$

While the partial density property can be defined as, Huo (2011):

$$\widehat{\phi_i} = \left(\frac{\partial \rho\phi}{\partial \rho_i}\right)_{T,\rho_{j\neq i}} \qquad (2.31)$$

The study by Meng (2001) gives the relation between the partial mass property and corresponding partial density variable that can be derived as, Hou (2011):

$$\widehat{\phi_i} = \widehat{\phi_i} + \rho\left(\frac{\partial \phi}{\partial P}\right)_{T,Y_j}\left(\frac{\partial P}{\partial \rho_i}\right)_{T,\rho_{j\neq i}} \qquad (2.32)$$

The viscosity, conductivity and mass diffusivity properties influence the fluid flow characteristics and heat and mass transfer (Yang, 2004). Equilibrium properties of fluids can be related to their critical property state originally proposed by van der Waals in 1873, according to the law of corresponding state. The state identifies that P-V-T relationship of species can be related to its critical point. The critical point represents a state that can be related to the intermolecular interaction of a given specie. As illustrated by Koretsky (2004) the reduced coordinate system of these properties can be given as, Koretsky (2004):

- $P_r = \frac{P}{P_c}$ (2.33)
- $T_r = \frac{T}{T_c}$ (2.34)
- $V_r = \frac{V}{V_c}$ (2.35)

The principle of corresponding state outlines that there is a universal function that is the same for all substances such that, (Koretsky, 2004):

$$F = \left(\frac{T}{T_c}, \frac{P}{P_c}, \frac{V}{V_c}\right) = 0 \tag{2.36}$$

Due to the supercritical nature of the propellants in the injector system of this study, it is imperative to accurately assess transport properties by not using mass averaging in a hydrogen – oxygen combustion environment. Since mass averaging does not take into account the impact of hydrogen on transport properties due to its low molecular weight.

2.2.4 Dynamic Viscosity and Thermal Conductivity

To calculate the dynamic viscosity and conductivity of a GO_2/GH_2 mixture at high pressure, the method used is outlined by Huo (2011), in which the study makes reference to Poling, et al. (2001). The method derived from elementary kinetic theory provides an estimate for dynamic viscosity and conductivity at high pressure. From the kinetic theory, dynamic viscosity (η) , conductivity (λ), transport coefficients and mass diffusivity are related to molecular speed and mean free path as, Huo (2011):

$$D = \frac{vL}{3} = (constant)\frac{T^{3/2}}{M_w p \sigma^2} \tag{2.37}$$

$$\eta = \frac{m\rho vL}{3} = (constant)\frac{T^{1/2}M_w^{1/2}}{\sigma^2} \tag{2.38}$$

$$\lambda = \frac{vLC_v n}{3} = (constant)\frac{T^{1/2}}{M_w^{1/2}\sigma^2} \tag{2.39}$$

If the molecules are considered to be finite hard spheres with diameter, σ, the viscosity can be identified as, Huo (2011):

$$\eta = \frac{T^{1/2}M_w^{1/2}}{\sigma^2} \tag{2.40}$$

In real systems, molecules are not rigid but are bounded by diffuse electron clouds and repulsive interactions occurring when the molecules are within close proximity that these electron clouds overlap. This leads to coulombic repulsion as well as possible violation of the Pauli exclusion principle as identified by Koretsky (2004). Taking the intermolecular interaction effects into account, the viscosity can be identified as, Huo (2011):

$$\eta = 26.69\frac{T^{1/2}M_w^{1/2}}{\sigma^2\Omega_v} \tag{2.41}$$

Where, Ω_v , is the collision integral calculated from the potential energy of interaction.

For gas mixtures at low pressures and to account for molecular shapes and polarities a factor, F_c, is added to Equation 2.41 to express the viscosity as, Huo (2011):

$$\eta_m = 26.69 F_c \frac{T^{1/2} M_w^{1/2}}{\sigma^2 \Omega_v} = 40.785 F_{cm} \frac{T^{1/2} M_w^{1/2}}{V_m^{2/3} \Omega_{vm}} \tag{2.42}$$

For the GO_2/GH_2 system, mixture properties are used to define viscosity as, Huo (2011):

$$\mu_m = \sigma_m^3 \sum_i \sum_j \frac{x_i x_j \mu_i^2 \mu_j^2}{\sigma_{ij}^3} \tag{2.43}$$

$$\sigma_m^3 = \sum_i \sum_j x_i x_j \sigma_{ij}^3 \tag{2.44}$$

$$T_m^* = \frac{T}{(\frac{\epsilon}{k})_m} \tag{2.45}$$

$$\left(\frac{\varepsilon}{\kappa}\right)_m = \left(\frac{\sum_i \sum_j x_i x_j (\varepsilon_{ij/k}) \sigma_{ij}^3}{\sigma_m^3}\right) \tag{2.46}$$

$$M_m = \left[\frac{\sum_i \sum_j x_i x_j (\varepsilon_{ij/k}) \sigma_{ij}^2 M_{ij}^{1/2}}{(\frac{\varepsilon}{k})_m \sigma_m^2}\right]^2 \tag{2.47}$$

$$\omega_m = \frac{\sum_i \sum_j x_i x_j \omega_{ij} \sigma_{ij}^3}{\sigma_m^3} \tag{2.48}$$

$$\kappa_m = \sum_i \sum_j x_i x_j \kappa_{ij} \tag{2.49}$$

In the study by Huo (2011) a correction factor is added to Equation 2.36 to account for the effect of high pressure on the viscosity of a pure gas after which mixture properties are applied to Equation 2.49 – 2.55. This follows as:

$$\eta_m = \eta^* \frac{36.344(MT_c)^{1/2}}{V_c^{2/3}} \tag{2.50}$$

$$\eta^* = \frac{(T^*)^{1/2}}{\Omega_v}\{F_c[(G_2)^{-1} + E_6 y]\} + \eta^{**} \tag{2.51}$$

$$y = \frac{\rho V_c}{6} \tag{2.52}$$

$$G_1 = \frac{1-0.5y}{(1-y)^3} \tag{2.53}$$

$$G_2 = \frac{E_1\{[1-e^{-iE_4 y}]/y\}+E_2 G_1 e^{E_5 y}+E_3 G_1}{E_1 E_4+E_2+E_3} \tag{2.54}$$

$$\eta^{**} = \ E_7 y^2 G_2 \exp[E_8 + E_9 (T^*)^{-1} E_{10} (T^*)^{-2}] \tag{2.55}$$

$$E_i = a_i + b_i\omega + c_i\mu_r^4 + d_i\kappa \tag{2.56}$$

The coefficients needed to calculate E_i in Equation 2.51 can be found in Huo (2011). As was done in the derivation for viscosity, the thermal conductivity can be derived in the similar manner. The thermal conductivity represented in the study by Huo (2011) can be represented as, H. Huo (2011):

$$\lambda = \frac{31.2\dot{\eta}\Psi}{M_w}(G_2^{-1} + B_6 y) + qB_7 y^2 T_r^{1/2} G_2 \tag{2.57}$$

Where,

- $\dot{\eta}$ = low pressure gas viscosity in N.s/m
- M_w = molecular weight in kg/mol
- q = $3.586 \times 10^{-3}(T_c M_w)^{1/2}/V_c^{2/3}$

$\Psi = 1 + \alpha\{[0.215 + 0.28288\alpha - 1.061\beta + 0.26665z]/[0.6366 + \beta z + 1.061\alpha\beta]\}$
(2.58)

Where,

$$\alpha = \frac{C_v}{R} - \frac{3}{2} \tag{2.59}$$

$$\beta = 0.7862 - 0.7109\omega + 1.3168\omega^2 \tag{2.60}$$

$$z = 2.0 + 10.5T_r^2 \tag{2.61}$$

$$G_2 = \frac{(B_1/y)\,[1-e^{-B_4 y}]+B_2 G_1 e^{B_5 y}+B_3 E_1}{B_1 B_4+B_2+B_3} \tag{2.62}$$

$$B_i = a_i + b_i\omega + c_i \mu_r^4 + d_i\kappa \tag{2.63}$$

The coefficients needed to calculate the conductivity can be found listed in the study by Huo (2011). The dynamic viscosity and thermal conductivity strongly influences the outcome of the calculated wall heat flux term in this study. Illustrating the need for real gas behaviour as far as possible of these transport properties in the high temperature and pressure combustion environment.

2.2.5 Mass Diffusivity

The mass diffusivity is a function of the molecular weight, empirical coefficient, absolute pressure, collision diameter and temperature dependent collusion integral. At high pressure mixtures there is a change in the dependent variables. At high pressure mixtures the mass diffusivity is no longer constant and changes as the mixture changes. Considering the empirical correlation as referenced in Huo (2011) for low pressure binary mass diffusivity. A corresponding state method is used by Huo (2011) for the high pressure effect. Firstly in the study the low pressure correlation is considered during which the study references B.E. Poling, et al. (2001), Huo (2011):

$$D_{ij} = \frac{0.00143T^{1.75}}{pM_{ij}^{1/2}\left[(\Sigma_v)_i^{\ 1/3}+(\Sigma_v)_j^{\ 1/3}\right]^2} \tag{2.64}$$

Where,

- D_{ij}, is the binary mass diffusivity (cm^2/s)
- Σ_v, is the sum of atomic diffusion volume

Σ_v, can be found in the atomic diffusion volume in Table 2.3 of the study by Huo (2011). The study by Huo (2011) applies the Takashi correlation for the high pressure system given by, Huo (2011):

$$\frac{D_{ij}p}{\left(D_{ij}p\right)^{+}} = f(T_r, p_r) \quad (2.65)$$

Where,

- The superscript + indicates the low pressure correlation represented by Equation 2.62
- $f(T_r,p_r)$, represents a pressure scaling factor given by Huo (2011). To calculate the reduced temperature and pressure, the combining rules are used, Huo (2011):

$$T_c = x_i T_{c,i} + x_j T_{c,j} \quad (2.66)$$

$$p_c = x_i p_{c,i} + x_j p_{c,j} \quad (2.67)$$

An alternative to the outlined method is using the Lewis number that relates the thermal and mass diffusion in the concentration and thermal boundary layer, Cengel (2006):

$$Le = \frac{Sc}{Pr} = \frac{\alpha}{D_{AB}} = \frac{Thermal\ diffusivity}{Mass\ diffusivity} \quad (2.68)$$

This will allow to determine the mass diffusion rate of the propellants at a specific point in the gas mixture that is proportional to the species concentration gradient at the specific point in the flow domain, Cengel (2006).

2.3 Turbulence Modelling

The strong nonlinear behaviour of turbulence modelling remains a challenge in computational fluid dynamics. The computational fluid dynamic numerical model of turbulence can be classified into 3 categories as outlined by Yang (2004):

- Direct numerical simulation (DNS)
- Reynolds-averaged Navier-Stokes (RANS)
- Large eddy simulation (LES)

The DNS is the most unequivocal method. The DNS method produces an accurate solution by discretising the governing equations with sufficient resolution and it is solved numerically by resolving the small scale motion. Therefore with sufficient computing power the governing equations of flow evolution can be solved without any model and the turbulent scales can be resolved explicitly. It makes the DNS a useful tool for insight into the detailed kinematics and dynamics of turbulent flows. The study by Huo (2011) references the findings in the study by Moin (1998) illustrating this. To investigate physiochemical processes, DNS has been applied to supercritical mixing as with the study by Miller, et al. (2001) and combustion processes as with the study by Vervisch, et al. (1998). For turbulent sub grid scale modelling and combustion model validation the DNS method can be used. According to Huo (2011), to resolve turbulence scales in a three dimensional system, the grid number should be considered proportional to $Re_L^{9/4}$, therefore DNS method is limited to small Reynolds number flows ($Re_L = 0(10^4)$. The study by Huo

(2011) furthermore references the study by Piomelli (2002) and indicates that DNS is not feasible for industrial applicaitons.

The Reynolds averaged Navier-Stokes (RANS) equations have been widely used for most turbulent flow systems. The computational power required for the RANS method is significantly less than that of the DNS method. Using the RANS method allows for statistical quantities to be predicted, such as the time-averaged mean quantities. Not all effects of the scales of motion are modelled with this method i.e. the Unsteady-RANS method only partially resolves the coherent motions as investigated by the study of P. Sagut (2001). The RANS method requires moderate computing power and has proven success in wide industry. The small scale motions are isotropic and tend to be universal to model at high Reynolds number based on the Kolmogorov’s hypothesis as proven by the study of Pope (2000). It is therefore difficult to achieve a universal model that can include all turbulent flows due to the large-scale motions that are strongly dependant on the boundary conditions as discussed by the study of Huo (2011).

For the current study it is therefore required that a balance between the accuracy and computational power requirement of the DNS and RANS be achieved. An intermediate method known as the Large Eddy Simulation (LES) can achieve a higher accuracy than that of the RANS method while requiring less computational power than the DNS method. The study by Ivancic, et al. (2002) found that at high pressures the chemical timescale is several orders of magnitude smaller than the Kolmogorov timescale. The current study utilises a frequency based model rather than a time step model due to the very small time scale in which combustion occurs. The study by the LES method directly simulates and applies a filter for the largest scales which contain the most energy and are fully resolved, as referenced by the study of Huo (2011). Smaller scales (subgrid scales) are modelled when using this method Piomelli, et al. (2002). The method assumes that the small scale flow evolution is more homogenous than large scale flow motions. According to the study by Huo (2011), small scale motions are more isotropic and universal and therefore can be modelled with less adjustments to the model coefficients, when compared to the RANS model simulations. To resolve all the scales of motion explicitly and accurately it will require significant computational power and time via the DNS method and therefore is avoided.

The Kolmogorov scales eventually disappears with decreasing scales due to the inhomogeneity of flow properties as investigated by Huo (2011). Therefore with the LES method grid size applies to the inertial range as in the study by Yang (2004). Peak values at less than 30 wall units are achieved due to the dissipation of turbulent kinetic energy at the near wall region as studied by Pope (2000). The Reynolds number will determine the energy containing scales. The exchange between large and small scales are different from unconstrained flow due to the wall presence that prohibits small scales growth. For the current system being studied that contains high Reynolds number flow, it is imperative to include the energy generating occurrences at the near wall layer. It is therefore required that a very fine grid be used in this region. According to Huo (2011) in which the Chapman's estimate by the study Chapman (1979) is referred to, the boundary layer is divided into two sections namely, the outer and inner layers. For the outer layer the number of grid points scales with $Re^{0.4}$, while with the inner layer it scales with $Re^{1.8}$. The study by Huo (2011) further highlights the wall layer modelling is imperative when applying the LES method. Huo (2011) indicates that there has been many research on the wall modelled LES method done. It mentions that in the studies by Cabot (1995) and Balaras (1996) modelling is done at the near wall region in the LES method of shear flow in a wall bounded system. It further discusses that the study by Spalart (2009) investigated a Detached-Eddy Simulation (DES) method. For the Reynolds stress and sub-grid stress modelling the DES method used Spalart-Allmaras turbulence model or k-omega SST model.

The current study employs the LES method to obtain turbulent closure. As mentioned, this method does not resolve the small scale turbulent motions. In this range of scales viscous dissipations change kinetic energy into internal energy. The appropriate sub grid scale (SGS) models has to be selected to model the turbulent motions. As discussed by Huo (2011) SGS modelling is at the core of the LES method. Due to the dissipation scales being unresolved the purpose of the SGS models is to convert energy from resolved scales to unresolved scales via the energy cascade as discussed by Yang 2004. Most of the SGS models are based on the eddy-viscosity model and include:

- Smagorinsky eddy viscosity model by J. Smagorinsky (1963)
- Dynamic eddy viscosity model, Germano, et al. (1991)
- Similarity and mixed model, Bardina, et al. (1980), Zang, et al. (1993), Meneveau, et al. (2000)

As discussed by Huo (2011) due to the simplicity of the Smagorinsky SGS model Smagorinsky (1963) it has been widely used in many industrial applications with good accuracy at sufficiently fine mesh grids. However, as discussed by Yang (2004) and Huo (2011), the SGS model has challenges due to positive coefficients in its standard form and as a result in the laminar regions or the viscosity sub-layers of boundary layers the model is too dissipative to predict the SGS stresses. Therefore the Smagorinsky model with positive constants will result in a non-zero residual stress tensor in the laminar shear flow or viscous sub layers in the near wall region. Furthermore, in the near wall region the Smagorinsky model cannot predict energy backscatter. The energy flux from small to large scales are neglected with a constant model coefficient as discussed in the study by Huo (2011). As outlined by Yang (2004) these challenges can be avoided by introducing ad hoc modifications. These include:

- Van Driest damping, Driest (1956)
- Intermittency function, Pomelli (1999)

The Van Driest damping corrects the model behaviour at near wall regions while the intermittency function eliminates the non-zero residual stress in the laminar flow region. The mentioned adjustments require an empirical function as discussed by Huo (2011).

A dynamic eddy viscosity model in which the study by Germano (1991) is referenced by Huo (2011), was proposed to avoid the empirical coefficients in the Smagorinsky model. The Smagorinsky coefficient is dynamically determined from the resolved flow motion instead of using the constant input value. An alternative to using a LES filter like what is done in the Smagorinsky model, in the dynamic model, both a test and an LES filter are used. The dynamically calculated coefficient is not positive definite and backscatter of energy is allowed when the model coefficient is negative.

2.3.1 Process of Filtering

The following section discusses the governing equations filtering process including the turbulent SGS models. To study high pressure mixing and combustion the filtered governing equations, thermodynamic properties and turbulence closure model will be investigated.

In order to separate the large scale from the small scale turbulent motions in a LES model, the filtering process will be used. Where a filtered variable is defined as, Yang (2004):

$$\bar{f}(x) = \int_{\infty} f(x) G_f(x - x') dx' \qquad (2.69)$$

Where,

- G_f , is the filter function
- $\int_{\infty} G_f(x) dx = 1$

The size and structure of the small scales are determined by the filter function. The study by Leonard (1974) outlined that the differentiation and filtering operations could be applied if, G, is only a function of $x - x'$. As discussed by Huo (2011), the Top-hat, Gausian and Cutoff filters are of the most commonly used filter functions. For stretched grids the commutation error is usually neglected and accounted for by the SGS models as discussed by Huo (2011) referencing the study by Ribault (1999). Additionally a simplified filter function, the box filter can be used as outlined by Pope (2000), Yang (2004):

$$\bar{f}(x) = \frac{1}{\Delta V} \int f(x) dx \tag{2.70}$$

Equation 2.68 indicates that the box filter operation is the average in the control volume.

2.3.2 Filtered Governing Equations

The Favre-averaging method establishes that an instantaneous variable (f) can be defined as the sum of the Favre averaged filtered scale $(\tilde{f})$ and a sub filter scale (f''), Huo (2011):

$$f = \tilde{f} + f'' \tag{2.71}$$

Where,

$$\tilde{f} = \frac{\overline{\rho f}}{\overline{\rho}} \tag{2.72}$$

To account for the variable density effects and to simplify the governing equations the Favre averaging is used. According to Huo (2011), $\widetilde{f''} \neq 0$ and $\overline{f'} \neq 0$, therefore the filter operation for the LES method is different to the Reynolds averaging method. Applying this difference to the governing equations of mass, momentum, energy and mixture fraction can be presented as, Yang (2004):

$$\frac{\partial \bar{\rho}}{\partial t} + \frac{\partial \bar{\rho} \tilde{u}_i}{\partial x_i} = 0 \tag{2.73}$$

$$\frac{\partial \bar{\rho} \tilde{u}_i}{\partial t} + \frac{\partial (\bar{\rho} \tilde{u}_i \tilde{u}_j + \bar{p} \delta_{ij})}{\partial x_j} = \frac{\partial (\bar{\tau}_{ij} - \tau_{ij}^{sgs})}{\partial x_j} \tag{2.74}$$

$$\frac{\partial \bar{\rho} \tilde{E}}{\partial t} + \frac{\partial ((\bar{\rho} \tilde{E} + \bar{\rho}) \tilde{u}_i)}{\partial x_i} = \frac{\partial}{\partial x_i} (\tilde{u}_j \tilde{\tau}_{ij} + \lambda \frac{d\tilde{T}}{dx_i} - H_i^{sgs} + \sigma_i^{sgs}) \tag{2.75}$$

$$\frac{\partial \bar{\rho} \tilde{Y}_k}{\partial t} + \frac{\partial (\bar{\rho} \tilde{u}_j \tilde{Y})}{\partial x_j} = \frac{\partial}{\partial x_j} \left(\bar{\rho} \widetilde{U}_{k,j} \tilde{Y}_k - \phi_{k,j}^{sgs} - \Theta_{k,j}^{sgs} \right) + \bar{\dot{\omega}}_k \tag{2.76}$$

The sub-grid scale (SGS) terms are defined as:

$$\tau_{ij}^{sgs} = (\overline{\rho \tilde{u}_\imath \tilde{u}_\jmath} - \bar{\rho} \tilde{u}_i \tilde{u}_j) \tag{2.77}$$

$$H_i^{sgs} = \left(\overline{\rho E u_\imath} - \bar{\rho} \tilde{E} \tilde{u}_i \right) + (\overline{p u_\imath} - \bar{p} \tilde{u}_i) \tag{2.78}$$

$$\sigma_i^{sgs} = (\overline{u_\jmath \tau_{\imath\jmath}} - \tilde{u}_j \tilde{\tau}_{ij}) \tag{2.79}$$

$$\phi_{k,j}^{sgs} = (\overline{\rho Y_k u_\jmath} - \bar{\rho} \tilde{Y}_k \tilde{u}_j) \tag{2.80}$$

$$\Theta_{k,j}^{sgs} (\overline{\rho Y_k U_{k,\jmath}} - \bar{\rho} \tilde{Y}_k \widetilde{U}_{k,j}) \tag{2.81}$$

From the above listed SGS terms the stress term, $\tilde{\tau}_{ij}$, SGS energy flux term H_i^{sgs}, and SGS species flux terms, $\phi_{k,j}^{sgs}$, is a result from filtering the corresponding convective terms. The correlation of the velocity field function with the viscous stress tensor function results in the SGS viscous term, σ_i^{sgs}, while the correlation between the velocity field function and the species mass fraction results in the species diffusive flux term, $\theta_{k,j}^{sgs}$ as discussed by the study of V. Yang (2004). The species mass production rate, $\bar{\dot{\omega}}_k$ is also unclosed. As outlined in Section 2.2.1, it is required that the equation of state be filtered in addition to the listed conservation equations. Therefore the filtered equation of state can be represented as, Yang (2004):

$$\bar{p} = R_u \tilde{Z} \bar{\rho} \tilde{T} + R_u (\tilde{Z} \overline{\rho"T"} + \bar{\rho} \overline{Z"T"} + \tilde{T} \overline{Z"\rho"}) \tag{2.82}$$

In the above equation, Z, represent the compressibility factor. From the study by (W. Calhoon, 1996) the filtered equation of state can be ignored for ideal gas with no heat release. This is not the case for high pressure real fluid mixtures, which is applicable to the current study. From the study by (Huo, 2011) the total energy term, $\tilde{E}$, can be defines as, Yang (2004):

$$\tilde{E} = \tilde{h} - \frac{\tilde{p}}{\bar{\rho}} + \frac{\tilde{u}_k^2}{2} + k^{sgs} = \widetilde{\Psi} + \int_{p0}^{p} \left[\frac{1}{\rho} + \frac{T}{\rho^2} \left(\frac{d\rho}{dT} \right)_p \right] dp - \frac{\tilde{p}}{\bar{\rho}} + \frac{\tilde{u}_k^2}{2} + k^{sgs} \tag{2.83}$$

With,

$$\Psi = \sum_1^N Y_k h_k^0 \tag{2.84}$$

$$k^{sgs} = \frac{\tau^{sgs}}{2\bar{\rho}} = \frac{1}{2} \left(\frac{\overline{\rho u_k u_k}}{\bar{\rho}} - \tilde{u}_k^2 \right) \tag{2.85}$$

2.3.3 Subgrid Scale Models

LES consists of SGS modelling and these models are introduced to allow energy transfer from larger to smaller scales due to small eddies dissipating most of the energy. This transfer is necessary to transfer internal energy at the correct dissipation rate of which most of the SGS models are based on the eddy viscosity model, where the stress, τ_{ij}^{sgs}, is related to the large scale strain rate tensor $\tilde{S}_{ij}$ as defined in Yang (2004):

$$\tau_{ij}^{sgs} - \frac{\delta_{ij}}{3}\tau_{kk}^{sgs} = -2v_i\tilde{S}_{ij} \tag{2.86}$$

Where,

$$S_{ij} = \frac{1}{2}\left(\frac{\partial\tilde{u}_j}{\partial x_i} + \frac{\partial\tilde{u}_i}{\partial x_j}\right) \tag{2.87}$$

v_i, represents the eddy viscosity.

2.3.3.1 Algebraic Smagorinsky Model

The algebraic model is used to obtain the eddy viscosity to avoid additional equations needed for closure. The model is simplified by using the equilibrium hypothesis which assumes small scale motions, with shorter time scales than large eddies, that can adjust rapidly to perturbation and recover equilibrium instantaneously as discussed in the study by V. Yang (2004). Therefore a balance exists between the sub grid scale kinetic energy production term and the viscous dissipation rate, Yang (2004):

$$-\tau_{ij}\bar{S}_{ij} = \varepsilon_v \tag{2.88}$$

The Smagorinsky model can be outlined based on the equilibrium hypothesis as, Yang (2004):

$$v_t = (C_s \mathit{\Delta})^2 \left|\tilde{S}\right| \qquad (2.89)$$

The, $\mathit{\Delta}$, in the equation above represents the filter width. By using the priori test on isotropic turbulence decay the C_s coefficient can be defined, while the study by V. Yang (2004) references the study by Erlebacher (1992) that developed a correlation of the Smagorinsky model to include flow compressibility effects which is applicable to the current study, Yang (2004):

$$\tau_{ij}^{sgs} = -2v_t\bar{\rho}(\tilde{S}_{ij} - \frac{\tilde{S}_{kk}\delta_{ij}}{3} + \frac{2}{3}\bar{\rho}k^{sgs}\delta_{ij} \qquad (2.90)$$

The eddy viscosity is represented by, v_t:

$$v_t = C_R(\mathit{\Delta} D)^2 \left|\tilde{S}\right| \qquad (2.91)$$

$$k^{sgs} = C_I(\mathit{\Delta} D)^2 \tilde{S}_{ij}\tilde{S}_{ij} \qquad (2.92)$$

The compressible Smagorinsky constants are represented by the dimensionless quantities C_R and C_I . P. Kim (1981), expressed the inhomogeneities at the near-wall region by using the Van-Driest damping function (D) and represented in the study by H.Huo (2011) as, Yang (2004):

$$D = 1 - \exp(1 - (y^+/\ 25)^2) \qquad (2.93)$$

Where, $y^+ = yu_\tau/v$ and u_τ is the friction velocity. The energy flux term, H_j^{sgs}, can be modelled as, Yang (2004):

$$H_j^{sgs} = -\bar{\rho}\frac{\nu_t}{Pr_t}\left(\frac{\partial\tilde{h}}{\partial x_j} + \tilde{u}_i\frac{\partial\tilde{u}_i}{\partial x_j} + \frac{1}{2}\frac{\partial k^{sgs}}{\partial x_j}\right) \tag{2.94}$$

The turbulent Prandtl number represented by, Pr_t , is set at 0.9 for the current study. The SGS viscous term, σ_{ij}^{sgs}, as described by Yang (2004), is neglected due to its minimal contribution to the total energy, while the approximation used to describe the convective species flux can be represented as:

$$\phi_{k,i}^{sgs} = -\bar{\rho}\frac{\nu_t}{Sc_t}\frac{\partial\tilde{Y}_k}{\partial x_i} \tag{2.95}$$

The turbulent Schmidt number represented by, Sc_t, is set at 0.7 for the current study. The agreement with experimental data represented by Zhukov (2015), was achieved by the optimisation of the turbulent Prandtl and Schmidt numbers. The turbulent Prandtl and Schmidt numbers are responsible for defining the turbulent heat and mass transfer respectively. As discussed by the study of Yang (2004), Durbin (1996) achieved agreement between simulation and experimental results by including Durbin's limiter in order to bound the diagonal components of the Reynolds stress tensor. The study by Durbin (1996), utilised different numerical mesh sizes, different boundary conditions and RANS solvers. It outlines the importance of the influence of the turbulent Prandtl and Schmidt numbers.

The algebraic Smagorinsky model as outlined in Section 2.3.3.1 is widely used in the Large Eddy Simulation method but has limitations as outlined by Germano, et al. (1991). These limitations as outlined by Yang (2004) include:

- The optimal model constant changes for different characterisation of flow
- At the near wall region the model does not have correct limiting behaviour
- The model is dissipative in the transition region

- Backscatter of energy from small to large scales is not accounted for by the model which is imperative in the transition region

To address these limitations of the algebraic Smagorinsky model to ensure that the limitations have minimal effect on the simulation results, the following dynamic model is additionally incorporated.

2.3.3.2 Dynamic Smagorinsky Model

As discussed by Yang (2004), the study by Germano, et al. (1991) introduced a dynamic model that seeks to close the limitations of the algebraic Smagorinsky model listed in Section 2.3.3.1. By applying the resolved scales measured coefficient to the SGS range, the model incorporates the assumption of scale invariance. Therefore by not treating the model coefficients as adjustable parameters as in the standard Smagorinsky model, the dynamic model calculates the coefficients dynamically from the information already contained in the resolved velocity field during the simulation. As outlined by Yang (2004), by using resolved scale information, the dynamic model uses this at grid – filter level with a coarser test – filter $\tilde{\bar{G}}$, which has the characteristic $\tilde{\bar{\Delta}} > \bar{\Delta}$ (where, $\tilde{\bar{\Delta}} = 2\bar{\Delta}$), applicable to the equations of motion, similar filtered equations are obtained as in Equation 2.71-2.74. The study by Yang (2004) discussed that this application is necessary in order to obtain the model parameters C_R and C_l as a function of time and space as the study by Germano, et al. (1991). Using the Germano identity on which the dynamical procedure is based on, Yang (2004):

$$L_{ij} = T_{ij} - < \tau_{ij}^{sgs} > \tag{2.96}$$

Where, $L_{ij} =< \bar{\rho}\tilde{u}_i\tilde{u}_j > - < \bar{\rho} > \overleftrightarrow{\tilde{u}_\iota}\overleftrightarrow{\tilde{u}_\jmath}$, and $T_{ij} =< \overline{\rho u_\iota u_\jmath} > - < \bar{\rho} > \overleftrightarrow{\tilde{u}_\iota}\overleftrightarrow{\tilde{u}_\jmath}$

And the Favre filtered variable is defined as, $\overset{\leftrightarrow}{\tilde{f}} =< \overline{\rho f} >/< \bar{\rho} >$. Based on the test filter the, < >, denotes the averaging operator. The following expressions as outlined by (Yang, 2004) can be derived to obtain the dynamic model parameters, C_R and C_l by using the least square minimisation approach of (Lilly, 1992), Yang (2004):

$$C_R = \frac{<L_{ij}M_{ij}>}{<M_{kl}M_{kl}>} - \frac{1}{3}\frac{<L_{mm}M_{nn}>}{<M_{kl}M_{kl}>} \tag{2.97}$$

$$C_l = \frac{<L_{kk}>}{<\beta - <\alpha\gg} \tag{2.98}$$

Where M_{ij}, β and α are represented as, Yang (2004):

$$M_{ij} = \beta_{ij} - < \alpha_{ij} > \tag{2.99}$$

$$\beta_{ij} = -2\hat{\Delta}^2 < \bar{\rho} > \left|\overset{\leftrightarrow}{\tilde{S}}\right| \left(\overset{\leftrightarrow}{\tilde{S}}_{ij} - \frac{\delta_{ij}}{3}\overset{\leftrightarrow}{\tilde{S}}_{kk}\right);\ \alpha_{ij} = -2\Delta^2 |\tilde{S}| (\tilde{S}_{ij} - \frac{\delta_{ij}}{3}\tilde{S}_{kk}) \tag{2.100}$$

$$\beta = 2 < \bar{\rho} > \hat{\Delta}^2 \left|\overset{\leftrightarrow}{\tilde{S}}\right|^2 ; \alpha = 2\bar{\rho}\Delta^2 \left|\tilde{S}\right|^2 \tag{2.101}$$

The procedure outlined above can be used to dynamically calculate the turbulent Prandtl and Schmidt numbers.

2.4 Reaction chemistry

This section will elaborate the H_2/O_2 reaction chemistry and combustion process which is imperative for rocket propulsion. The current study evaluates the non-premixed injection of propellants and the turbulent combustion thereof with accurate numerical modelling. The study by M. Hersch (1967) calculated the hydrogen (H_2) and oxygen (O_2) interaction chemical kinetics. The chemical reaction rate described by the study is strongly nonlinear and adheres to the Arrhenius Law. As in the study by M. Hersch (1967), the current study injects hydrogen annularly around a centre-fluid of oxygen. The propellants injected into the combustion chamber are routed from equal pressure lines. As will be noted from the data analysis section of this study, the varying operational pressure of the combustion chamber will be set nominally equal to the propellant line pressures. Due to the miniscule pressure difference between the oxidiser and fuel line, the mixing process between the hydrogen and oxygen is driven by the shear occurring at the interface of the hydrogen and oxygen fluids which are set at different velocities. Due the mixing caused by the shear, the propellant fluids are mixed in the shear layer, which in turn initiates the combustion process. The reaction at the shear layer occurs stoichiometrically, although the injection equivalence ratio is at non-stoichiometric conditions.

Combustion instabilities cause large temperature and pressure variations. The chemical reaction rates are susceptible to variations in temperature and pressure and therefore the chemistry selection is important to accurately model the experimental data. The study by Turns (2000) elaborates on the multiple reaction steps associated with H_2/O_2 combustion system. This study outlines that the initiation step reactions include, Turns (2000):

$$H_2 + M \rightarrow H + H + M \tag{2.102}$$

$$H_2 + O_2 \rightarrow HO_2 + H \tag{2.103}$$

In the above listed reaction equations, M, represents a third body such as N_2. During the initiation period, the radicals O, H and OH are formed by the chain - reaction steps that include, Turns (2000):

$$H + O_2 \rightarrow O + OH \tag{2.104}$$

$$O + H_2 \rightarrow H + OH \tag{2.105}$$

$$H_2 + OH \rightarrow H_2O + H \tag{2.106}$$

$$O + H_2O \rightarrow OH + OH \tag{2.107}$$

The study by Turns (2000) elaborates that after the initiation period is followed by an induction period. During the induction period there is an exponential growth of atoms and radicals. Towards the end of the induction period atom and radical concentration increase to the point that it causes an increase in temperature due to the three-body recombination reactions. The recombination reactions include the O, H and OH radicals are the chain – terminating reaction steps, Turns (2000):

$$H + H + M \rightarrow H_2 + M \tag{2.108}$$

$$O + O + M \rightarrow O_2 + M \tag{2.109}$$

$$H + O + M \rightarrow OH + M \tag{2.110}$$

$$H + OH + M \rightarrow H_2O + M \tag{2.111}$$

To further complete the radical formation, the hydroperoxy radical, HO_2, and hydrogen peroxide, H_2O_2, has to be included, Turns (2000):

$$H + O_2 + M \rightarrow HO_2 + M \tag{2.112}$$

Equation 2.106 proceeds with the following reaction steps and the reverse reaction of Equation 2.101, Turns (2000):

$$HO_2 + H \rightarrow OH + OH \tag{2.113}$$

$$HO_2 + H \rightarrow H_2O + O \tag{2.114}$$

$$HO_2 + O \rightarrow O_2 + OH \quad (2.115)$$

$$HO_2 + HO_2 \rightarrow H_2O_2 + O_2 \quad (2.116)$$

$$HO_2 + H_2 \rightarrow H_2O_2 + H \quad (2.117)$$

The following reactions are necessary to complete the rate reaction, Turns (2000):

$$H_2O_2 + OH \rightarrow H_2O + HO_2 \quad (2.118)$$

$$H_2O_2 + H \rightarrow H_2O + OH \quad (2.119)$$

$$H_2O_2 + H \rightarrow HO_2 + H_2 \quad (2.120)$$

$$H_2O_2 + M \rightarrow OH + OH + M \quad (2.121)$$

The reverse reaction of the above listed reactions are dependent on the temperature, pressure and extent of reaction of the environment within the combustion chamber. The eight species H_2, O_2, H_2O, OH, O, H, HO_2 and H_2O_2 represent the species associated with H_2/O_2 combustion system. This system has characteristics of sudden pressure and temperature increases within certain species concentrations and the temperature and pressure environment. There are however regions within the temperature and pressure curve where this phenomenon is not experienced such as at 500°C and low pressure of less than 0.01bar. This is due to the free radical formation as described in Equation 101 and Equation 102-105 being diminished by the combustion chamber walls. The chamber wall prevents accumulation of radicals which leads to an abrupt temperature and pressure increase. This phenomenon is not included in the current study because the study is confined to only gas phase reactions. The study by Turns (2000) represents this phenomenon as:

$$Radical \xrightarrow{k_{wall}} absorbed\ products \quad (2.122)$$

The reaction constant, k_{wall}, is a function of the wall surface characteristics, diffusion and the chemical process. Solids combustion and catalysis involve heterogeneous reactions which involve the reaction of gaseous species at solid surfaces. This however is not applicable to the current study and will not be further investigated.

At a pressure greater than 0.01bar and 500°C the reaction mixture experiences significant temperature and pressure increase due to the radical formation prevailing over the radical destruction at the wall. While at 500°C and 0.07bar the reaction mixture stabilises due to scarcity of H – atoms causing competition between the chain branching and chain terminating reactions. At 4bar combustion chamber pressure the reaction mixture also experiences again a significant temperature and pressure increase due a chain terminating step that promotes the H_2O_2 chain sequence. The aforementioned is applicable to the current study and will be further elaborated on in the Results and Discussion Section. The current study incorporates the reaction rate across a wide temperature and pressure range in order to accurately evaluate species interaction and consequence thereof on the simulated data.

2.5 Injector Design Performance Evaluation

In this section the injector design performance evaluation is conducted using the following:

- Key injector design parameter optimisation to achieve reduced combustion length, L_{com}
- Geometry adjustment to improve mixing and evaluate by using combustion efficiency, η_{C^*}

The study by Xiao-Wei, et al. (2011) used the combustion length (L_{com}) as a target objective for the respective study. By decreasing the combustion length the injector length can be reduced while sustaining a high combustion efficiency. This will reduce the total injector weight and improve rocket engine efficiency. For the current study this target objective will be used as performance evaluation to compare the different design variations. In the studies by Farhangi, et al. (1999), Sozer, et al. (2009) and Calhoon, et al. (1973) the L_{com} is used to evaluate the injector performance based on the combustion process. The study by Xiao-Wei, et al. (2011), uses the ratio of residual O_2 mass flow rate of 50% as indication of combustion completion. A smaller combustion length will indicate an increased mixing effect that increases the effectiveness of the combustion process. As the study by Wang, et al. (2011) indicates, the π theorem is utilised to identify all parameters that could influence the combustion length and their common interaction. Dimensional analysis is applied to the single element injector to highlight the key design parameters influencing the combustion length. The study by Xiao-Wei, et al. (2010) expresses the combustion length as a function of the key design parameters by using this π theorem. As in the study by Xiao-Wei, et al. (2010), for the current study of the GO_2/GH_2 single element injector design, the parameters that have an influence on the combustion length include, Xiao-Wei, et al. (2010):

Geometric parameters:

- Oxidiser post (d_{O_2}) inner diameter
- Fuel annulus (inner and outer diameter of Hydrogen, $d_{H_{2,1}}$ and $d_{H_{2,2}}$ respectively)
- Recess length (L_r)
- Combustion Chamber diameter (d_C)

Velocity parameters:

- Fuel velocity (u_{H_2})
- Oxidiser velocity (u_{O_2})

Combustion chamber parameter:

- Combustion chamber pressure (p_C)

Specie property parameters:

- Density (ρ_{H_2}, ρ_{O_2})
- Temperature (T_{H_2}, T_{O_2})
- Viscosity (μ_{H_2}, μ_{O_2})
- Specific heat (c_{p,H_2}, c_{p,O_2})
- Diffusivity (D_{H_2}, D_{O_2})
- Conductivity ($\lambda_{H_2}, \lambda_{O_2}$)
- Specie wall boundary parameter (G)
- Heat flux loss ($\dot{q}$)
- Reaction rate (w_s)

In the study by Xiao-Wei, et al. (2010) after applying the π theorem there are ten dimensionless parameters introduced, Xiao-Wei, et al. (2010):

- $\pi_1 = \frac{L_{com}}{d_{O_2}}$
- $\pi_2 = \frac{d_{H_{2,1}}}{d_{O_2}}$
- $\pi_3 = \frac{d_{H_{2,2}}}{d_{O_2}}$
- $\pi_4 = \frac{L_r}{d_{O_2}}$

- $\pi_5 = \frac{d_c}{d_{O_2}}$
- $\pi_6 = \frac{\rho_{O_2}}{\rho_{H_2}}$
- $\pi_7 = \frac{p_C}{\rho_{O_2}.u_{O_2}^2}$
- $\pi_8 = \frac{u_{H_2}}{u_{O_2}}$
- $\pi_9 = \frac{\dot{q}}{\rho_{O_2}.u_{O_2}^3}$
- $\pi_{10} = \frac{w_s}{\rho_{O_2}.u_{O_2}/d_{O_2}}$

The listed ratios are the identified key design parameters that can influence the single element coaxial injector design optimisation. The study by Xiao-Wei, et al. (2010) develops the following expression from the π theorem, Xiao-Wei, et al. (2010):

$$\pi_1 = f(\pi_2, \dots, \pi_{10}) \qquad 2.123$$

In the study by Xiao-Wei, et al. (2010) Equation 2.123 indicates that π_1 remains unchanged given that $\pi_2, \dots, \pi_{10}$ remains constant. It further illustrates the ratio of the key parameters on the combustion flow. The current study will select the parameters listed below to investigate for performance evaluation in terms of combustion length and efficiency:

- Recess length
- Injection momentum ratio (m_r) of the fuel and oxidiser
- Oxidiser velocity (optimisation of flow direction into the combustion chamber)

Combustion efficiency can be calculated by using the relation applied in the study by Xiao-Wei, et al. (2011):

$$\eta_{C^*} = \frac{C^*_{Exp}}{C^*_{Th}} \qquad 2.124$$

Where,

$$C^*_{Exp} = \frac{p_c A_t}{\dot{m}} \qquad 2.125$$

$$C^*_{Th} = \frac{\sqrt{kRT_{Th}}}{k\sqrt{\left(\frac{2}{k_{Th}+1}\right)^{\frac{k+1}{2(k-1)}}}} \qquad 2.126$$

The constants in Equation 2.125 and 2.126 represents the following:

- p_c, combustion chamber pressure
- $\dot{m}$, the total mass flow rate
- A_t, is the combustion chamber throat area
- k, is the specific heat ratio
- R, represents the universal gas constant
- T_{Th}, represents the adiabatic flame temperature of each investigated case respectively

The efficiency quantifies the injector performance based on the extent of the combustion completion of fuel in the chamber. The numerical model allows for the fuel mass flow rate to be determined throughout the entire flow domain. This is used to evaluate the applicability of method outlined by Xiao-Wei, et al. (2011).

2.6 Swirl Coaxial Injector

The current study additionally investigates the application of swirl coaxial flow. The key design parameter investigates the flow direction of the oxidiser into the combustion chamber. The oxygen is injected tangentially to the center oxidiser post. Similarly to the study by GuoBiao, et al. (2016), the oxidiser is injected into the combustion chamber in the pattern of swirl flow while the gaseous hydrogen fuel envelopes the oxidiser. The study by GuoBiao, et al. (2016) quantifies the swirl intensity by a dimensionless number (S). This dimensionless number gives a relation between the tangential momentum and axial momentum as, GuoBiao, et al. (2016):

$$S = \frac{G_\Theta}{G_x} = \frac{\int_0^R (V_\Theta r)\rho v_x 2\pi r dr}{R\int_0^R (\rho V_x^2 + p) 2\pi r dr} \quad 2.127$$

Where,

- V_x, is the axial velocity
- V_Θ, is the tangential velocity
- ρ, is the gas density
- R, is the oxidiser inner diameter
- p, is the static pressure

The study by GuoBiao, et al. (2016) further simplifies Equation 2.127 by using injector geometry parameters, GuoBiao, et al. (2016):

$$S = \frac{\pi r_i R}{A} \qquad 2.128$$

Where,

- A, is the total area of the tangential holes through which the oxidiser is injected to achieve swirl flow.
- r_i, is the offset between the center line and the tangential holes and the axial line of the swirl cavity GuoBiao, et al. (2016).

The swirl method is investigated and compared to the coaxial flow of propellants. Its efficiency is quantified and compared to all other cases investigated in this study. The manner in which swirl is applied to the current study will be further discussed in Section 3.

2.7 Turbulence Vorticity

The vortex stretch mechanism is responsible for transferring energy from large to small scales. This is done through energy cascading and the generation of small scale vortical structures, Yang (2004). The vorticity transport and vorticity magnitude equations are considered to quantify its influence in turbulence. The vorticity transport equation is given as, Yang (2004):

$$\frac{D\omega}{Dt} = (\omega \cdot \nabla)u - (\nabla \cdot u)\omega - \nabla\left(\frac{1}{\rho}\right) \times \nabla p + \nabla \times \left(\frac{1}{\rho}\nabla \cdot \tau\right) \qquad 2.129$$

While the vorticity magnitude is given as, Yang (2004):

$$\frac{D(\omega\cdot\omega)}{Dt} = 2\omega\cdot(\omega\cdot\nabla)u - 2(\nabla\cdot u)\omega\cdot\omega - 2\omega\cdot\nabla\left(\frac{1}{\rho}\right)\times\nabla p + 2\omega\cdot\nabla\times\left(\frac{1}{\rho}\nabla\cdot\tau\right) \quad 2.130$$

As elaborated by Yang (2004) D/Dt is the substantial derivative while the vortex stretching and titling are represented by the right hand side first term. Volume dilation is represented by the second term and baroclinic torque is represented by the third term. Viscous dissipation is represented by the fourth term. The study by Yang (2004) illustrates that all the terms except for viscous dissipation contributes to the vorticity magnitude. This was defined at a characteristic length where, $\frac{x}{D_{inj}} = 2$. It further illustrates that baroclinic torque that is generated by the misalignment between the pressure and density gradients, rivals the stretching and titling term in the vorticity magnitude. This illustrates the influence of density stratification on vorticity production. The study further highlights that the vortex stretching and titling contribution is evenly distributed. While for the azimuthal vorticity, the baroclinic term has a strong influence on the injected propellants. In the ambient fluid field, the viscous dissipation and stretching are dominant. It is identified that the volume dilation contribution is small, Yang (2004).

Yang (2004) further illustrates that at an axial position of $\frac{x}{D_{inj}} = 5$ the baroclinic torque and viscous dissipation rival in magnitude and have opposite effects on the vorticity. These terms peak in regions with large density gradients where a high degree of mixing occurs. The study by Okong’o, et al. (2002) found that vorticity production occurs on the light fluid side. The study by Yang (2004) outlines that the vorticity core shifts slightly toward the dense fluid as ambient pressure increases but mainly remains on the ambient gas side as the mixing region changes in the radial direction. The three vorticity terms increase due to increase in vertical motions as the ambient pressure increases.

2.8 Shear Layer

The study by Schadow, et al. (1992) investigates flow instabilities and vortex shedding in constant – density shear layers. As discussed by Yang (2004) the work of Schadow, et al. (1992) illustrates the initial vortex shedding frequency, f_1, can be scaled with the characteristic velocity $\bar{U}$ and shear layer momentum thickness θ_0. The relation produces the non-dimensional frequency or Strouhal number, $St_i = f_i \theta_0 / \bar{U}$. Yang (2004) illustrates that the analysis of the Strouhal number can be applied to mixing layers in axisymmetric configurations if the radius of the injector is larger than the thickness of the shear layer. It further outlines that the frequency of the most unstable case exhibits low pressure dependence at high pressures. There is however a significant decrease in the near – critical regime this is due to the increased mixing layer momentum thickness and the density stratification Yang (2004).

3. Methodology

This study aims to improve the prediction accuracy of the aspects regarding the turbulent, kinetic thermo - chemistry. Providing a safe operating gaseous oxygen (GO2) gaseous hydrogen (GH2) CFD model through numerical validation and verification that can be applied in the industrial design process. The CFD model aims to identify design limitations and associated improvements. This will eliminate the time and cost to fabricate and test physical models. It will therefore allow the basic engineering design phase of the coaxial injector to be completed before a hot fire physical model is tested. A typical rocket engine injector assembly would consist of hundreds of coaxial injectors. The simulation thereof would require excessive computational time and be very power intensive. Therefore only a single coaxial injector is investigated in the current study. This study focuses on the flow field domain in a single element coaxial injector model of a rocket engine that involves highly turbulent, chemically reacting fluid flow.

An investigation into the complex fluid dynamics and combustion processes involved, could improve CFD modelling accuracy by using the predicted heat load, combustion length and combustion efficiency as key performance indicators in rocket engine design. The verification and validation will be completed by using the experimental results of wall heat flux in the combustion chamber and compare it to the CFD model. The physical model experimental results that will be used is that of the Pennsylvania State University test case in which a rocket engine combustion chamber was designed for the validation of wall heat flux Marshall, et al. (2005).

The development and testing of GO_2/GH_2 single element coaxial injectors are expensive and time consuming. The application of CFD modelling to the practical test rig is affordable and efficient to investigate physiochemical phenomena associated with the complex O_2 – H_2 combustion process. The restriction of the application of CFD modelling in the design of injectors is due to minimum CFD code validations and low accuracy thereof. Calhoon, et al. (1973) investigated the gaseous injector performance for the auxiliary propulsion systems (APS). The key performance indicators of the injector performance included shear mixing, impingement and swirl mixing in cold flow testing. The results of these tests were used to define flow characteristics of different injector element types and consequently the effect of mixing on the combustion process. The cold flow tests defined the fluid flow characteristics which were used to define the injector performance, rate of heat transfer and reaction kinetic stability under hot fire testing. The Pennsylvania State University test case in the study by Marshall, et al. (2005) where a physical experimental model is developed and widely cited, conducts wall heat flux measurements in a cylindrical combustion chamber using a single coaxial injector. The experimental model includes a preburner for the fuel and oxidiser respectively. This configuration achieves supercritical states of the gasses that corresponds to the staged combustion cycle. The study focuses on achieving the accurate heat transfer profile with the associated gas flow rates.

3.1 Approach

The first step towards meeting the research objectives will be in creating a computer model of the coaxial injector. The geometry is to be based on the experimental model coaxial injector by the study of Marshall, et al. (2005). The model will be used as basis for the boundary conditions for the developed flow field in the injector including the areas of interest for the investigation of the different physiochemical processes. Figure 2 illustrates an extract of the experimental geometry used for the current study from Tucker, et al. (2008).

The current study will utilise large – eddy - simulation to investigate the high pressure cryogenic fluid injection and extent of mixing dynamics of a single element GH_2/GO_2 coaxial injector. To maintain simulation feasibility the Large-eddy – simulation (LES) will be utilised since this turbulence numerical simulations are less computational intensive than direct numerical simulations (DNS). The proposed research will address challenges that include thermodynamic non-idealities, highly turbulent flow and highly reactive chemical kinetics in an approach that is similar to current experimental efforts. The proposed research will focus on detailed fluid dynamic representation and thermo physical processes. The research will entail the determination of a theoretical framework and accurate property evaluation with closure methodologies. Additionally the proposed research will develop a numerical model for the multiphase turbulent fluid dynamics in which real fluid thermodynamics are accounted for, including the high variation of pressure.

The focus is placed the GO_2/GH_2 propellant mixture in coaxial injectors. The variation of propellant flow rate, combustion chamber pressure and propellant momentum flux ratio will be investigated and the effects on rocket injector performance assessed. The momentum flux ratio can be defined as the momentum ratio between the fuel and the oxidiser. The main chemistry reactions that will be focused on in the proposed research is the H_2-O_2 reactions given by Turns (2000) in Section 2.4.

The experimental data used for the current study was generated by using the Pennsylvania State University shear coaxial test rig. The schematic in Figure 2 represents a general arrangement drawing of the test rig and consists of an oxidiser and fuel preburner. The test rig consists of a single element shear coaxial injector and a heat sink main combustion chamber with thermocouples to measure the temperature along the axial direction. The test rig was designed to determine the generated axial heat flux profile along the combustion chamber wall and measure the wall temperature that will be used to set the boundary conditions for simulations. More detail regarding the boundary conditions and the geometry are shared in Section 4 of this study.

The coaxial injector design for the current study was modelled in 3D using CFD. The combustion chamber has been included in the model but multiple injection elements will not be modelled in order to keep the generated flow field characteristics as simple as possible. The software that was used for the proposed research was STAR-CCM+ version 12.06.010 and version 13.06.011.

The study by Chuech, et al. (2004) illustrated that symmetry within the flow field domain is one of the major limitations to accurately determine the flow domain. This is due to the highly turbulent wave instability present in the flow domain and fine grid distribution required for accurate numerical modelling. This study by Chuech, et al. (2004) analysed the wave instability in order to predict the growth rates along the gas streamlines. To achieve this, the wave dispersion equation was numerically solved while the governing equations of the flow dynamics were solved for the formation of the jet core and variation of the flow structure. Furthermore, the fine grid distribution required will result in the numerical model being computationally intensive.

The variation of the injector feed flow rate will be numerically modelled to generate the flow field over the temperature and pressure regimes in the entire flow domain. At this stage, the flow field characterisation in the combustion chamber will be modelled as well.

The combustion process in the injector is highly exothermic, however, the thermal effects of combustion on the injector material will not be investigated in this study. The temperature field in the flow domain will greatly affect the flow characteristics of the super critical state propellants. It is therefore evident that a model for the temperature field will have to be produced.

With the geometry of the injector and the base level propellant fluid flow rate modelled and validated it will be used for the initial development of the CFD code to quantify the flow domain and the array of physiochemical phenomena. With the flow field domain modelled, the distinct flow regimes will be fed back to the flow profile and jet characteristics as well as momentum flux which are influenced by the injector design. The resultant flow field domain at this stage will be used to examine the flow and flame dynamics of the coaxial injector. Therefore, producing a more realistic model where the injector geometric parameters and flow conditions can be identified that influences the injector performance.

In order to verify the numerical model by determining whether the computational model accurately represents the underlying mathematical model. The solution as referenced in ASME-NAFEMS-2004 is required to establish confidence in the computational model by carrying out two fundamental processes which include:

- Code Verification
- Calculation Verification

Code Verification requires that the mathematical model and solution are working correctly while Calculation Verification requires the discrete solution of the mathematical model to be accurate. The Code Verification and Calculation Verification will be conducted by comparing the model to the findings of (Zhukov, 2015) in which an efficient CFD model for wall heat flux has been developed. A grid independence study will be conducted to estimate the amount of error in the numerical solution that can be attributed to discretisation. The rate of convergence of the solution will be compared at two or more discretisation (meshes). Therefore, refining the mesh to ensure that the algorithms are implemented correctly. To achieve grid independence, the coaxial injector 3D CFD mesh will be compared to the mesh convergence and mesh independent solution presented in the study by (Zhukov, 2015). A Grid Convergence Index method by Coleman, et al. (2008) will be further used to evaluate the mesh independence. Figure 2 below is an extraction of the presentation by Coleman and Roache, 2008, of the modelling flow scheme that will be followed in order to achieve simulation model validation and verification:

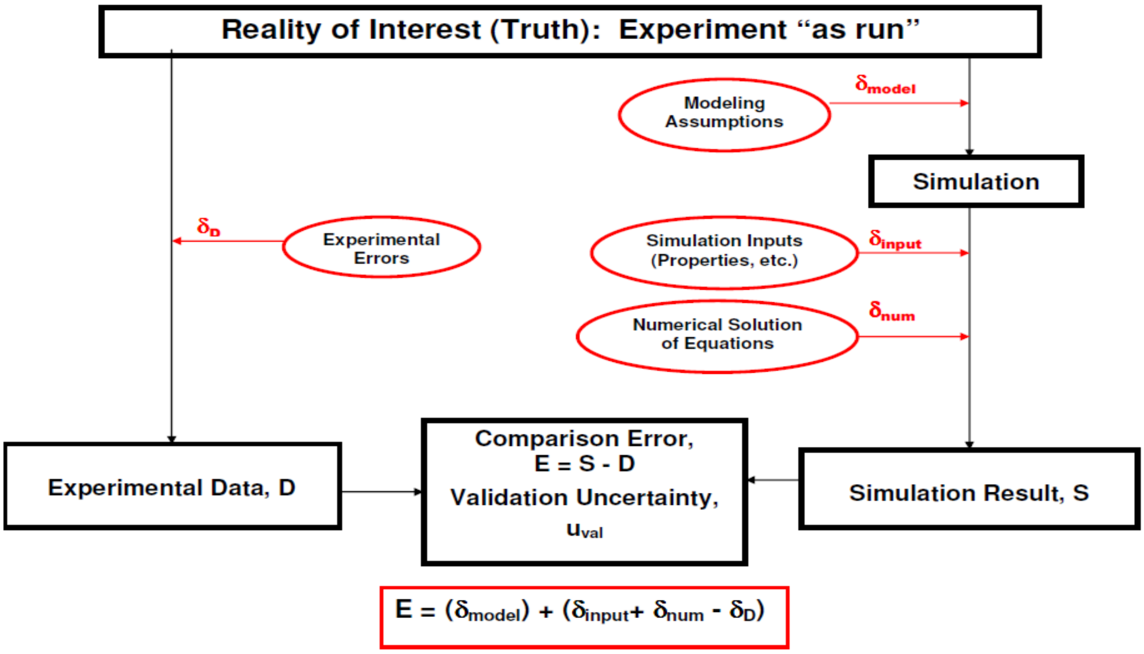

Figure 1: Validation and Verification Flow Schematic presented by H. Colman, 2008. Extracted from the presentation by H. Coleman 2008 in which P. Roache is referenced as consultant.

In order to validate the numerical model it is required that the model be an accurate representation of the physical model and its intended purpose. The physical experimental results that will be used to assess the adequacy of the selected Conceptual and Mathematical models of the coaxial injector will include the study by W.M. Marshall, et al. (2005).

The final results of the model should include the flow development inside the injector, jet dynamics dictated by the local thermodynamic state and intra element mixing efficiency for a given set of flow conditions. The results of Conely (2006) will be further used to validate the CFD code at each of these stages.

4. Experimental Setup

The following section will discuss the physical and numerical experimental setup used to develop the CFD models. The physical experimental setup will give insight into the design geometry and operating conditions. The setup of the numerical CFD models will discuss the manner in which the program software is utilised to generate the fluid flow domain in the coaxial shear injector for further analysis. The setup of the CFD models will be discussed as well as the method used to achieve mesh grid independence. The validation of the numerical results to the experimental results will be further discussed in this section.

4.1 Physical Experimental Setup

The geometrical detail, operating conditions and experimental results of the CFD model of this study will be based on the physical experimental model developed by Marshall, et al. (2005). The wall heat flux data generated during this study will be used as benchmark for the single element GO_2/GH_2 injector numerical model. The experimental data formed part of the Full – flow staged-combustion (FFSC) cycle engines which at the time of the study was considered part of the NASA Reusable Launch Vehicle (RLV). Like the current study, the study by Marshall, et al. (2005), used gaseous oxidiser and fuel propellants to be injected into the combustion chamber. The study indicates that the benefits of FFSC include simplicity and increased thrust to weight ratio when compared to other closed cycles.

The Cryogenic Combustion Laboratory at the University of Pennsylvania conducted rocket combustion chamber tests which provided the experimental data used for the current study. The test rig illustrated by Figure 2 is a shear coaxial injector that contains oxidiser and fuel preburners. Further design detail is listed in Table 1. The test rig is configured in order to easily make changes to the combustion chamber length or information sensor hardware. The preburners are designed to be bolted perpendicular onto the main combustion chamber. Taking into account the main axis of the rocket combustion chamber. Before being injected into the main combustion chamber the fluid flow from the preburners turns at an angle of 90°. As described by Marshall, et al. (2005) the material of construction of the rocket combustion chamber is that of oxygen – free high conductivity (OFHC) copper. The chamber inner diameter is 38.1mm while the chamber length is defined as 285.7mm. The test rig allows for operating pressures up to 1000psia and a water cooled nozzle. The design of the nozzle allows for fuel and oxidiser (H_2 and O_2 respectively) operation to be near stoichiometric conditions of 3282.2°C.

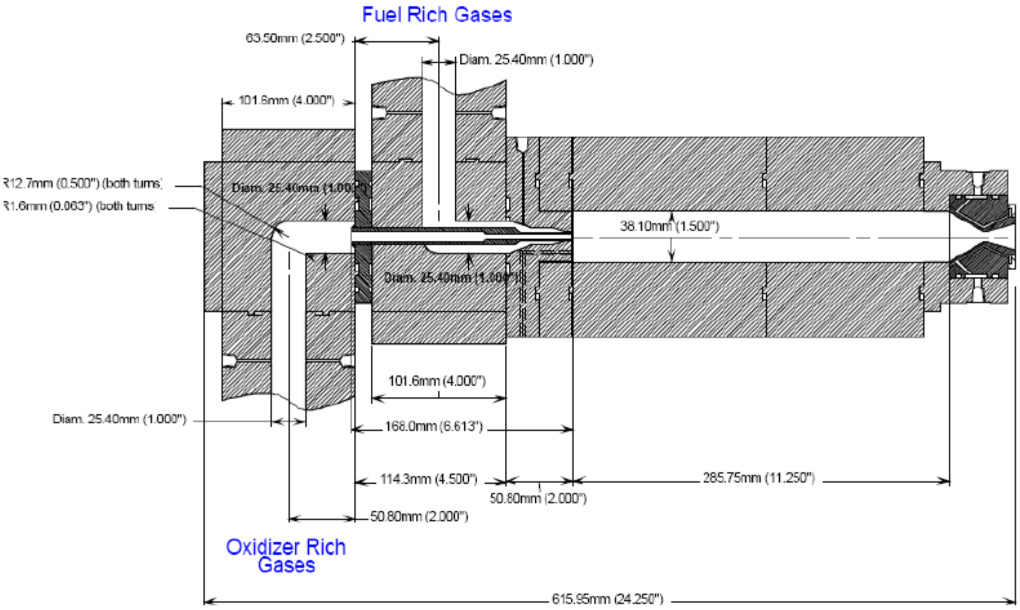

Figure 2: Experimental geometry of the shear coaxial single element. Extracted from Validation of High - Fidelity CFD Simulations for Rocket Injector Design, P.K. Tucker et al, 2008.

Table 1: Geometry detail of the shear coaxial injector.

Design Parameter	**Dimension (mm)**
Oxygen post recess length	0.43
Fuel annulus outer diameter	7.49
Fuel annulus inner diameter	6.3
Oxygen post inner diameter	5.26
Nozzle throat diameter	8.17

The study by Marshall, et al. (2005) further illustrates the adaptability of the test rig. It is further illustrated being able to change the combustion chamber pressure for a given total propellant mass flow rate. This is achieved by the design of the water cooled nozzle that allows the interchange of different diameter nozzles. Ignition of the main chamber flow is achieved with a GH_2/GO_2 torch igniter. The material of construction for the oxidiser preburner with Monel was chosen based on safety. Since Monel will resist burning in an oxygen rich environment. The material of construction of the fuel preburner is the same as the combustion chamber which is selected as OFHC copper. The preburners were designed to achieve near-stoichiometric core/downstream dilution philosophy. To achieve the near – stoichiometric mixture ratios the preburners consist of impinging element injector that is upstream. Furthermore the hot gas from the stoichiometric core is diluted with GH_2 for the fuel preburner and GO_2 for the oxidiser preburner. The fluid flow from the preburners is routed at a 90° bend before it is injected into the combustion chamber. Upstream of the dilution injectors the preburners inner diameter is 12.7mm while from the dilution injectors to the injector the inner diameter is 25.4mm. The oxidiser and fuel preburner is 304.8mm long and are ignited using GH_2/GO_2 torch igniters.

Further detail regarding the preburner is outlined by Marshall, et al. (2005) in which the near – stoichiometric core injector achieves dilution by injection through holes in the wall in a radial direction. The fuel preburner near –

stoichiometric impinging injector is a fuel centered pentad. It consists of a central hole for fuel that is surrounded by four 30° centrally angled holes. In contrast to the fuel preburner, the oxidiser preburner near – stoichiometric impinging injector consists of six 20° centrally angled holes surrounding the central hole for fuel. The preburners operate with GO_2 flowing through the angled holes while GH_2 flows through the central element, Marshall, et al. (2005).

As mentioned by Marshall, et al. (2005), temperature control at the nozzle throat is achieved by using a high flow rate water cooled nozzle design. The nozzle shape is 15° half angle with OFHC copper being the material of construction. The nozzle wall, especially at the nozzle throat, has water flow passages to achieve temperature control by entering these passages along the nozzle radial edge. It passes through the passages and exits through stainless steel tubing soldered around the nozzle exit. In order to accommodate different nozzle throat diameter designs, the water cooled nozzle assembly is modular in design, as was mentioned for the combustion chamber. The propellants in the preburners and the combustion chamber are ignited by identical GO_2/GH_2 torch igniters. Ignition is achieved by a spark plug driven by an oil furnace ignition transformer while GO_2 and GH_2 are injected off axis into the igniter. A pressure rise in the igniter combustion chamber indicates that ignition has been achieved. Before any propellants are routed to the combustion chamber, the pressure rise in the igniter is checked. The propellant flows in the preburners and main combustion chamber are ignited when hot gas from the igniters flow into the integrated assembly.

Table 2, extracted from Tucker, et al. (2008), lists the boundary conditions of the oxidiser and fuel streams of the experimental test rig regarding the stream composition, reference properties and flow characteristics.

Table 2: Experimental test rig boundary conditions. Extracted from Validation of High-Fidelity CFD Simulations for Rocket Injector Design by P. Tucker et al (2008).

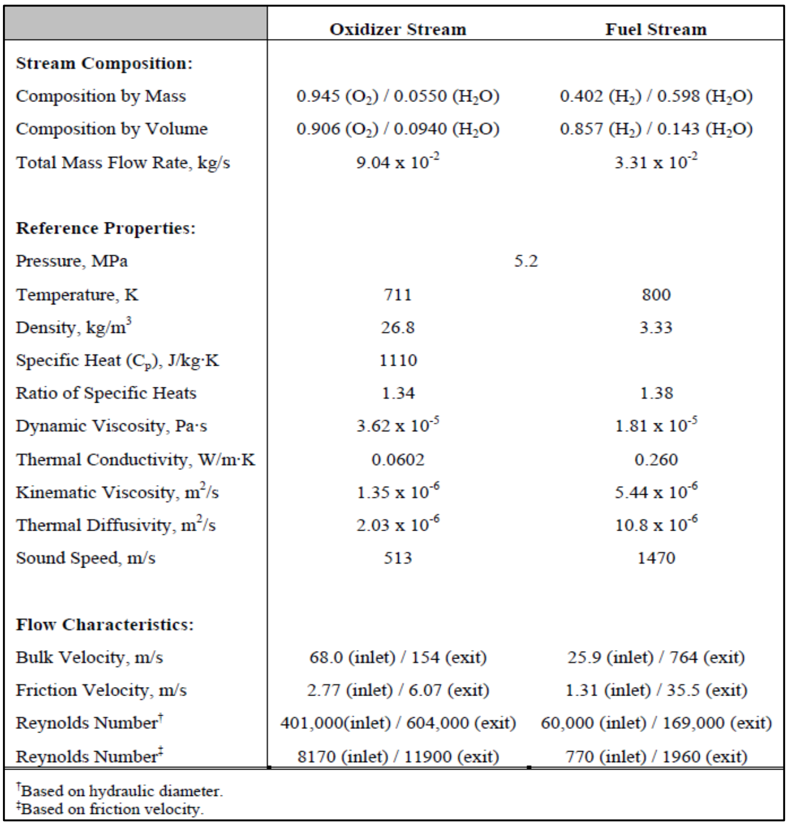

	Oxidizer Stream	Fuel Stream
Stream Composition:		
Composition by Mass	0.945 (O_2) / 0.0550 (H_2O)	0.402 (H_2) / 0.598 (H_2O)
Composition by Volume	0.906 (O_2) / 0.0940 (H_2O)	0.857 (H_2) / 0.143 (H_2O)
Total Mass Flow Rate, kg/s	9.04×10^{-2}	3.31×10^{-2}
Reference Properties:		
Pressure, MPa	5.2	
Temperature, K	711	800
Density, kg/m^3	26.8	3.33
Specific Heat (C_p), J/kg·K	1110	
Ratio of Specific Heats	1.34	1.38
Dynamic Viscosity, Pa·s	3.62×10^{-5}	1.81×10^{-5}
Thermal Conductivity, W/m·K	0.0602	0.260
Kinematic Viscosity, m^2/s	1.35×10^{-6}	5.44×10^{-6}
Thermal Diffusivity, m^2/s	2.03×10^{-6}	10.8×10^{-6}
Sound Speed, m/s	513	1470
Flow Characteristics:		
Bulk Velocity, m/s	68.0 (inlet) / 154 (exit)	25.9 (inlet) / 764 (exit)
Friction Velocity, m/s	2.77 (inlet) / 6.07 (exit)	1.31 (inlet) / 35.5 (exit)
Reynolds Number†	401,000(inlet) / 604,000 (exit)	60,000 (inlet) / 169,000 (exit)
Reynolds Number‡	8170 (inlet) / 11900 (exit)	770 (inlet) / 1960 (exit)

†Based on hydraulic diameter.
‡Based on friction velocity.

4.2 Computational Domain

The oxidiser flow stream contains 0.906 moles of oxygen, 0.0940 moles of water and enters the combustion chamber at a temperature of 711K. The fuel stream contains 0.0.857 moles of hydrogen, 0.143 moles of water and enters the combustion chamber at a temperature of 800K. User defined functions with input of the information represented in Table 2 achieved constant flow rates at the inlets of 0.0904kg/s for the oxidiser and 0.0331 kg/s for the fuel. The measured axial temperature profile along the radial wall of the combustion chamber is achieved with temperature measurements at the combustion chamber wall. This information could be used as input into the isothermal boundary condition. Tucker, et al. (2008) utilised the least squares fit method to approximate the temperature distribution (illustrated in Figure 3). The boundary conditions including the wall temperature distribution used for the current study are illustrated by the figure below. The computational domain consists of a 90° section of the single element coaxial injector. The two sides of the model are set as rotational periodic boundaries.

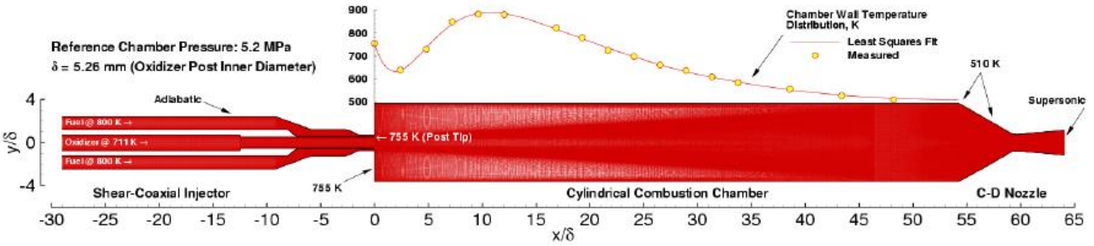

Figure 3: Schematic of the simulation boundary conditions and the computational domain. Extracted from Validation of High-Fidelity CFD Simulations for Rocket Injector Design by P. Tucker et al (2008).

An adiabatic boundary condition is applied at the wall of the injector while no-slip conditions are applied at all wall surfaces. At the nozzle exit supersonic boundary conditions are applied. At the head of the combustion chamber and oxidiser post tip the temperature is uniform at 755K. The least squares fit method used by Tucker, et al. (2008) assumes the nozzle temperature of 510K which is consistent with the curve fit (see Figure 3). This is the temperature achieved at the end of the combustion chamber with a zero gradient. The fluid flow velocity is 154m/s (oxidiser) and 764m/s (fuel) at the chamber reference pressure of 5.2MPa.

4.2.1 Computational Grid Generation

One of the key objectives of the current study is to develop a mesh sufficiently accurate to predict the experimental results. In order to achieve this, first the grid has to be generated with the necessary inputs based on the finite volume method. After which it is necessary to refine the grid in order to achieve mesh grid independence. A 3D model was developed and the areas of refinement included the areas in which high property gradients would be achieved. To confirm the flow symmetry of the selected periodic boundaries, the 3D model fluid flow analysis was analysed in terms of:

- Propellant composition
- Temperature profile
- Velocity profile
- Density profile

In order to proceed with a 90° element that accurately presented the simulated rocket injector model. After the refinement of the mesh was completed, a 90° element could be used to achieve simulation result convergence. By doing this, the CPU time required could be reduced.

The aspects used from the STAR-CCM+ 13.06.011 Pre-Processing Guide (2019) to assess the overall mesh quality includes:

- Mesh Density – in the expected areas of high property gradient, the mesh has been sufficiently refined to represent the flow features accurately
- Mesh Distribution – the distribution of the mesh and mesh transition has been optimally generated between the high and low gradient areas
- Near Wall Layers – the mesh near – wall layers have been included in the model to account for turbulence and heat transfer effects

For the current study including the oxidiser and fuel fluid flow, the mesh quality has a significant impact on the accuracy of the convective and diffusive fluxes. Therefore the following factors were investigated on the mesh cell level:

- Aspect Ratio – for the expected flow regime the ratio has been sufficiently refined
- y^+ Range – the y^+ values achieved were sufficient to illustrate that it is within the desirable range for the turbulence model
- Volume Ratio – the cell volume ratio to the adjacent cell is acceptable
- Skewness Angle – the mesh cell skewness was minimised in the grid generation

The simulations were conducted using a polyhedral mesh with mesh refinement near the walls, the injector post before entering the combustion chamber and the flame region. Mesh refinement was applied at the converging section of the nozzle and nozzle throat. An absolute target surface size of 0.34mm was specified at the nozzle throat while 0.85mm was specified at the converging section of the nozzle. Further refinement was applied around the shear layer between the jets of fuel and oxidiser. The final base cell size was set at 1.2mm with a minimum surface cell size of 0.05mm. A total of 2.04 million cells were used to resolve the computational domain. To ensure accurate wall heat flux prediction high mesh resolution was achieved near the walls. A minimum of 0.08mm cell base size for the mesh along the wall, which corresponded to $y^+ < 1$. Near the wall the stretching factor was set to less than 1.05 while the mesh density and growth factor was set to 1.2 and 0.8 respectively. Figure 4 represents a graphical illustration of the final mesh used as the base case for the current study. The computational domain of all simulations were solved by gaining access to the Centre of High Performance Computing (CHPC). The CHPC allowed the simulations to be run utilizing 5 nodes each with 24 cores running 24 mpi processes on a total of 240-way parallel. Thus allowing the implementation of parallel computation with message passing technique (mpi) in the fluid flow domain. This enabled simulation convergence to be reached after 6 hours of run time. The total amount of CPU – hours required to complete all necessary and investigated numerical simulations was 65 541.

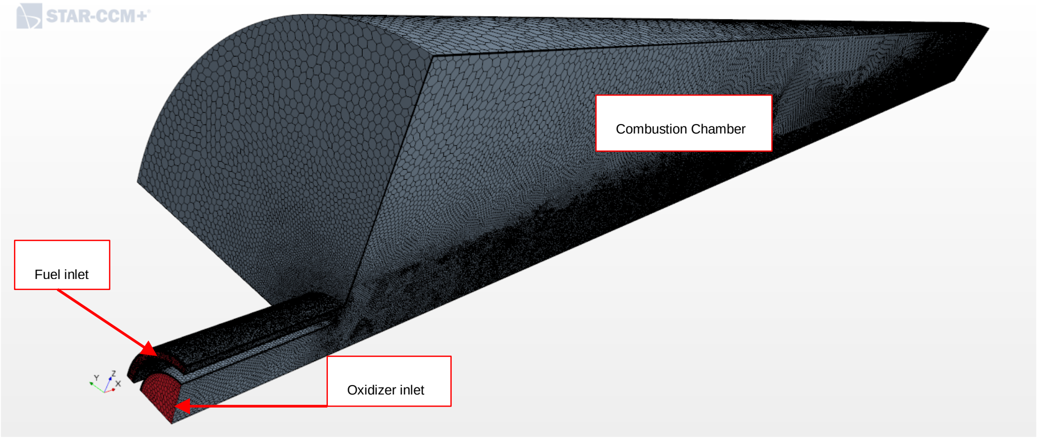

Figure 4: Base case mesh at cell size of 1.2mm resulting in 2.04million cells.

4.2.2 Turbulence Model and Thermodynamic Setup

The numerical modelling of the thermodynamic properties, turbulence and chemical reactions to an acceptable level of accuracy represents a major challenge in the current study. The flamelet method was assessed in the current study based comparison between the Kolmogorov time scale and the chemical time scale. The study by Zong et al (2007) investigated the liquid oxygen (LOX) and methane (CH_4) combustion dynamics in order to evaluate the suitability of the flamelet method to supercritical LOX/CH_4 combustion. It illustrated that the Kolmogorov time scale remains one order of magnitude greater than the chemical time scale. In the study by Zong et al (2007) the Reynolds number was 76000 while for the current study based on the oxidiser inlet and friction velocity the Reynolds number is 8170. Hydrogen reacts faster than methane and the flame profile is narrower than that of methane. Therefore it was decided to proceed with the use of the flamelet model only where laminar properties are predominant and to identify the flame surface within the flow field. Due to the high degree of turbulence in the current study it was found that the flamelet model predict a low percentage of cells within the flow domain with sufficient level of accuracy and therefore an alternative method had to be considered for the remainder of the flow domain.

The turbulent flame can be considered as a region of reaction zones within an inert turbulent fluid flow domain. As discussed by www.cfd-online.com (2019) the Mathur-Saxena Averaging method was used where the shear stress transport (SST) k-ω model is applicable to accurately represent the flow domain. The SST k-ω model is applicable throughout the flow domain up to the wall. It can thus accommodate low Re turbulence modelling without the requirement of extra damping factors. The k-ω model is sensitive to the inlet free stream turbulence properties and therefore the SST formulation can adapt to k-ε behavior in the free stream. Illustrating this method is suitable in the current study with high pressure and density gradients. Additionally, when considering the study by Ribert et al. (2008), the O_2/H_2 flame is resistant to fluid flow dynamic strain. The current study has not considered the solution conditions at the flame extinction state.

The chemical reaction selection in the numerical model to represent the current study is imperative to produce a numerical model of a high degree of accuracy when compared to the physical experimental model results. The set of reactions used for the current study are represented in Section 2.4 and simplified to an 8 species (H_2, O_2, H_2O, OH, HO_2, H_2O_2, O and H) 19 reversible reaction model. The study by O'Conaire et al. (2004) validates the reaction mechanisms over a pressure range of 0.05 to 87 atmosphere with experimental data.

The thermodynamic property selection is elaborated on in Section 2. In this section the enthalpy and entropy have been defined for the GO_2/GH_2 system. Furthermore the dynamic viscosity and conductivity have been defined using Sutherland's Law and the Mathur-Saxena Averaging method. This method was followed due to the following parameters that had to be included for the current study:

- Dipole momentum

- Lennard – Jones characteristic length. To take into account the collision diameter
- Lennard – Jones energy. To take into account the potential energy of attraction

These parameters are of specific interest in the current study due to the small H_2 molecule. The averaging method uses the equation below (presented in the STAR-CCM+ 13.06.011 Pre-Processing Guide, 2019) to calculate the property on the mixture level that utilises values for the individual mixture components taking into account the mixture composition, STAR-CCM+ 13.06.011 Pre-Processing Guide, 2019:

$$\phi = \frac{1}{2}\left(\sum_1^n X_i\phi_i + \left(\sum_1^n \frac{X_i}{\phi_i}\right)^{-1}\right) \qquad 4.131$$

Where:

- Φ, is the property Mathur – Saxena Averaging property method
- Φ_i, represents the material property
- X_i, represents the mole fraction of component, i

4.2.3 Mesh Convergence Study

It is imperative that in the current study a mesh convergence study be conducted due to the large amount of scales present. It is therefore necessary that all scales are resolved and grid independence is achieved. The grid independence method by Roach et al (1998) was used to achieve this objective. This method determines a Grid Convergence Index (GCI) for the different solutions at the different mesh cell size. To relate the different mesh sizes a relationship is developed between the successive meshes by defining a constant grid refinement ratio (r). If the mesh is doubled in each dimension represented in the solution domain then r = 2. The current study utilised non – integer refinement and the grid refinement ratio was set at 1.3 for the successive meshes that followed from the coarse mesh case. As defined by Roach et al (1998) and ASME V&V 20 (2009) the objective of grid refinement is to achieve a numerical solution which is within the asymptotic range. This is achieved where the theory of Richardson Extrapolation is asymptotically valid.

The parameter used to compare the numerical model to the experimental model is, wall heat flux (MW/m^2). The wall heat flux is calculated by using the correlation presented in Huo (2011):

$$\dot{q} = (k_{lam} + \ k_{turb}) \frac{dT}{dr}|_w \qquad 4.132$$

The temperature measured at the wall is distributed as represented in Figure 3. As discussed by Huo (2011), from Equation 132 the heat flux is calculated by the sum of the molecular and turbulent conductivity and the temperature measurement at the wall. Based on the velocity profile in the flow domain the turbulent conductivity is calculated. While based on the gas composition at the near wall region, the laminar conductivity is calculated. In Section 5 the temperature distribution, streamline and species concentration are evaluated and the affect thereof assessed to elaborate on further improvement.

To illustrate how the GCI is determined the wall heat flux parameter will be represented as, f. However it should be noted that for the current study the wall heat flux is measured at various locations along the axial direction of the model. In order to accurately represent the flow domain, each of the data points were compared to experimental model and the GCI calculated respectively. Therefore the experimental results have 15 represented data points which will be used. For the current study three different successive converged numerical solutions were considered, therefore producing f_1, f_2 and f_3. Where the finest mesh is associated with f_1. The information available from these numerical solutions can be used to calculate the order of convergence (p), Roach et al (1998) and ASME V&V 20 (2009):

$$p = \ln\left(\frac{f_3 - f_2}{f_2 - f_1}\right)/\ln(r) \ , \qquad 4.133$$

Using the Richardson Extrapolation and neglecting higher – order terms produces the wall heat flux parameter (represented by f) at zero grid spacing, Roach et al (1998) and ASME V&V 20 (2009):

$$f_{h=0} = f_1 + \frac{f_1 - f_2}{r^p - 1} = \frac{r^p f_1 - f_2}{r^p - 1} \qquad 4.134$$

The fine GCI is defined as, Roach et al (1998) and ASME V&V 20 (2009):

$$GCI_{fine} = \frac{F_s|\varepsilon|}{r^p - 1} \qquad 4.135$$

Note from Equation 135 that a safety factor, F_s, has been included which is set at 1.25 when a minimum of 3 numerical solutions are used. While the relative error, ε, is represented as, Roach et al (1998) and ASME V&V 20 (2009),

$$\varepsilon = \frac{f_2 - f_1}{f_1} \qquad 4.136$$

For the mentioned 3 numerical solutions that will be used to achieve grid independence the GCI can be calculated for the successive points as, Roach et al (1998) and ASME V&V 20 (2009):

$$GCI_{1-2} = \frac{F_S\left|\frac{f_2-f_1}{f_1}\right|}{r^p-1} \tag{4.137}$$

$$GCI_{2-3} = \frac{F_S\left|\frac{f_3-f_2}{f_2}\right|}{r^p-1} \tag{4.138}$$

If the asymptotic range of convergence has been achieved, Roach et al (1998) and ASME V&V 20 (2009):

$$GCI_{2-3} \approx r^p GCI_{1-2} \tag{4.139}$$

Illustrating that if mesh grid independence has been achieved, Roach et al (1998) and ASME V&V 20 (2009):

$$\frac{GCI_{2-3}}{r^p GCI_{1-2}} \approx 1 \tag{4.140}$$

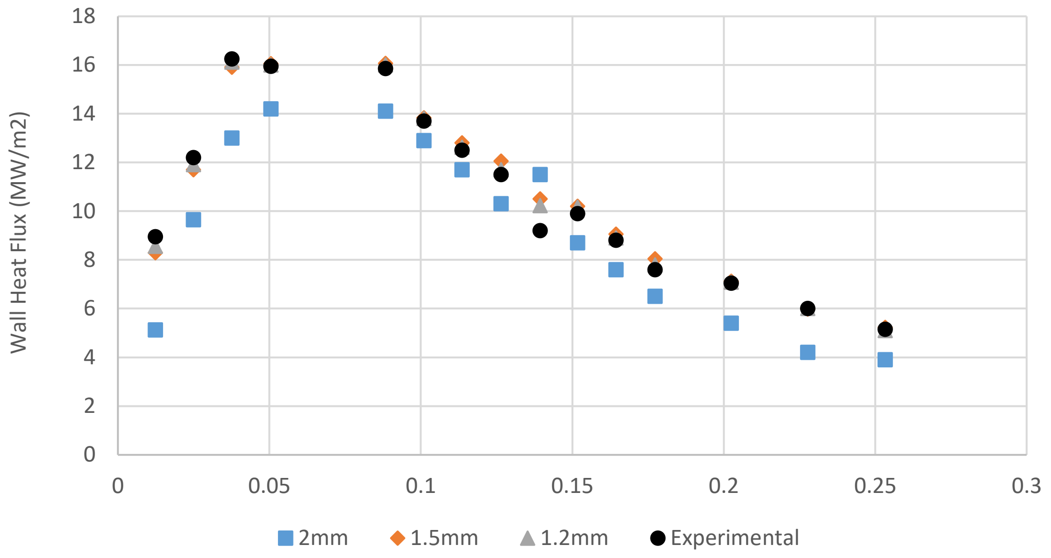

Figure 5: Numerical solution of the wall heat flux at different mesh base cell size. Experimental results extracted from Computational Fluid Dynamics Simulations of a GO2/GH2 Single Element Combustor by Zhukov (2015).

Figure 5 illustrates the numerical solution achieved at different mesh base cell size. Note that the numerical solution accuracy increases in an increase in mesh density and near wall resolution to minimise the y^+ - values. The finest mesh grid (1.2mm base cell size) has 2.7 times the number of cells than that of the coarse mesh (2mm base cell size). The illustration indicates that mesh grid independence was possible to be obtained in the current study with a final mesh that consists of 2.04million cells and a near wall resolution of $y^+ < 1$. The 1.2mm and 1.5mm GCI ratio achieved was 1.086, further indicating that mesh grid independence has been achieved. The mesh grid independence and high degree of accuracy to that of the experimental results, validates the final mesh size selection of 1.2mm to be used as base case for the current study.

5. Results and Discussion

The following section will discuss the results obtained throughout the various numerical solutions achieved at different design parameter optimisations. Firstly, the base case of the current study will be elaborated on and the validation thereof compared to previous research. The section illustrates how the current study provides insight into how CFD can influence the design process of the rocket injector. The study by Tucker et al. (2007) validates different numerical solutions and compares each numerical solution's accuracy to the physical experiment. This study's results will be used to compare the base case of the current study and the level of accuracy that the numerical model achieves.

As discussed by Huo (2011), the lack of detailed experimental data due to extreme operating conditions that imposes challenges to accurately measure process data makes it challenging to validate CFD numerical models for supercritical combustion studies. The CFD models presented by Tucker, et al. (2007) illustrate the inherent accuracy and numerical difficulty that these models have for supercritical turbulent combustion cases. The uncertainties in modelling turbulence combustion and the chemical reaction interaction associated with the GO_2/GH_2 rocket injector system with multi scale physical processes illustrates the intricacies associated with the current study. Furthermore, the variation in the thermodynamic properties and species transport gradients as the propellants are injected into the combustion chamber and the propellants transition into the supercritical phase, further compounds the challenge on the numerical model to accurately predict the physical experiment.

The base case of the current study will be used for variations in structural design after the validation has been completed with a high degree of accuracy.

The current study evaluates the single element injector in the following sections:

- Design parameter optimisation of the injector with applied oxidiser post recess length
- Introduction of centre oxidiser swirl flow to enhance mixing

5.1 GO_2/GH_2 Shear Coaxial Injector Base Case

The study by Tucker et al. (2008) investigates the validity of different numerical solutions that include:

- LES – Stoichastic Reconstruction Model (Sandia National Laboratories, SNL)
- LES – Kinetics with Sub – iteration Model (Georgia Institute of Technology, GIT)
- LES – Flamelet Model (The Pennsylvania State University , PSU)
- Unsteady RANS (Purdue University, Purdue)
- Steady RANS (Marshall Space Flight Center, MSFC)

As discussed by Tucker et al. (2008), the numerical solution by Oefelein is presented by the LES (SNL) with the LES (GIT) numerical solution conducted by Menon. The simulations were conducted in a 3D LES simulation model. A 2D axisymmetric LES model was developed by Yang which is represented by the LES (PSU) numerical solution. Similarly the numerical solutions of URANS (Purdue) and RANS (MSFC) were developed by Merkle and Tucker et al. (2008) respectively. Merkle developed a 2D axisymmetrical unsteady model while Tucker, et al. (2008) developed a steady RANS simulation. These studies are used as comparison to the current study in order for the current study to illustrate sufficient accuracy at an acceptable level of required computing power and time.

Huo (2011) presents the mesh density of these different studies which is given in Table 3.

Table 3: Mesh density of the different studies.

Study	**Total number of cells (million)**
Current Study	2.04
Menon (LES GIT)	3.5
Oefelein (LES SNL)	6.7
Merkle (URANS Purdue)	0.25
Tucker (RANS MSFC)	0.4
Yang (LES PSU)	0.26
Huo (2011)	225

It was evident throughout the refinement of the numerical model that different complexity levels were required to improve the base case accuracy. The current study numerical model used the 1.2mm base case cell size. This base cell size was selected after the mesh grid independence study was completed. A turbulence intensity of 5% was set at the propellants inlet boundary. It was found that the increase in this boundary condition did not significantly improve the accuracy of the numerical model. The injector nozzle outlet pressure was set to atmospheric pressure. While at the chamber walls the effect of radiated heat transfer was disregarded. One of the biggest contributors to improving the model accuracy was the definition of the transport properties. The dynamic viscosity and thermal conductivity was found to be strong influencers to the outcome of the wall heat flux term calculated in this study. As soon as the dynamic viscosity and thermal conductivity was defined as a function of temperature, to account for real gas behaviour and not assuming the gas molecules to react as hard spheres the accuracy improved significantly.

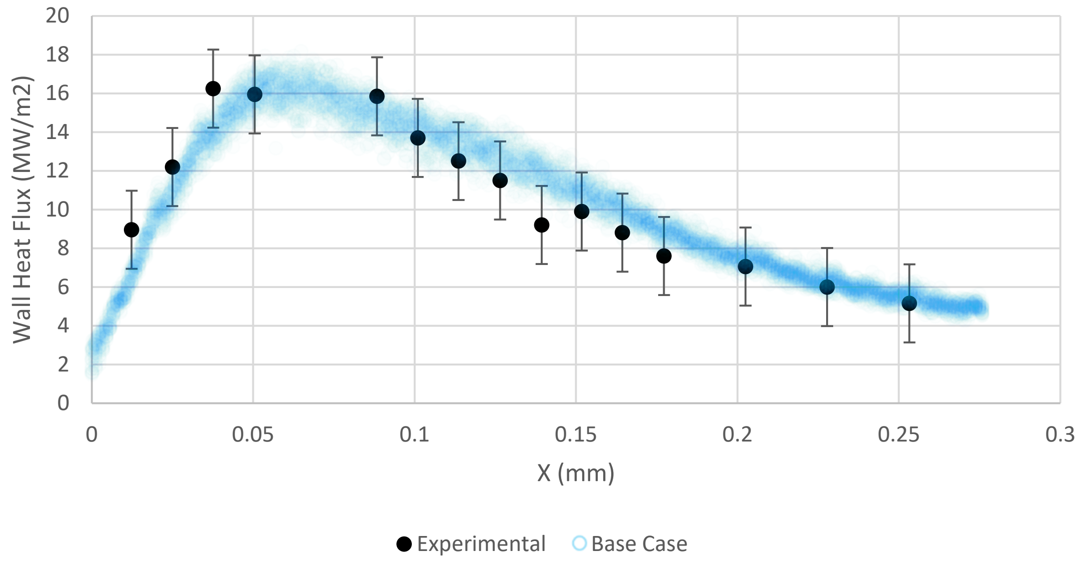

Figure 6: Base case data trend line of 95% confidence interval compared to the physical experimental results. Experimental results extracted from Computational Fluid Dynamics Simulations of a GO2/GH2 Single Element Combustor by Zhukov (2015).

Note from Figure 6 that the current study's base case at 1.2mm base cell size compares well to the experimental results. The light blue scatter trend line illustrates the actual simulation results while the black dots are the experimental results with 95% confidence interval included. Upon the propellants entering the combustion chamber the wall heat flux is low (<6MW/m^2). This is due to the shear layers that have not fully developed yet to promote mixing due to unstable flow. The base case achieves $\pi_1 = 19.01$ and $\pi_4 = 0.06$ with $\pi_2, \dots, \pi_{10}$ remaining constant, which will be used for comparison to the further test cases of this study. Additionally found in the base case was that the unstable flow during the initial simulation time exhibited an outer recirculation zone close to the injector face. The base case initial species composition was changed to be filled with nitrogen. This allowed for the region at the outlet of the injector to be at the same or higher pressure than the chamber upon the initiation of combustion. It was evident that this nitrogen blanketing of the injector improved the stability of flow but does not remove it. The presence of nitrogen does not allow the hot hydrogen propellant to react with residual oxygen in the chamber. This allows that the injected hydrogen propellant only reacts with the injected oxidiser. It could be that the propellants velocity is significantly changed during the initiation phase of the combustion process. As the propellants flow toward the injector it is possibly experiencing choke flow phenomenon. This would occur until the chamber pressure rises as the propellants flow into it. Upon ignition the chamber pressure increases and propellant velocity reduces until the nominal chamber pressure is reached. After the nominal chamber pressure is reached, the propellant velocity reaches its nominal operating condition. At this point the propellant flow is able to reach a steady state which was not possible during the pressure and velocity change. This illustrates the influence of recirculation zones on the steady state operating condition of the injector.

The numerical solution raw data achieves a cumulative error percentage of less than 5%. The cumulative error is determined by the square root of the sum of the each data point respectively, Zhukov (2015):

$$Error_{total} = \sqrt{\sum Error_i^2} \tag{5.140}$$

The numerical solution of Figure 6 predicts the wall heat flux well in the head-end region and achieves a peak of approximately 16.3MW/cm^2. In the downstream region there is one data point, at 0.14m, that is over predicted by 10%. If the 95% confidence interval is used. There are however raw data points that predict the wall heat flux at this axial location within an error percentage of 5%. The biggest contributors to the deviation include, chemical rate of extent of reaction, wall interference due to material erosion and experimental uncertainties. These uncertainties also include the initial conditions set for the simulation. These uncertainties are evident upon the initiation of the numerical model where unstable flow persist.

The numerical solutions of all the earlier mentioned studies and the experimental results are presented in Figure 7.

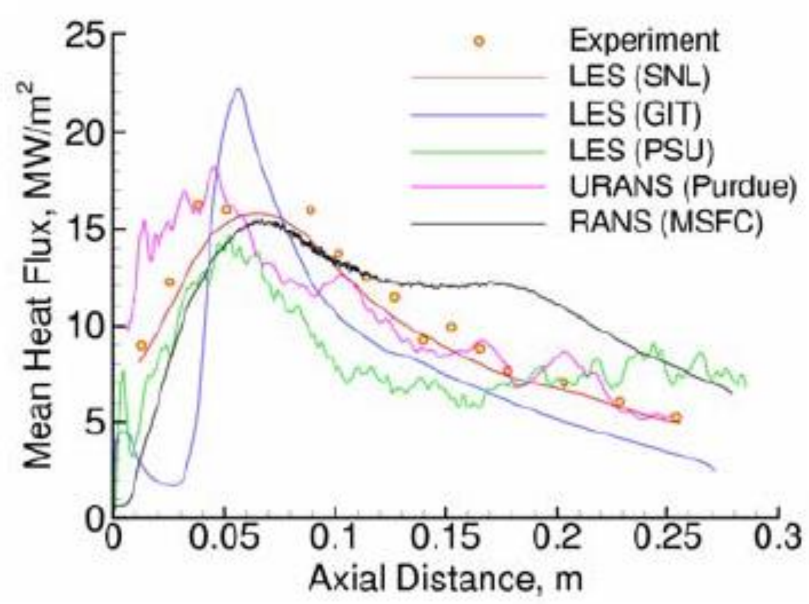

Figure 7: Numerical solutions of previous studies compared to experimental results. Extracted from Validation of High - Fidelity CFD Simulations for Rocket Injector Design, Tucker et al. (2008).

As the propellants are injected and begin to react close to the injector face (at an axial distance of less than 0.05m) there is a rapid increase in the heat flux. Tucker et al. (2008) refers to this section of the injector as the head-end region where, $0 \leq x \leq 0.1$ meters, where x denotes the axial distance. There is a steady increase in the wall heat flux up to an axial distance of 0.06m, followed by a gradual decrease downstream of the head-end region to the end of the combustion chamber. The heat flux peaks at approximately 16.5MW/m$^{2.}$ while it gradually reduces to 5MW/m^2 as the last measured experimental result. The rate of increase and the peak value of the heat flux are critical parameters to consider for injector design. To accommodate the material of construction of the combustion chamber. The rate of increase of the wall heat flux allows to make qualitative inferences on the rate of combustion and subsequently the injector efficiency. It is evident that the 3D numerical solutions are less erratic due to a large flow domain used to construct the numerical solution.

Note from Figure 7 that the 3D numerical solution by Oefelein (LES SNL) has the highest level of accuracy when compared to the experimental results. The remaining numerical solutions under predicts, like the study by Menon (LES GIT) and Tucker (RANS MSFC), by up to 50% when compared to the experimental result in the region of the head-end. While the numerical solution by Merkle (URANS Purdue) over predicts by up to 30% when compared to the experimental result in the head-end region. The study by Yang (LES PSU) under predicts the wall heat flux by approximately 20% in the head-end region with the peak value under predicted by approximately 12%. This numerical solution remains fairly constant downstream of the head-end region. The numerical solution of Merkle (URANS Purdue) and Yang (LES PSU) display similarities in the wall heat flux trend, while both these solutions are 2D axisymmetric, as outlined by Tucker et al. (2008) the differences between these two solutions in the head-end region can be contributed to differences in recirculation zones. It is clear that the Yang (LES PSU) solution under predicts when compared to the Merkle (URANS Purdue) solution in the head end region while further downstream the deviation between the two models are minimised. The numerical solution by Menon (LES GIT) has the highest wall heat flux peak value when compared to the other solutions. This numerical solution mainly under predicts at all the experimental data points up to 35%. At the peak however it over predicts by approximately 35% while at the downstream region the numerical solution under predicts similarly to that of Yang (LES PSU) and Merkle (URANS Purdue).

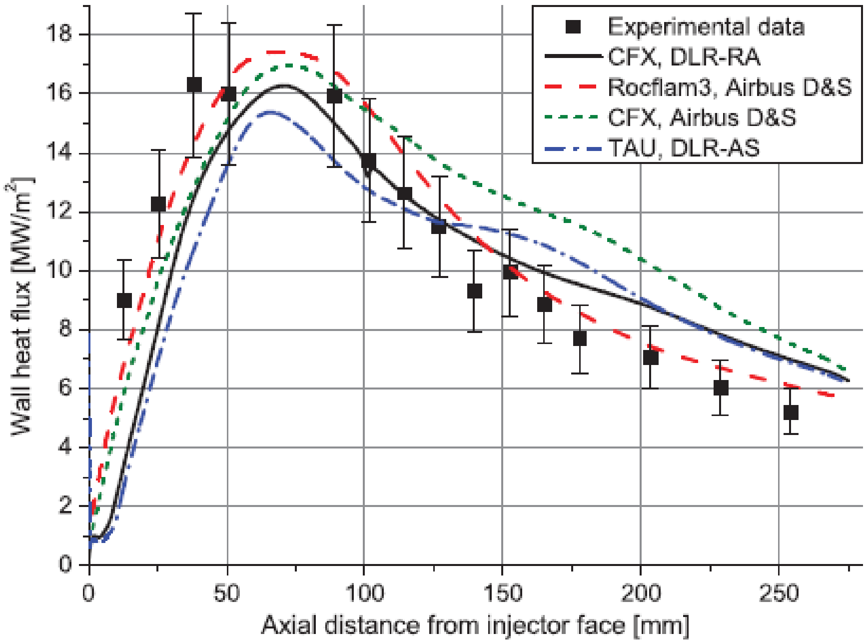

Figure 8: Comparison of study by Zhukov (2015) (black line) to that of previous studies. Extracted from Computational Fluid Dynamics Simulations of a GO2/GH2 Single Element Combustor by Zhukov (2015).

Note from Figure 8, the study by Zhukov (2015) investigated numerical solutions that compare within an error percentage of 15%. All the numerical solutions were developed by RANS equations with the Rocflam3 model achieving the highest accuracy when compared to the experimental results. The Rocflam3 numerical solution is an Airbus D&S in house CFD code. The experimental results are characterised by statistical error. The critical parameters such as pressure and temperature oscillate which will influence the determination of the wall heat flux. The wall heat flux measured value fluctuated as much as 8% in the study by Marshall et al. (2005) that presented a time profile of the wall heat flux.

Zhukov (2015) discusses that during hot fire tests the combustion chamber walls undergo erosion regardless whether the walls have been pretreated by polishing it. The erosion and oxidation are non - uniformly distributed after hot fire tests which are dependent on the local process conditions that exist at the walls. These two factors have a significant impact on the wall heat flux. The current study specified the wall roughness as 5µm which might not be accurate enough at an axial distance of 0.14m to minimise the percentage error of the numerical model at this point. By increasing the wall roughness specification by as much as 50% does not significantly change the numerical result. After the increase in wall roughness, the numerical solution changed by as much as 1.5%. The variation in wall roughness is insufficient to significantly influence the density variation at the near wall region. It is neither significant to influence the turbulence intensity at the near wall region. The change in wall roughness does influence the friction force along the wall and subsequently the azimuthal and axial velocity. This will consequently result in momentum loss. It is evident from the current study results that the wall roughness influence on density, velocity and momentum is not significant to alter the wall heat flux profile generated in the single element coaxial injector. Therefore the wall roughness influence on the measured wall heat flux is significantly less than the bulk fluid species mass flux influencing the temperature gradient, thermal conductivity and dynamic viscosity.

As discussed by Zhukov (2015), an additional contributing factor to the experimental uncertainties is that of the boundary conditions. It is highlighted that the injected gas temperature is lower than that of the temperature calculated with the assumption of preburner complete combustion. With the use of the NASA CEA program, McBride et al. (1996), Pal et al. (2006) for the calculation of the fuel-rich gas temperature, it was determined that the temperature is 1360K. While for the measured temperature of the fuel-rich gas the temperature of 811K was specified. Zhukov (2015) discusses that Pal et al. (2006) contributes the temperature discrepancy to heat loss through the preburner walls. Zhukov (2015) indicates that the heat loss is more likely due to fluid flow stratification by which the temperature achieved in the middle of the preburner is higher than that at the periphery. From the base case of the current study it is evident from the wall heat flux trend degree of accuracy that this model can be used with confidence.

Comparing Figure 6, Figure 7 and Figure 8 it is evident that the current study compares in most cases better to the experimental results than the previous studies discussed and outlined. The most comparable study is the Rocflam3 numerical model that compares closest to the current study numerical solution.

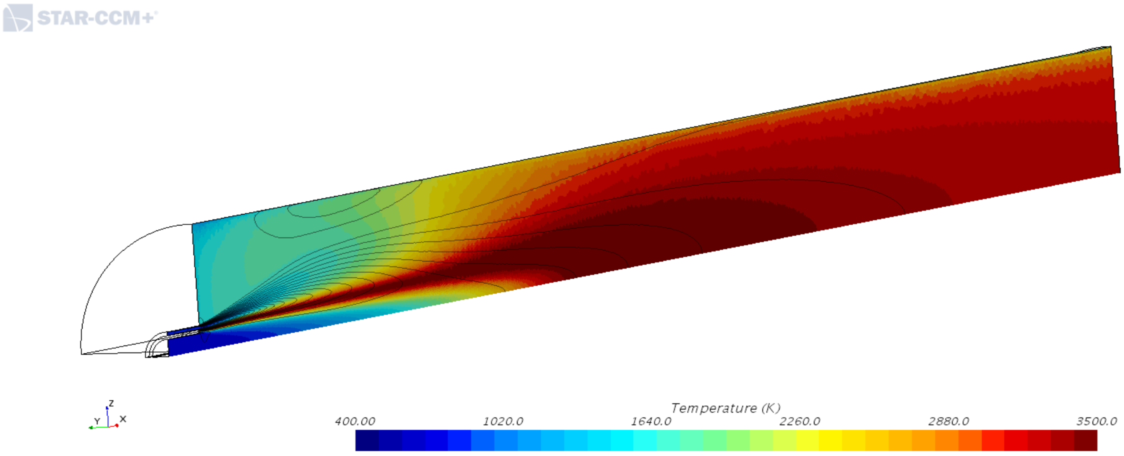

Figure 9: Base case study combustion chamber temperature distribution profile.

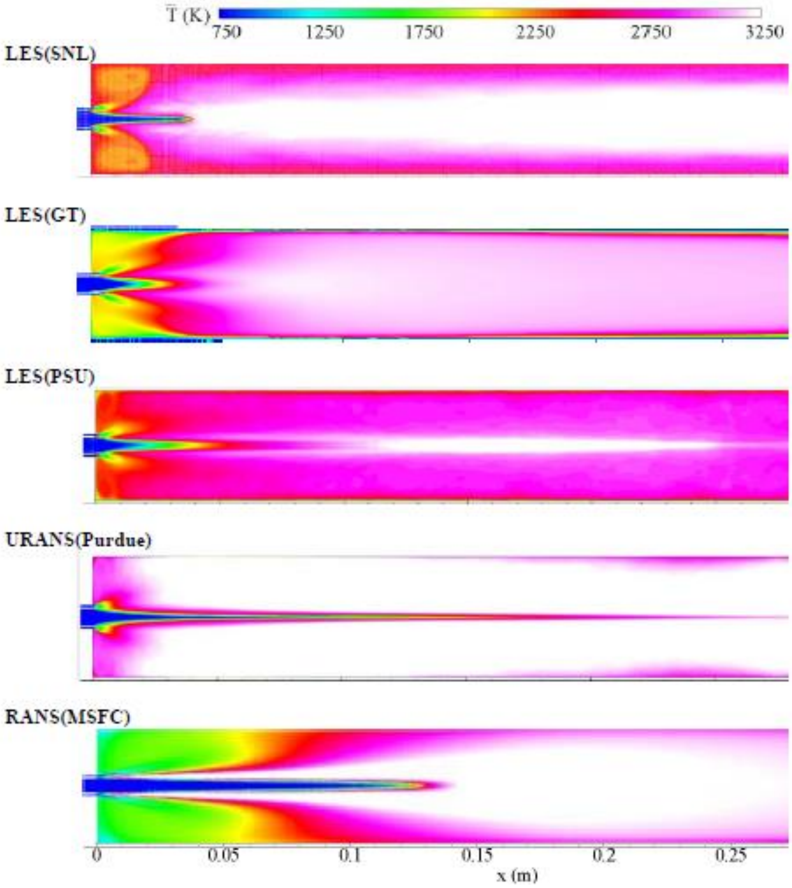

Figure 10: Previous studies temperature distribution profile of only the combustion chamber. Extracted from Validation of High - Fidelity CFD Simulations for Rocket Injector Design, Tucker et al. (2008).

Note from Figure 9 and Figure 10 the temperature distribution profile in the combustion chamber. From the current study results and the previous studies it is evident that there is a large temperature distribution profile difference between the different studies. This largely contributes to the difference in wall heat flux results. The head end region consist predominantly of recirculation zones and the current study temperature distribution, where x<0.06m, increases rapidly to approximately 3500K. The temperature distribution profile and core length compares well to the LES studies and the experimental results. The recirculation zones aids in turbulence mixing and promotes the chemical combustion which results in a temperature increase. Note that the 2D studies mainly achieve a temperature peak of 1200K. While along the axial distance of the current study, on the centreline where x < 0.06m, the temperature mainly resembles the oxidiser temperature while a temperature peak of 3500K is observed at x= 0.12m along the centreline. The RANS (MSFC) study centreline temperature peak is at approximately 3400K while the 2D studies LES (PSU) and URANS (Purdue) centreline temperature peak is at approximately 2000K. The current study temperature profile is comparable to the 3D numerical solutions while noting that the numerical RANS solutions have a predominant cold region along the centreline. The current study core length is approximately 0.06m long in the axial direction which compares well to the 3D numerical solutions. Downstream of the head end all the studies illustrates a gradual uniform increase in the temperature distribution profile. However when considering the study by Oefelein (LES SNL) there exist a significant boundary layer at a lower temperature of approximately 2300K. If the streamline profile of the velocity magnitude in the current study (refer to Figure 11) is considered, it can be compared to that of the study by Oefelein LES (SNL) and Huo (2011).

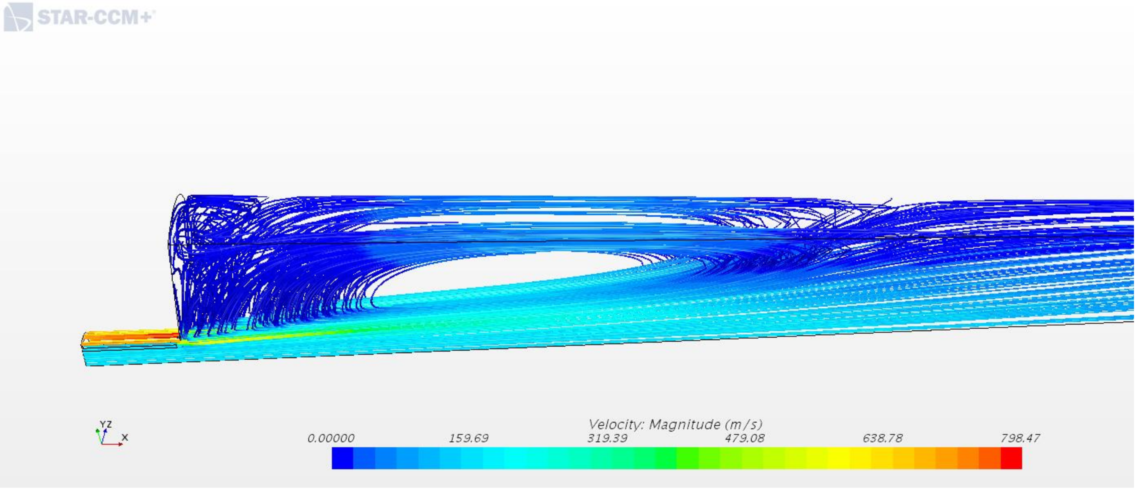

Figure 11: Base case streamline profile based on velocity magnitude.

The remaining studies have differences in streamline profile within the head end region (refer to Figure 11). The recirculation zones differ in size and number of noted recirculation zones in the head end region in the combustion chamber, which influences the numerical solution in terms of wall heat flux.

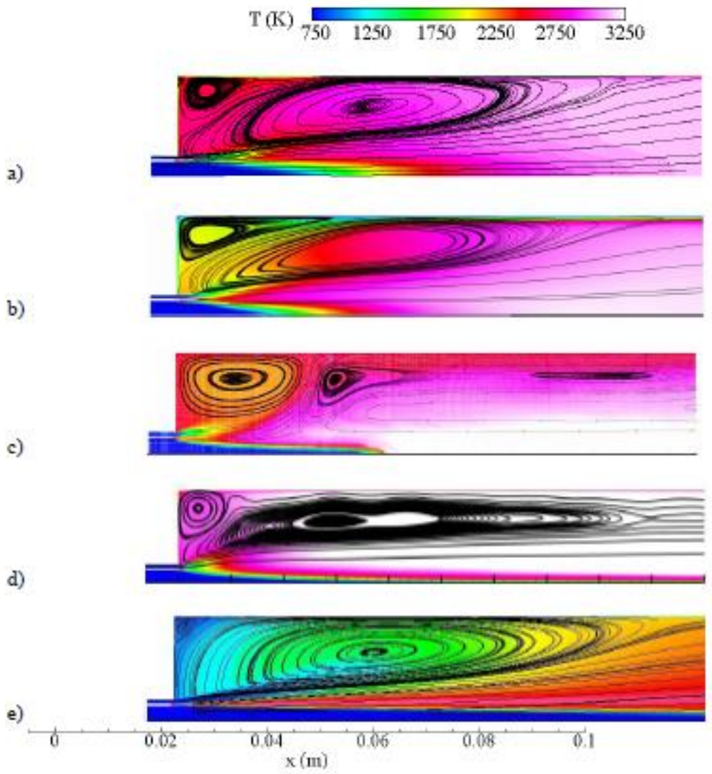

Figure 12: Streamline profile overlaid on temperature distribution of the different numerical solutions: a) Huo, 2011 b) Menon 3D LES c) Oefelein 3D LES d) Merkle 2D URANS e) Tucker 2D RANS. Extracted from Large – Edddy Simulation of Supercritical Fluid Flow and Combustion, Huo 2011.

The current study is comparable to the study by Menon 3D LES and Huo (2011) in which it clearly indicates two recirculation zones. There is one small recirculation zone where x < 0.03m followed by a larger and more intense recirculation zone where x < 0.1m. The study by Oefelein illustrates at least three recirculation zones. One large recirculation zone in the head end where x < 0.04m, followed by a smaller zone where, 0.05m < x < 0.07m and eventually a narrow recirculation zone where, 0.09m < x < 0.12m. The current study does portray similarities to the studies by Menon 3D LES and Huo (2011) in terms of streamline profile and temperature distribution profile but does not portray a similar boundary layer temperature of approximately 2300K as in the case of Oefelein 3D LES. This result justifies the comparison when referring to Figure 6 and Figure 8, of which the wall heat flux of the current study compares well to experimental results, the study by Huo (2011) and Menon 3D LES.

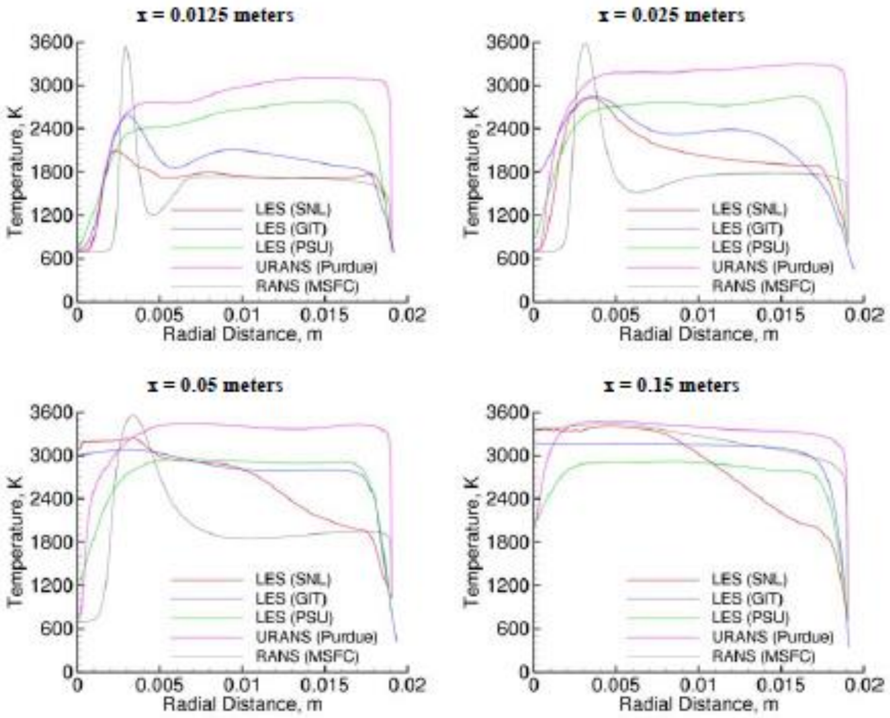

Figure 13: The radial temperature profile distribution at various axial lengths of 0.0125m, 0.025, 0.05m and 0.15m of the previous studies. Extracted from Validation of High - Fidelity CFD Simulations for Rocket Injector Design, Tucker et al. (2008)

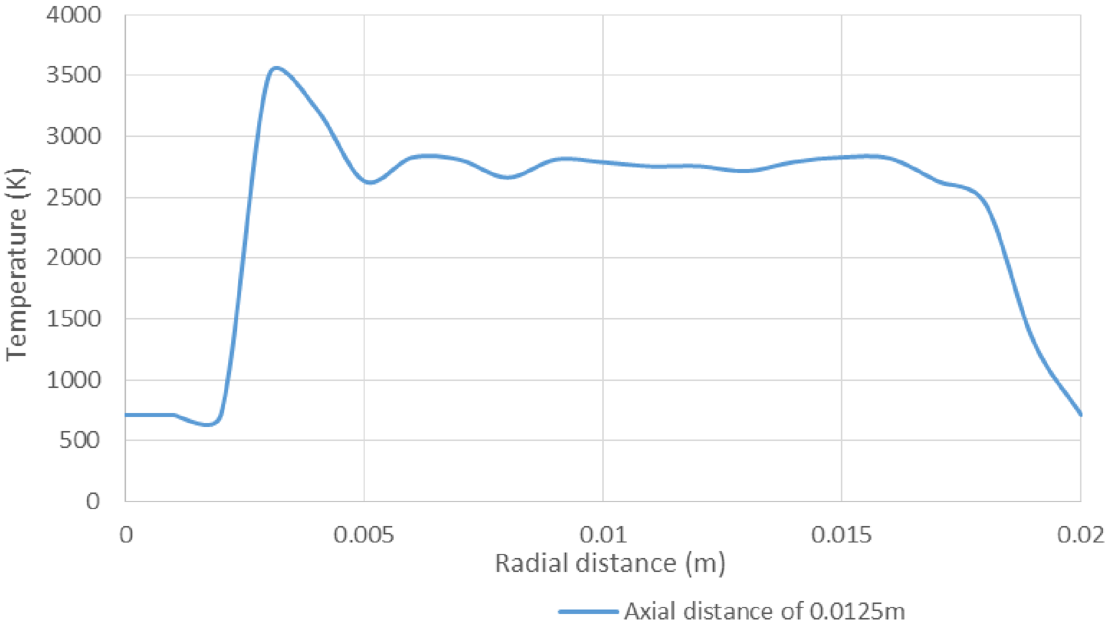

Figure 14: Radial temperature distribution profile of the base case at an axial distance of 0.0125m.

Figure 13 represents the radial temperature distribution profile of the previous studies as illustrated by Tucker (2008). Note that the RANS (MSFC) numerical solution is an excessive temperature peak within the head end region. The 3D LES numerical solution of LES (SNL) and LES (GIT) illustrate a lower, wider temperature peak which results in a lower flame temperature compared to the RANS (MSFC) study. Note that at axial distance of 0.0125m the RANS (MSFC) numerical solution achieves a peak temperature of approximately 3600K while the LES (SNL) numerical solution achieves a peak temperature of approximately 2100K with the LES (GIT) study reaching 2600K. There is a sudden decrease in temperature of the RANS (MSFC) numerical solution to approximately 1300K after which it increases and stabilises at 1700K. This is different to the LES (SNL) study that reduces and stabilises at approximately 1900K. The current study resembles a temperature profile of the RANS (MSFC) study where the peak temperature of approximately 3500K is achieved at x = 0.012m and a radial distance of < 0.05m. Note that the 2D numerical solutions have different trends compared to the 3D numerical solutions. The LES (PSU) and URANS (Purdue) does not illustrate a temperature peak but rather a rapid increase in temperature from the centreline, followed by a gradual increase into the recirculation zones. The temperature of these two studies abruptly decreases as the gas mixture moves closer to the prescribed wall temperature. The LES (PSU) and URANS (Purdue) numerical solutions also achieves higher temperatures in the recirculation zones than the other studies including the current study. Temperatures as high as approximately 2800K are achieved for the LES (PSU) study with the URANS (Purdue) study achieving approximately 3100K. The temperatures of all studies remain stable downstream in the combustion chamber as illustrated by an axial distance of x = 0.15m. The current study closely resembles a temperature profile of the LES (GIT) and Huo (2011) in a large region of the combustion chamber. The grid resolution difference of the studies can attribute to the noted differences in results. Noting that the current study applied extensive grid refinement in the flame zone and recirculation zones. The purpose of the current study’s grid resolution refinement in the mentioned areas were to accurately capture the effective gas mixture conductivity and the rapid heat transfer from the bulk gas fluid flow to the wall. Although the temperature profile differences between URANS (Purdue) and LES (SNL) are evident, the heat flux of these studies are in close agreement to the experiment. The current study has good agreement to the experimental wall heat flux results but illustrate differences in radial temperature profile to that of URANS (Purdue) and LES (SNL).

The wall heat flux profile and temperature profile across the flow domain attempts to give insight into the energy balance. Energy balance closure can be identified as the energy entering the combustion chamber as chemical energy. As the propellants move into the combustion chamber the chemical reactions convert this chemical energy into internal energy. The combustion chamber contents experiences energy loss at the non-adiabatic wall. The propellants finally exits the combustion chamber in the form of kinetic energy and thermal energy. The balance can be represented by Equation 5.141:

$$\dot{E}_{in} = \dot{E}_{loss} + \dot{E}_{out} \qquad 5.141$$

The current study illustrates energy balance closure by using the inlet oxidiser and fuel mass flow rates and their respective specific enthalpies. Using these parameters the energy flow into the combustion chamber is determined. The energy loss is determined by the heat flux profile. Using the temperature profile, the current study compares the mean temperature well to that of experimental measured values that indicates good closure with respect to the energy balance.

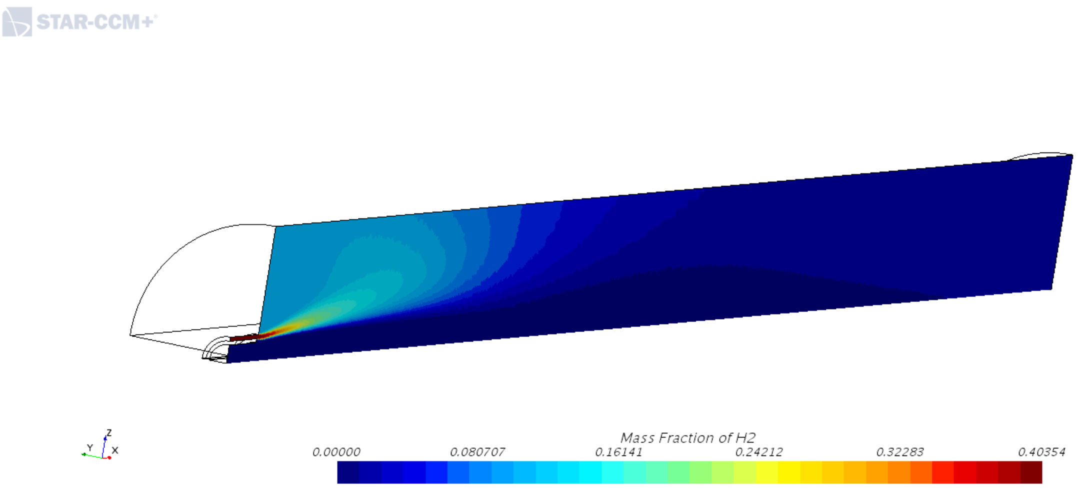

Figure 15: Base case hydrogen mass fraction distribution profile in the combustion chamber.

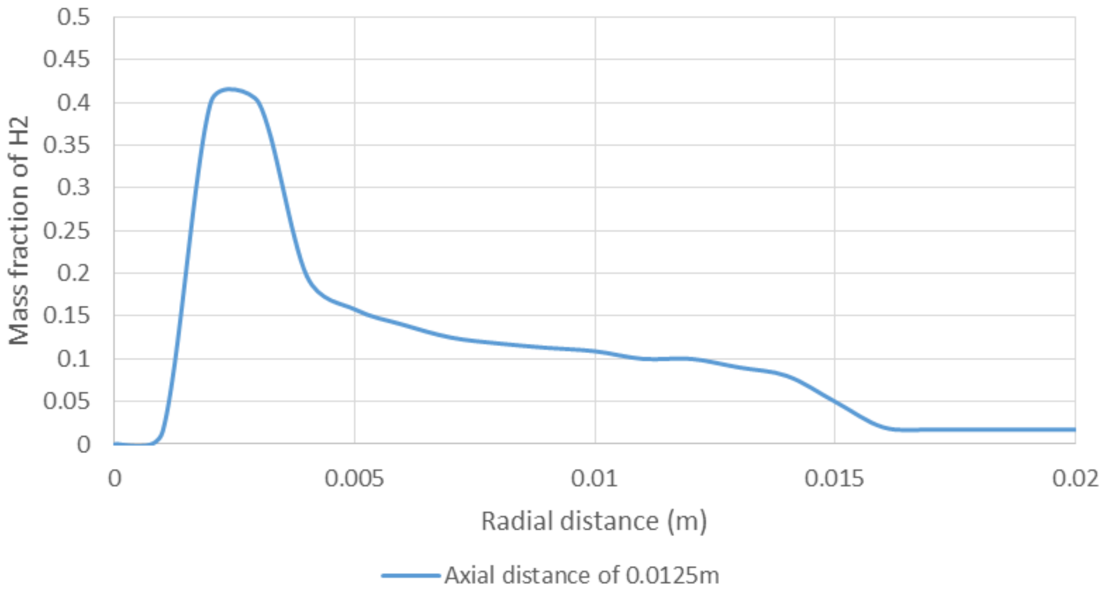

Figure 16: Base case hydrogen mass fraction distribution profile at an axial distance of 0.0125m

Due to the extent of reaction being a function of the gas mixture within the localised regions in the combustion chamber. It is clear that as the species concentration changes, the gas mixture conductivity changes and subsequently the combustion process. The hydrogen fuel component has a distinct difference in molecular response when considering the conductivity and diffusivity. This is largely related to the molecular size of Hydrogen. The hydrogen mass fraction distribution profile in the combustion chamber is represented by Figure 15.

While the hydrogen mass fraction distribution profile in the radial direction at an axial direction 0.0125m is displayed by Figure 16. From these figures it is evident that the recirculation zones have a significant influence on the hydrogen mass fraction in the head end region. This phenomenon will consequently influence the wall heat flux.

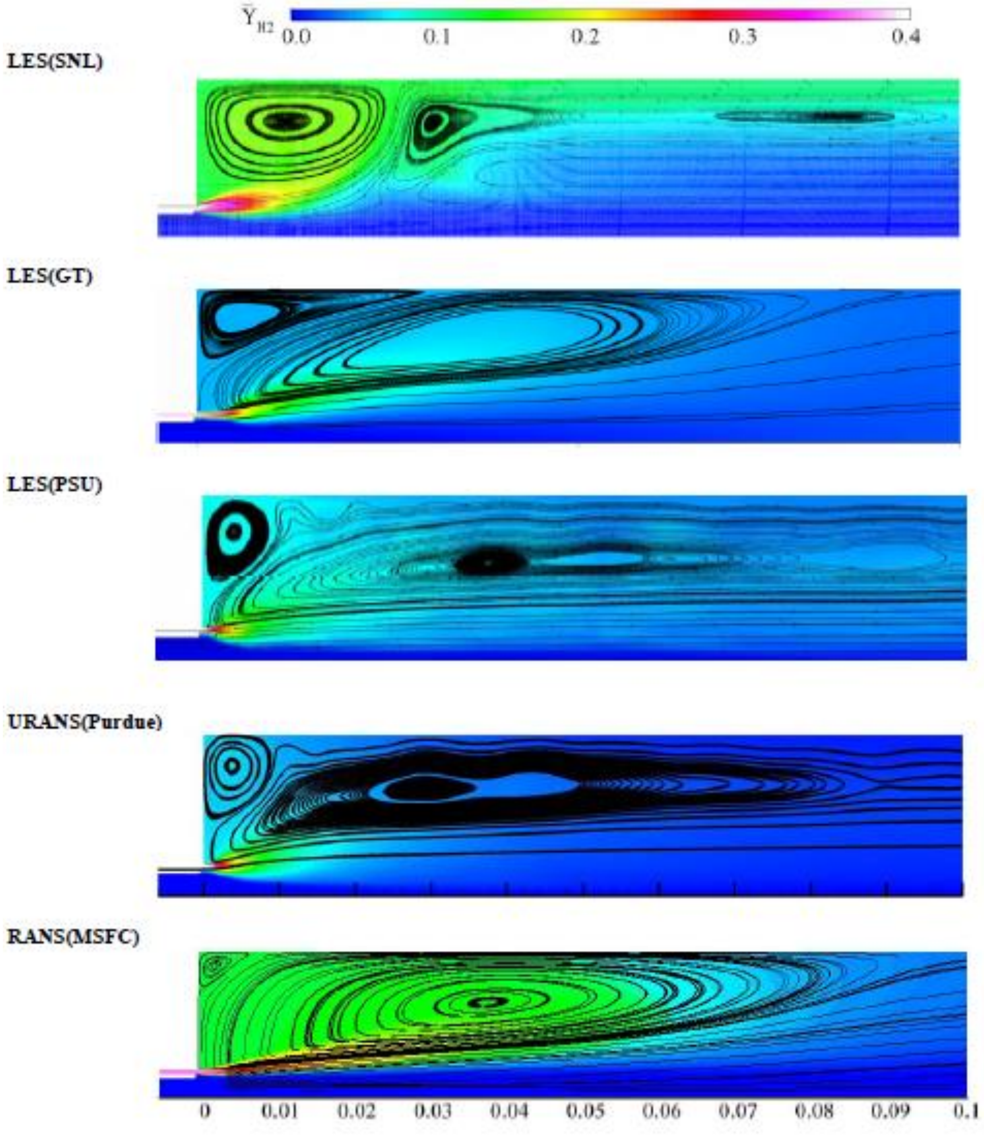

Figure 17: Streamline profile overlaid on hydrogen concentration distribution of the different numerical solutions: Extracted from Validation of High-Fidelity CFD Simulations for Rocket Injector Design Tucker et al. (2008).

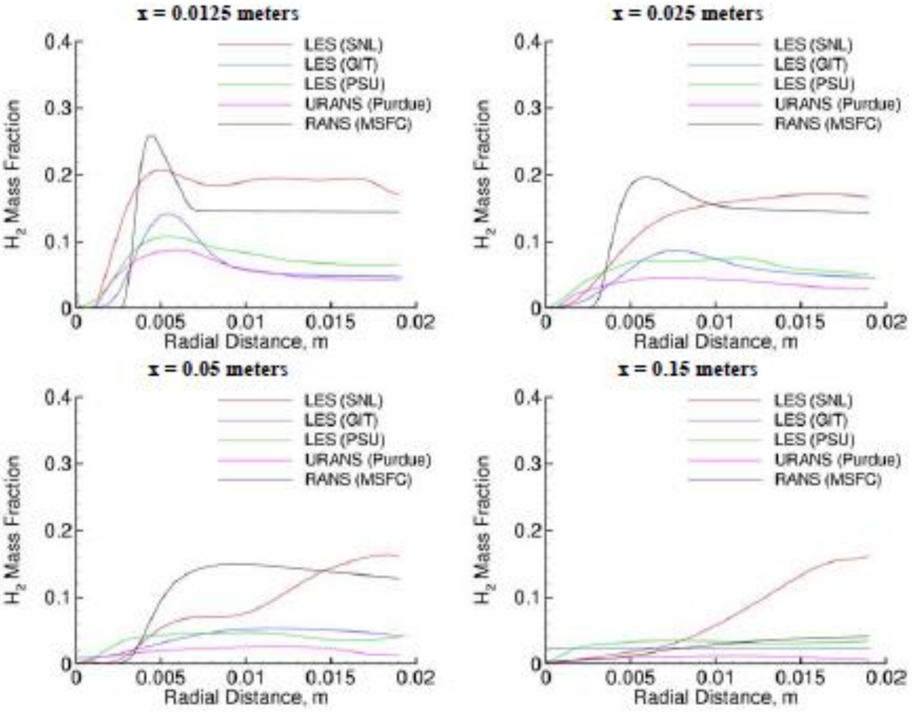

ure 9. Radial hydrogen mass fraction profiles at axial locations of 0.0125, 0.025, 0.05 and 0.15 m.

Figure 18: Radial hydrogen mass fraction distribution profile of previous studies. Extracted from Validation of High - Fidelity CFD Simulations for Rocket Injector Design, Tucker et al. (2008)

Note from the streamline trends depicted by Figure 17, that all the numerical solutions contain a localised recirculation zone in the corner of the combustion chamber in the head end region. The localised recirculation zones differ in size, form and location in all numerical solutions. There are however similarities that can be drawn from the numerical results. The current study illustrates a similar peak at a radial distance of 0.003m to that of RANS (MSFC). The peak of the current study is larger than the numerical solution of RANS (MSFC). The mentioned peak is followed by a gradual decrease in Hydrogen mass fraction until it reaches the wall and reverts to 0.017. The trend following the peak resembles the numerical solution by LES (GIT). The difference in the hydrogen spreading angle of the current study results in the mentioned differences in the hydrogen mass fraction peak in the head end region and the gradual decrease in the downstream region. The LES (SNL) numerical solution is distinctly different due to the three notable localised recirculation zones in the combustion chamber. In the LES (SNL) case the injected hydrogen fuel reacts in the flame region, concentrates in the large localised recirculation zone in the corner of the combustion chamber, after which it moves towards the flat elongated recirculation zone closest to the wall. The resultant hydrogen along the wall will promote combustion in this near wall region until the gas mixture exits the chamber. This is not a desirable effect due to the risk associated with the gas mixture after burn and possible concentration increase downstream of the combustion chamber. It further illustrates that a large volume of hydrogen leaves the combustion chamber which results in a lower predicted bulk gas temperature. The RANS (MSFC) numerical solution illustrates a similar trend as the current study where most of the injected hydrogen is concentrated in the head end region. The concentrated hydrogen region has a larger volume and unlike the LES (SNL) does not illustrate a hydrogen mass fraction concentration further downstream along the wall.

The mentioned observations are further illustrated by the radial distribution profile in Figure18. The current study resembles the RANS (MSFC) trend in the head end region while the LES (GIT) trend is comparable to the current study in the downstream region. This is evident that the hydrogen concentration distribution in the combustion fluid flow domain is not solely affected by only one specie, but rather the fluid flow mixture and flow dynamics. The peak in hydrogen concentration is consistent with the noted peak in temperature in the head end region in the radially outboard side of the flame zone. As the flow however progresses downstream in the combustion chamber the turbulence intensity decreases with a low bulk velocity at about 100m/s. This indicates that the resultant turbulent gas mixture conductivity is minimal. The current study y^+ - values are less than one, at the combustion chamber wall, therefore at the near wall region where a cell is located in the buffer region of the turbulent boundary layer, the turbulent viscosity will be negligibly low compared to the molecular viscosity at the first grid point in the near wall region. The temperature gradient of the LES (SNL) study and the current study are comparable and subsequently is the wall heat flux profile. Although the current study does not resemble the hydrogen concentration along the combustion chamber wall as that of the LES (SNL) study. The current study and the LES

(GIT) study have similar hydrogen concentration profiles at the wall but with different temperature gradients. This can be largely attributed to the difference in grid resolution and as a result indicating the significant influence of the turbulent thermal diffusivity in the heat flux. From the

The oxygen concentration profile within the combustion chamber is examined by comparing the current study to that of the previous studies. A benchmark oxygen concentration of 50% was used in order to achieve a relative comparison in terms of the core length. The study by Wang et al. (2011) uses the ratio of residual oxygen mass flow rate as the benchmark value of 50% as an indication of complete combustion. Note that the LES (SNL) and LES (GIT) studies produces a significantly shorter core length compared to the other studies. These two mentioned studies are full 3D LES simulations which are significantly different to the 2D axisymmetric simulations that include LES (PSU) and URANS (MSFC). The URANS (Purdue) study produces the longest core length with oxygen exiting through the nozzle.

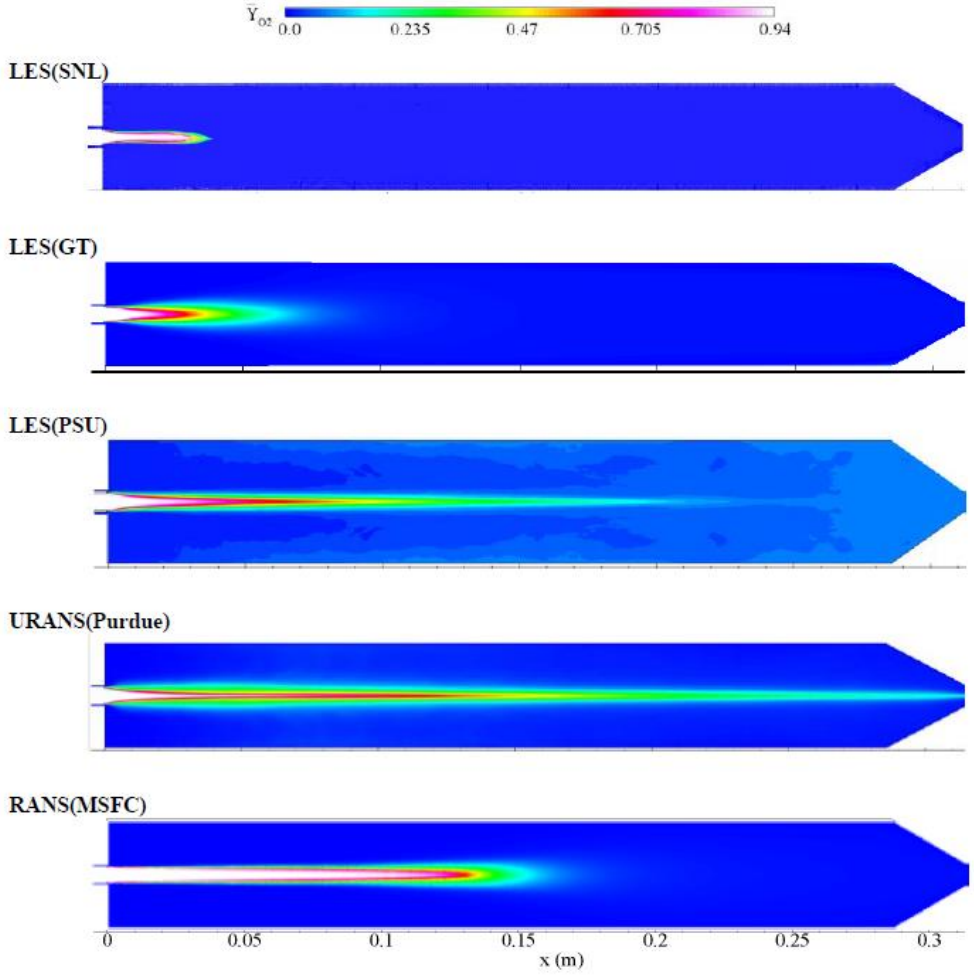

Figure 11. Time-averaged distributions of oxygen concentration.

Figure 19: Oxygen concentration distribution profile. Extracted from Validation of High - Fidelity CFD Simulations for Rocket Injector Design, Tucker et al. (2008)

The current study oxygen core length does not resemble the simulation study results of LES (SNL) and LES (GIT). The core length of the current study at which complete combustion is achieved is calculated as 0.1m for the base case. This base case oxygen concentration distribution profile will be used as benchmark in the injector structure improvement design variations.

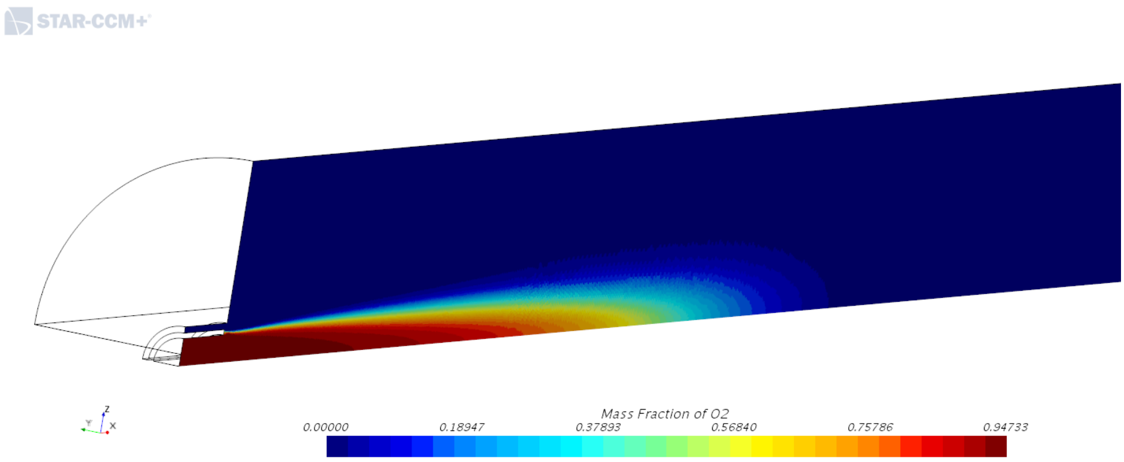

Figure 20: Base case oxygen concentration distribution profile.

All the studies presented in this section predict the general heat flux trend as compared to the experimental results. The product consisting of a series of chemical combustion interactions and species variations. Initially the oxidizer and fuel are injected into the combustion chamber after which mixing is achieved through the shear layers developed between the two streams. The flame originates in the head end region and develops into the combustion chamber as the propellants break up and complete mixing is achieved. In the flame region, heat is generated and the combustion products are routed to the combustion chamber wall via turbulent eddy currents. The combination of all turbulent eddy currents develop the whole fluid motion which is responsible for energy transfer and promote specie mixing and chemical reaction. At the wall region heat is transferred from the hot gas to the chamber wall. The species, temperature and velocity non-uniformity in the axial direction produces the various distributions used for model comparison.

The mass balance closure is illustrated firstly by the simulation residuals for all species that achieved steady state at a value less than 0.01. This was achieved after approximately 9500 iterations. To illustrate that mass convergence has been achieved, tracking plots have been included below. The difference between the total mas flow rate measured at the inlet and outlet can be contributed to the numerical model initiation parameters. As part of the initiation parameters the combustion chamber is filled with nitrogen to attempt to stabilise the injected propellants. It was found that when the combustion chamber is filled with air the numerical model is unstable and does not converge. The plot below illustrates that the inlet and outlet total mass flow rate have achieved steady state and that mass balance closure has been achieved.

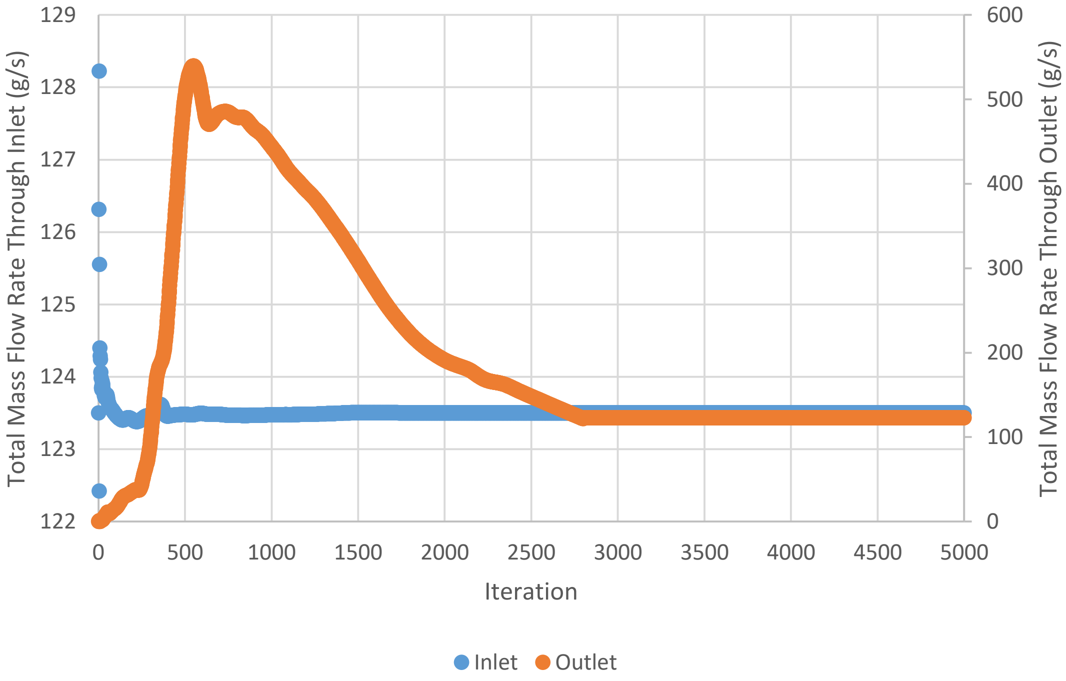

Figure 21: Total mass flow rate through the inlet and outlet respectively measured in g/s.

The modelling of the combustion process poses challenges that include grid resolution, turbulence modelling, chemical kinetic modelling and wall boundary layer modelling. All of which influence the accuracy of the predicted heat flux. The current study produces a high degree of accuracy when compared to the experimental results. To further improve the accuracy of the heat flux measurements in the combustion chamber further investigation into minimising the error of measurement and experimental error can be applied. Images and chemical specie images in the head end region and further downstream in the combustion chamber can be used to verify the flame structure to further assess the accuracy of the numerical studies.

5.2 Shear Coaxial Injector with Recess Length

This section investigates the effect on the shear coaxial injector performance when a recess length on the oxidiser post is applied. For this case the momentum ratio (m_r) and recess length was varied and the effect of the change compared and assessed with the base case. The injector performance was assessed using the combustion length (L_{com}) and the combustion efficiency (η_{C^*}). Further comparison is applied when using π_1 and π_4 as dimensionless parameters. The momentum ratio was simulated and assessed at a recess length of 30% and 60% of the oxidiser post inner diameter (5.26mm). Each of the recess length cases were then further simulated at a fuel:oxidiser momentum ratio of 0.1, 0.2, 0.4 and 0.5 respectively. The base case is designed with a recess length of 5.7% of the oxidiser post inner diameter, a momentum ratio of 0.37, combustion length of 0.11m and combustion efficiency of 96.5%. Furthermore for the base case $\pi_1 = 19.01$ and $\pi_4 = 0.06$ indicating the influence that the recess length has on the extent of combustion. For the current study, the oxidiser inner diameter is not varied and therefore π_1 will be influenced based on the aforementioned parameter adjustments.

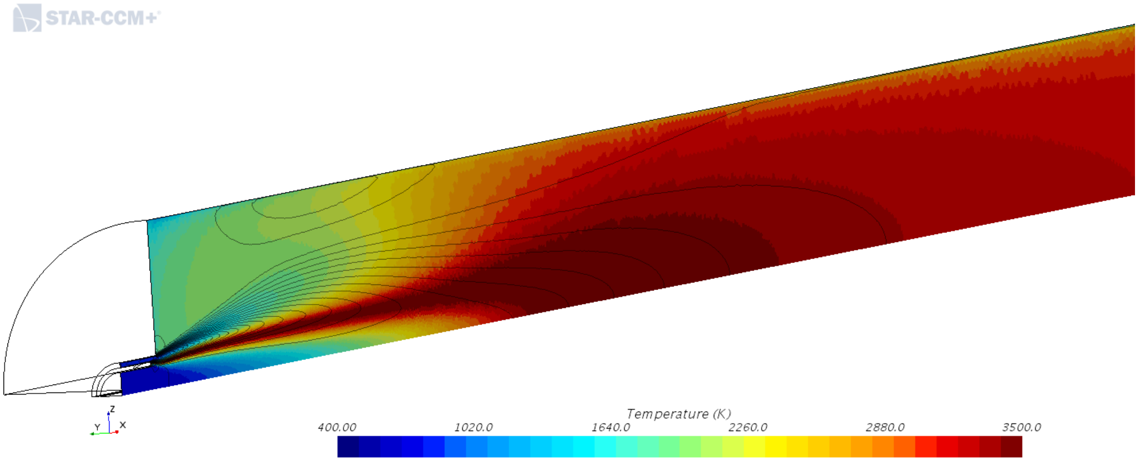

Figure 22: Temperature distribution profile of the 30% recess length case.

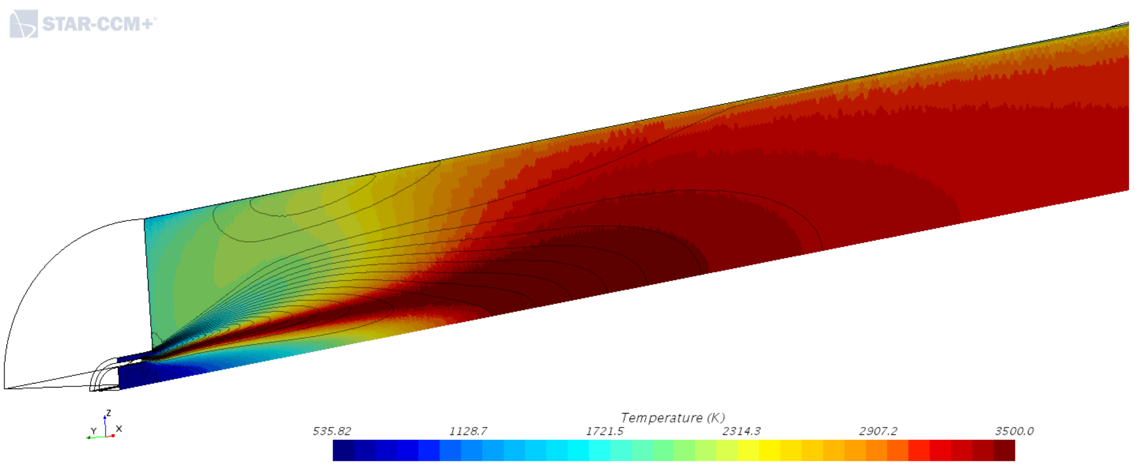

Figure 23: Temperature distribution profile of the 60% recess length case.

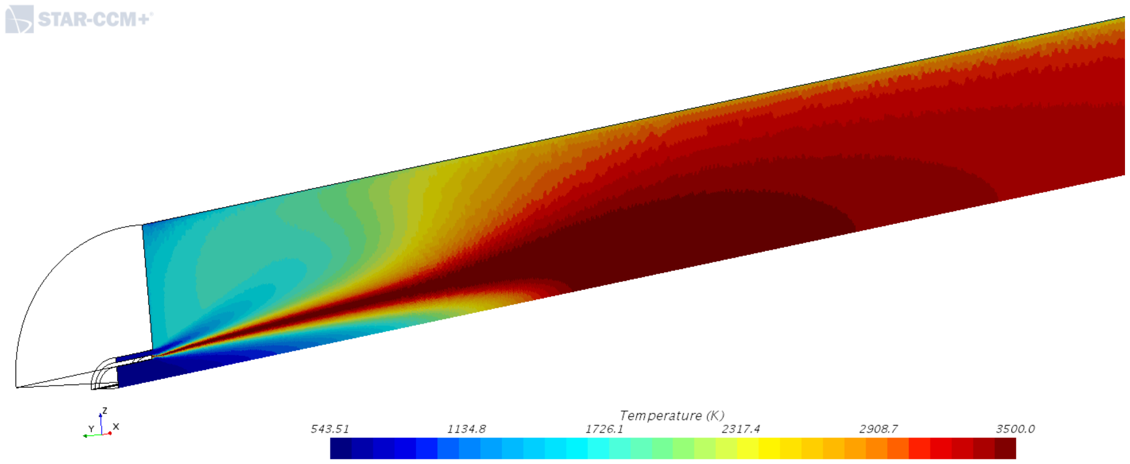

Figure 24: Temperature distribution profile of the base case.

All the recess length simulation cases have different flame pattern and length compared to the base case. Figure 22 to Figure 24 represents the temperature profile illustrating the difference in the recess length cases compared to the base case. This representation has not taken into account the momentum ratio change. There is a minimal difference of 0.012m in the combustion length between the recess length cases of 30% and 60%. The improvement compared to the base case was that the combustion length was shortened by 0.025m resulting in a 21.7% improvement. The difference in combustion length can be attributed to the increase in shear layer intensity by the induced impingement of the oxidiser into the fuel. This would result in an increased contact area for combustion. Since in the GO_2/GH_2 injector combustion occurs at the shear layer where the contact surface is between the fuel and oxidiser. The recess length changes the total heat release that comprises of reaction heat and combustion reaction associated with the GO_2/GH_2 coaxial injector. The heat release influences the combustion chamber wall pressure profile. During the simulation cases it was found that the pressure drop increased for the recess length cases compared to the base case.

The simulation tests were repeated at a recess length of 30% and 60% to include the momentum ratio change. The results of the 8 tests cases are shown in Table 3. It is clear from the comparison of the π terms that the combustion efficiency compares well when comparing these terms from case to case.

Table 4: Recess length simulation case results at different momentum ratios.

Test case number	Momentum ratio, m_r	Recess length (%)	Combustion length, L_{com} (m)	π_1	π_4	Combustion efficiency, η_{C^*} (%)
1	0.1	30	0.18	34.2	0.3	99.9
2	0.2	30	0.12	22.8	0.3	99.9
3	0.4	30	0.09	17.1	0.3	95.6
4	0.5	30	0.08	15.2	0.3	89.7
5	0.1	60	0.16	30.4	0.6	99.9
6	0.2	60	0.11	20.9	0.6	99.9
7	0.4	60	0.09	17.1	0.6	93.5
8	0.5	60	0.08	15.2	0.6	89.4

Note from test case 1 and 2 that the efficiency is at 99% mainly due to the low momentum ratio. Excess oxidiser is available in these cases for complete combustion to occur. These test cases produce a low characteristic flow velocity which is not practically suitable. The results of these cases produce a slightly lower combustion chamber wall temperature and results in a higher temperature difference at the wall. The increased temperature differential results in a slightly higher wall heat flux. This is illustrated by Figure 25. Furthermore the recess length test cases result in a slightly higher temperature in the injector head end region.

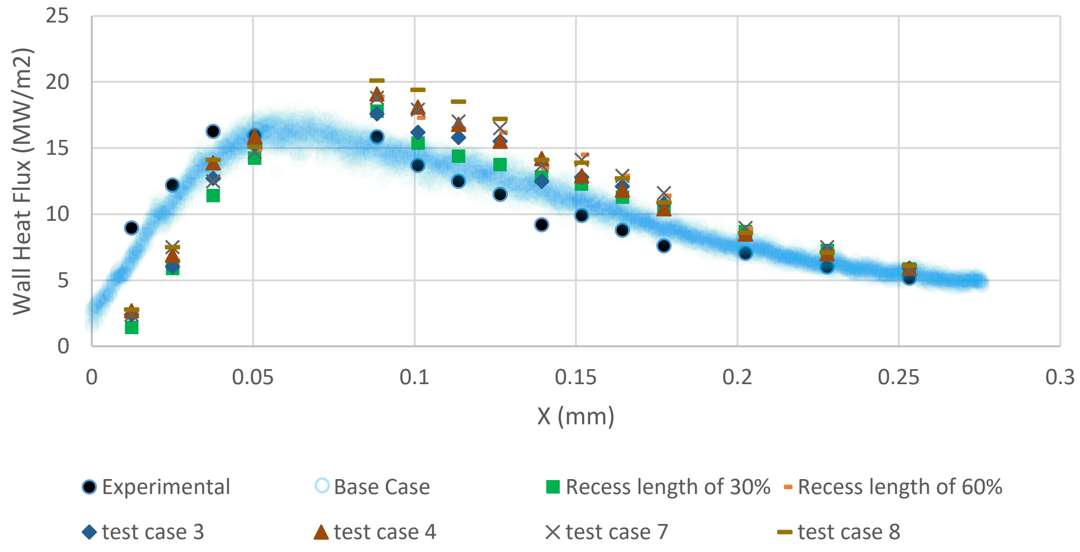

Figure 25: Wall heat flux of the different recess length test cases. Experimental results extracted from Computational Fluid Dynamics Simulations of a GO2/GH2 Single Element Combustor by Zhukov (2015).

It was further noticed that as the recess length increases while keeping the momentum ratio constant at 0.37, there is a slight velocity magnitude decrease. This finding is similar to the study by Ping et al. (2013). From Table 2 it is noted that the combustion efficiency decreases as the momentum ratio exceeds 0.4 which can be attributed to an excess fuel case. The minimal difference in wall temperature of the 30% and 60% test case illustrates that the heat transfer influence on combustion efficiency is minimum. The recess length case enhances the development of large scale vortices at the oxidiser post which will enhance mixing of H_2 and O_2. The intensified shear layer induces higher turbulence fluctuations which will increase the contact area between the fuel and oxidiser that will further assist reaction kinetics and improve injector performance. For the current study at high temperature and pressure the reaction kinetics are fast. At the high Re number the diffusion and convection rates mainly influence flow. The recess length cases does improve the injector mixing performance followed by an increased heat of combustion. The current study illustrates that the propellants ignite upon contact and sustains the combustion process given the availability of fuel and oxidiser. The combustion products at the shear layer impede the combustion process to a certain degree. This is due to restriction placed on the hydrogen molecules via the combustion products to contact oxygen for the reaction to take place. Therefore the recess length and momentum ratio should increase the contact surface are between the propellants in order to overcome this restriction. This will improve combustion performance and improve efficiency.

The best case considered the coaxial injector is to maintain the base case momentum ratio and apply the 30% recess length (refer to Appendix A for flow distribution profiles). Further research is required to investigate maximum injector performance in terms of efficiency and combustion length, at a specified recess length and momentum ratio.

5.3 Swirl Coaxial Injector with Recess Length

The following section investigates the injector performance influenced by applying swirl – coaxial flow. Swirl – coaxial flow injectors are widely used in liquid rocket engines as outlined by GuoBiao, et al. (2016). This is done to initiate atomisation of liquid droplets in gas-liquid and liquid-liquid injector applications. The current study utilises swirl to investigate the fluid dynamic response in the GO_2/GH_2 injector. The flame structure and combustion chamber temperature distribution profile of the swirl case will be investigated in order to assess its applicability in practical injectors. The high heat release in the injector head end region and near wall region are investigated as well.

The swirl injector performance was assessed using the combustion length (L_{com}) and the combustion efficiency (η_{C^*}) similarly to that of recess length test case. The momentum ratio was simulated at the base case condition of 0.37 and assessed in terms of injector combustion length and combustion efficiency.

The flow field is analysed to identify the differences of the swirl case compared to the base case. The swirl simulation test case is setup with the same thermodynamic properties as that of the base case. Together with the thermodynamic base case settings a Swirl number of 0.85 was selected as test case calculated by Equation 2.128.

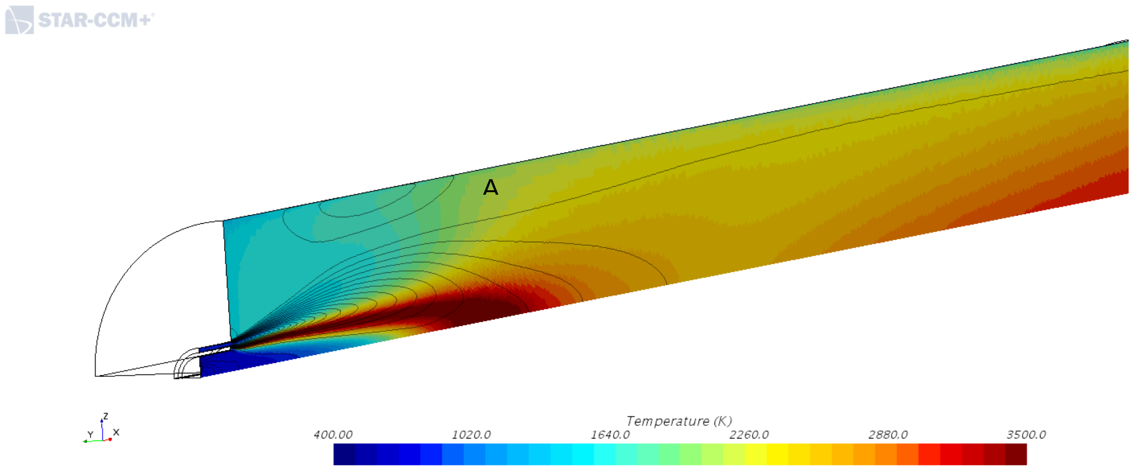

Figure 26: Swirl test case streamline profile based on temperature distribution profile.

From Figure 26, illustrating the stream line profile based on the temperature distribution profile, it is evident that an outer recirculation zone exists between the propellant injection and the combustion chamber wall. The swirl test case compared to the base case has a higher temperature in the head end region that is approximately 300K higher. This is attributed to the combustion products being routed into the outer recirculation zone that results in a higher temperature in the head end region and injector faceplate. This area is represented by the letter, A, in Figure 26. The outer recirculation zone is promoted by the propellants being entrained into this localised high temperature area in the combustion chamber.

Since the base case is designed with a recess length of 5.7% of the oxidiser post inner diameter, this key design parameter strongly influences the flame stability to retain hot reaction products while continuously routing reactants from the source upstream of the injector. The swirl test case produced a combustion length of 0.065m with $\pi_1 = 12.4$ and$\pi_4 = 0.06$. This is a 40.9% improvement in combustion length when compared to the base case. Assessing the oxygen mass fraction (Figure 28) and temperature distribution profile, it is evident that the oxidiser swirl effect enhances the mixing effect resulting in a shorter combustion length compared to the base case. Therefore the swirl effect changes the flame pattern, combustion efficiency and consequently the heat release.

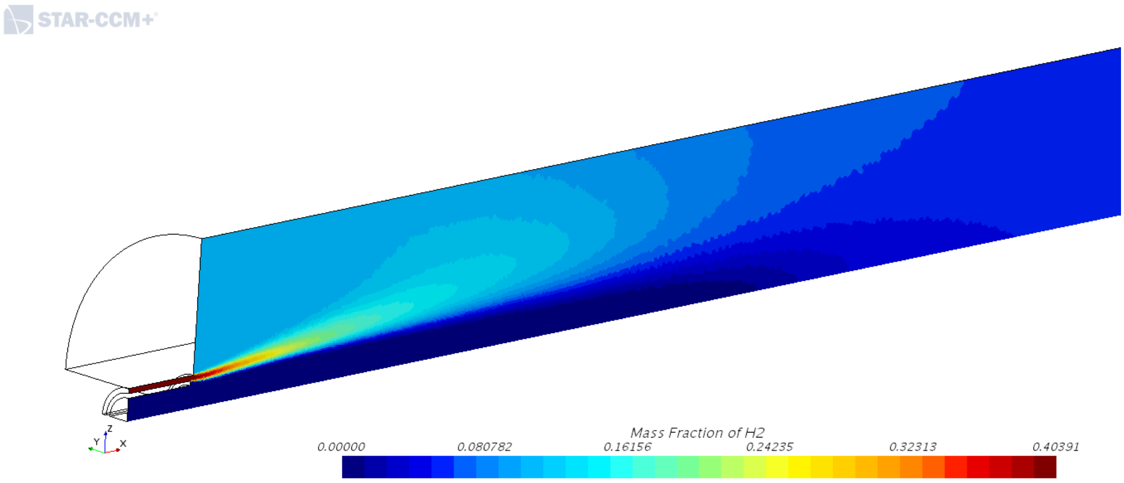

Figure 27: Hydrogen concentration distribution profile of the swirl test case.

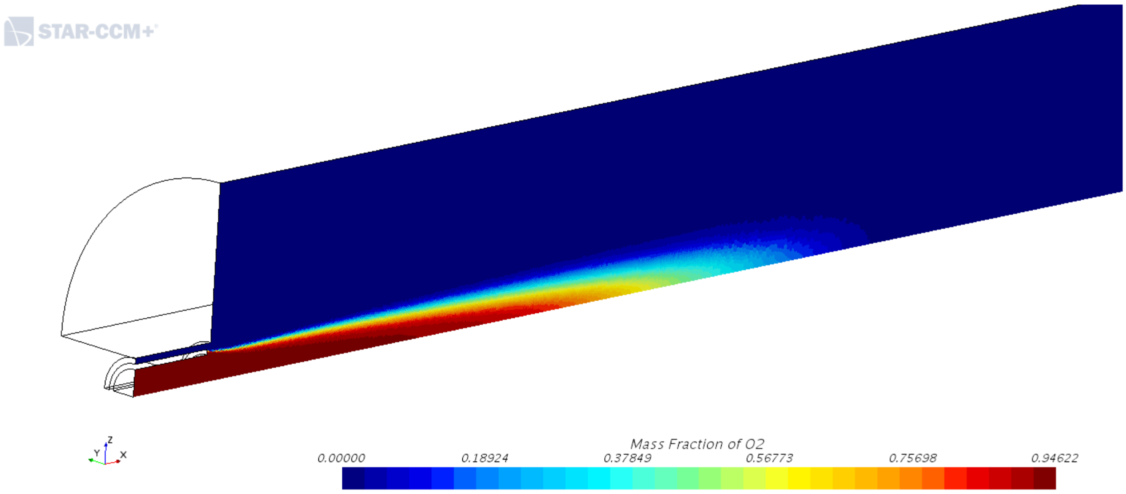

Figure 28: Oxygen concentration distribution profile of the swirl test case.

As noted in the temperature distribution profile, the hydrogen concentration profile (represented by Figure 27) illustrates the outer recirculation zone. The higher hydrogen concentration in the combustion chamber outer recirculation zone further promotes the higher temperature noted in the head end region.

The swirl test case does improve the combustion efficiency when compared to the base case. The combustion efficiency achieved of the swirl case is 98.2%, which is 1.7% higher than the base case test. This is attributed to an increase in mixing that results in an increase in the contact surface area between the propellants. The swirl test case produces a higher heat release in the head end region and consequently the injector faceplate (refer to Appendix B for flow distribution profiles). To apply this design practically it will require increase temperature protection of the combustion chamber to prevent any mechanism of failure related to high temperature.

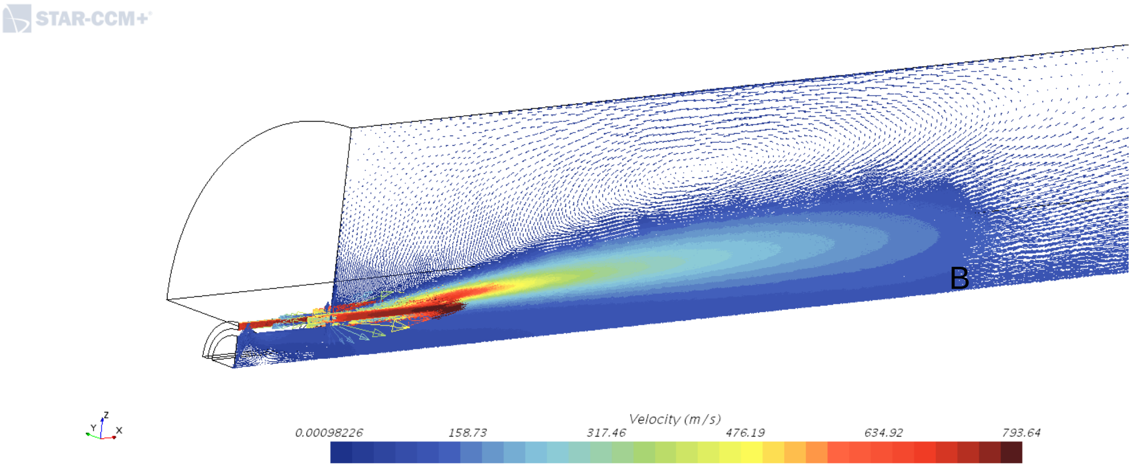

Figure 29: Velocity vector profile of the swirl test case while maintaining the base case momentum ratio.

From the velocity profile illustrated by Figure 29, as the oxidiser flows downstream there is significant expansion with significant decrease in the radial velocity. From the velocity profile there is an inner recirculation zone, indicated by the letter B, where high temperature combustion products are circled back to the flame. This is related to the temperature profile, where it is illustrated that the swirl case influences the flame pattern, combustion and heat release. The oxidiser swirl has the biggest influence on the inner recirculation zone, combustion length and core radial extension.

6. Conclusions and Recommendations for Further Investigation

This project has focussed on the theoretical and numerical modelling of GO_2/GH_2 single element coaxial rocket injector flow and combustion dynamics. The numerical results obtained were discussed throughout the various numerical solutions achieved at different design parameter optimisation conditions. The base case numerical solution of the current study produced a high degree of accuracy when compared to the experimental results. The base case study achieved a confidence interval of 95% that produced a percentage error less than 5%. It is recommended to further improve the accuracy of the heat flux measurements in the combustion chamber by minimising the error of measurement and experimental errors that are applicable. Images and chemical specie images in the head end region and further downstream in the combustion chamber can be used to verify the flame structure to further assess the accuracy of the numerical studies.

The design optimisation case of an applied recess length of the oxidiser post produced 21.7% improvement of combustion length compared to the base case. The results of these cases produced a slightly lower combustion chamber wall temperature and results in a higher temperature difference at the wall. The increased temperature differential results in a slightly higher wall heat flux. It is recommended that for this type of design optimisation, the optimum combination is to maintain the base case momentum ratio and apply the 30% recess length. Further research is required to investigate maximum injector performance in terms of efficiency and combustion length, at a specified recess length and momentum ratio.

The design optimisation case of a swirl flow case for the oxidiser produced a 98.2% combustion efficiency, which is a 1.7% improvement when compared to the base case. This is mainly attributed to an increase in mixing that results in an increase in the contact surface area between the propellants. The swirl test case produced a higher heat release in the head end region and consequently the injector faceplate. To apply this design practically it is recommended to increase the temperature protection of the combustion chamber to prevent any mechanism of failure related to high temperature which is associated with this test case.

The current study only investigated and evaluated the single element injector. It is recommended that multiple side-by-side injectors be studied in future research. It is recommended that future research investigate the effect of the combustion chamber length, throat nozzle diameter and oxidiser swirl injection that includes oxidiser post recess length to maximise the injector performance in terms of combustion efficiency and combustion length.

References

Anderson, J. (1995). *Computational Fluid Dynamics The Basics With Applications.* McGraw-Hill Education.

ASME V&V 20. (2009). *Standard for Verification and Validation in Computational Fluid Dynamics and Heat Transfer.* American Society of Mechanical Engineers, ISBN 9780791832097.

Balaras E., Benocci C., Piomelli U. (1996). Two-Layer Approximate Boundary Conditions for Large-Eddy Simulations. *AIAA Journal*.

Bardina, J., Ferziger, J., & W, R. (2003). Improved Subgrid Scale Models for Large Eddy Simulation. *Journal of Propulsion and Power*.

Berque J., Sion M. (1999). *Tricoaxial Injector Technology Development.* AIAA 1999-2492.

Cabot, W. (1995). Large-Eddy Simulations with Wall Models.

Calhoon D, Ito J, Kors D. (1973). *Investigation of Gaseous Propellant Combustion and Associated Injector-Chamber Design Guidelines.* Aerojet Liquid Rocket Company, NASA CR-121234.

Calhoon W., Menon S. (1996). Subgrid Modeling for Reacting Large Eddy Simulations. *Aerospace Sciences Meeting and Exhibit*.

Cengel, Y. (2006). *Heat and Mass Transfer A Practical Approach.* New York.

CFD-Online. (2019). Retrieved from www.cfd-online.com.

Chapman, D. (1979). Computational Aerodynamics Development and Outlook/Dryden Lecture in Research for 1979. *American Institute of Aeronautics and Astronautics, Aerospace Sciences Meeting*.

Cheng G.C, Farmer R.C. (2005). *Numerical simulation of spray combustion flows with a linearised real-fluid model.*

Chuech S.G.K., Przekwas A.J., Wang C.Y.,. (2004). Numerical Modeling for Atomisation of Coaxial Liquid/Gas Jets. *Journal of Marine Science and Technology, Vol. 12, No. 4*, 290-299.

Clayton R., Rupe J.H., Gerbracht F.G.,. (1967). *An Experimental Correlation of the Nonreactive Properties of Injection Schemes and Combustion Effects in a Liquid-Propellant Rocket Engine.*

Coleman H., Roache P. (2008). *An Overview of ASME V&V 20: Standard for.*

Conley, C. (2006). *High-Pressure GH2/GO2 Combustion Dynamics.* University of Florida.

Dahm W.J.A., Dibble R.,. (1998). *Coflowing Turbulent Jet Diffusion Flame Blowout.*

Dahm W.J.A., Mayman A.G.,. (1990). *Blowout Limits of Turbulent Jet Diffusion Flames for Arbitrary Source Conditions.*

Dimotakis, P. (1986). *Two-Dimensional Shear-Layer Entrainment.*

Driest, E. V. (1956). On Turbulent Flow near a Wall. *Journal of the Aeronautical Sciences*.

Durbin, P. (1996). *On the k-e Stagnation Point Anomaly.* International Journal of Heat and Fluid Flow.

Erlebacher, G. (1992). *Toward The Large - Eddy Simulation Of Compressible Turbulent Flows.*

Farhangi S. , Yu T., Rojas L., Sprouse K., McKinnon J.,. (1999). Gas-Gas Injector Technology For Full Flow Stage Combustion Cycle Application. *AIAA*.

Favre, A. (1965). Equations of Compressible Turbulent Gases.

Fujita M. , Fukushima Y. . (1996). *Improvement of LE-5A and LE-7 Engine.* AIAA Paper 1996-2847, 1996.

Germano M. (1992). Turbulence - the Filtering Approach. *Journal of Fluid Mechanics*.

Germano M., Piomelli U., Moin P., Cabot W. (1991). A Dynamic Subgrid - Scale Eddy Viscosity Model.

Ghorbanian K., Ashjee M., Soltani M.R., Mesbahi M.H., Morad M.R. (2004). *Experimental study of the spray of a liquid-liquid coaxial swirl injector for different injection pressures.*

Ghorbanian K., Soltani M.R. (2005). *Spray Characteristics of a Liqui-Liquid Coaxial Swirl Atomiser at Different Mass Flux Ratios.*

Graboski, M.S., and Daubert, T.E.,. (1978). *Modified Soave Equation of State for Phase-Equilibrium Calculations .2. Systems Containing Co2, H2s, N-2, and Co.*

GuoBiao C., Jian D., Yang Z., Nanjlia Y. (2016). Combustion Behaviors of GO2/GH2 Swirl-Coaxial Injector Using Non-Intrusive Optical Diagnostics. *Acta Astronautica*.

H, M. (2001). *Liquid-Fuel Droplet Vaporisation and Cluster Behavior at Supercritical Conditions.* Pennsylvania State University.

Haeseler D., Mading C., Preclik D. (2006). *LOX-Kerosene Oxidiser-Rich Gas-Generator and Main Combustion Chambers Subscale Testing.* AIAA 2006-5197.

Hersch, M. (1967). *Hydrogen-Oxygen Chemical Reaction Kinetics in Rocket Engine Combustion.* Washington D.C.: National Aeronautics and Space Administration.

Huo, H. (2011). *Large Eddy Simulation of Supercritical Fluid Flow And Combustion.* The Pennsylvania State University.

Immich H., Alting J., Kretschmer J. (2002). *Technologies for Thrust Chambers of Future Launch Vehicle Liquid Rocket Engines.* AIAA Paper 2002-4143.

Ivancic B., M. W. (2002). *Time- and Length Scales of Combustion in Liquid Rocket Thrust Chambers.*

Kim P., M. J. (1981). *Numerical Investigation of Turbulent Channel Flow.*

Koretsky, M. (2004). *Engineering and Chemical Thermodynamics.*

Lafon P, Y. V. (1995). Pressure-Coupled Vaporisation and Combustion Responses of Liquid Oxygen (Lox) Droplets in Supercritical Hydrogen Environments. *AIAA, ASME, SAE and ASEE Joint Propulson Conference and Exhibit, 31st, San Diego, United States*.

Leonard, A. (1974). Energy Cascade in Large-Eddy Simulations of Turbulent Fluid Flows.

Lilly, D. (1992). A Proposed Modification of the Germano-Subgrid-Scale Closure Method.

Locke J. (2011). *High Speed Diagnostics For Characterisation of Oxygen/Hydrogen Rocket Injector Flowfields.*

Marshall W.M., Pal S., Woodward R., Santoro R.J. (2005). *Benchmark Wall Heat Flux Data for a GH2/GO2 Single Element Combustor.* American Institute of Aeronautics and Astronautics.

Mcbride B.J., G. S. (1996). *Computer Program for Calculation of Complex Equilibrium Compositions and Applications.* NASA Reference Publ. 1311.

Menon, N. (2008). *Analysis of Non - Axisymmetric Underexpanded jet flow fields.* Johannesburg: University of the Witwatersrand.

Miller R., Harstad K., Bellan J. (2001). Direct Numerical Simulations of Supercritical Fluid Mixing Layers Applied to Heptane-Nitrogen. *Journal of Fluid Mechanics*.

Moin P., Mahesh K. (1998). Direct Numerical Simulation: A Tool in Turbulence Research. *Journal of Fluid Mechacanics, Vol 118*.

Murakami E., Papamoschou D. (2002). *Mean Flow Development in Dual-Stream Compressible Jets.*

Murrone, A.; Fdida, N.; Le Touze, C.; L., Vingert. (2014). *Atomisation of cryogenic rocket engines coaxial injectors - Modeling aspects and experimental investigations.*

O'Conaire M., Curran H., Simmie J.M., Pitz W.J., Westbrook C.K. (2004). A Comprehensive Modeling Study of Hydrogen Oxidation. *Wiley Interscience*.

Okong'o N.;Hardstad K.;Bellan J. (2002). Direct Numerical Simulation of O2/H2 Temporal Mixing Layers under Supercritical Conditions. *AIAA* .

Pal S., Marshall W., Woodward R., Santoro R. (2006). *Wall Heat Flux Measurements for a Uni-Element GO2/GH2 Shear Coaxial Injector.* Vernon, France: Third International Workshop on Rocket Combustion Modeling.

Ping J., Mao L., Guobiao C. (2013). Experimetnal Study of Hydrogen-Rich/Oxygen-Rich Gas-Gas Injectors. *Chinese Journal of Aeronautics*.

Piomelli U., Balaras E. (2002). Wall-Layer Models for Lare Eddy Simulations. *Annual Review of Fluid Mechanics*.

Poling, B., Prausnitz, J., & J.P.O'Connell. (2001). *The Properties of Gases and Liquids, 5th Edition.* New York: McGraw Hill.

Pomelli, U. (1999). Large Eddy Simulation: Achievements and Challenges.

Pope, S. (2000). *Turbulent Flows.*

Rehab H., Villermaux E., Hopfinger E.J. (1997). *Flow Regimes of Large-Velocity-Ratio Coaxial Jets.*

Ribault, C. L. (1999). Large Eddy Simulation of a Plane Jet. *Physics of Fluids*.

Ribert G., Zong N., Yang V., Pons L., Darabiha N., Candel C. (2008). Counterflow Diffusion Flames of General Fluids: Oxygen/Hydrogen Mixtures. *Combustion and Flame*.

Roache P.J. (1998). Verification and Validation in Computational Science and Engineering. New Mexico.

Roth C., H. O. (2015). *Comparison of different modeling approaches for CFD simulations of a single - element GCH4/GOX rocket combustor.* Munchen: Institute for Flight Propulsion, Technische University Munchen.

Sagut, P. (2001). *Large Eddy Simulations for Incompressible Flows: An Introduction.*

Schadow K.;Gutmark E. (1992). Combustion Instability Related to Vortex Shedding in Dump Combustors and Their Passive Control. *Progress in Energy Combustion Sciences*.

Schumaker S., Driscoll J.F.,. (2006). *Rocket Combustion Properties for Coaxial Injectors Operated at Elevated Pressures.*

Siemens. (2019). *STAR-CCM+ User Guide V13.06.011*. Retrieved from Siemens Product Lifecycle Management Software Inc.: https://thesteveportal.plm.automation.siemens.com

Smagorinsky, J. (1963). General Circulation Experiments with the Primitive Equations. I-the Basic Experiment.

Soteriou M.C., Ghoniem A.F. . (1995). *Effects of the Free-Stream Density Ratio on Free and Forced Spatially Developing Shear Layers.*

Sozer E., Vaidyanathan A., Segal C., Shyy W. (2009). Computational Assessment of Gaseous Reacting Flows In Single Element Injector. *AIAA*.

Spalart, P. (2009). Detached Eddy Simulation.

Tamura H., Sakamoto H., Takahashi M. (1997). *LOX/H2 Subscale Swirl Coaxial Injector Testing.* AIAA Paper 1997-2906,.

Thakur S., Wright J. (2012). *Simulation of a Shear Coaxial GO2/GH2 Rocket Injector with DES and LES Using Flamelet Models.*

Trask N. ,Perot J.B. ,Schmidt D.P. . (2009). *Modeling of the Internal Two-Phase Flow in a Gas-Centered Swirl Coaxial Fuel Injector.*

Tucker P.K., Menon S., Merkle C.L., Oefelein J.C., Yang V. (2008). *Validation of High - Fidelity CFD Simulations for Rocket Injector Design.*

Turns, S. (2000). *An Introduction to Combustion: Concepts and Application.*

Vaidyanathan R., Tucker P.K., Shyy W. (2003). *CFD-Based Design Optimisation for a Single Element Rocket Injector.* AIAA 03-0296, 41st AIAA Aerospace Sciences Meeting.

Vallet, A. (2009). *Mod´elisation Eulerienne de L'atomisation d'un Jet Liquide.*

Vervisch L., Poinsot T. (1998). Direct Numerical Simulation of Non-Premixed Turbulent Flames. *Annual Review of Fluid Mechanics*.

Villermaux E., Rehab E. (2000). *Mixing in Coaxial Jets.*

W. Calhoon, S. M. (1996). Subgrid Modeling for Reacting Large Eddy Simulations. *Aerospace Sciences Meeting and Exhibit*.

Wang X. ,Cai G., Gao Y., Jin P. (2009). *Large Flow rate Shear-Coaxial Gas-gas Injector.*

Wang X., Cai G., Huo H.,. (2012). *Numerical study of high-pressure GO2/GH2 combustion of a single-element injector.*

White, C. (2003). *Modeling of Circulation Zone and Shear Layers in Coaxial Injectors.* Knoxville: University of Tennessee.

XiaoWei W.;GuoBiao C.;YuShan G.;HongFa H.;. (2011). High flowrate injector with gaseous hydrogen and gaseous oxygen. *Science China*.

Yang, V. (2004). *Liquid-Propellant Rocket Engine Injector Dynamics and Combustion Processes at Supercritical Conditions.*

Zang, Y., Street, R., & Koseff, J. (1993). A Dynamic Mixed Subgrid - Scale Model and Its Application to Turbulent Recirculating Flows. *Physics of Fluids*.

Zhukov, V. (2015). Computational Fluid Dynamics Simulations of GO2/GH2 Single Element Combustor. *JOurnal of Propulsion And Power*.

Zong N., Yang V. (2007). Near-Field Flow and Flame Dynamics of Lox/Methane Shear-Coaxial Injector under Supercritical Conditions. *Proceedings of the Combustion Institute*.

Appendix A: Shear Coaxial Injector with Recess Length

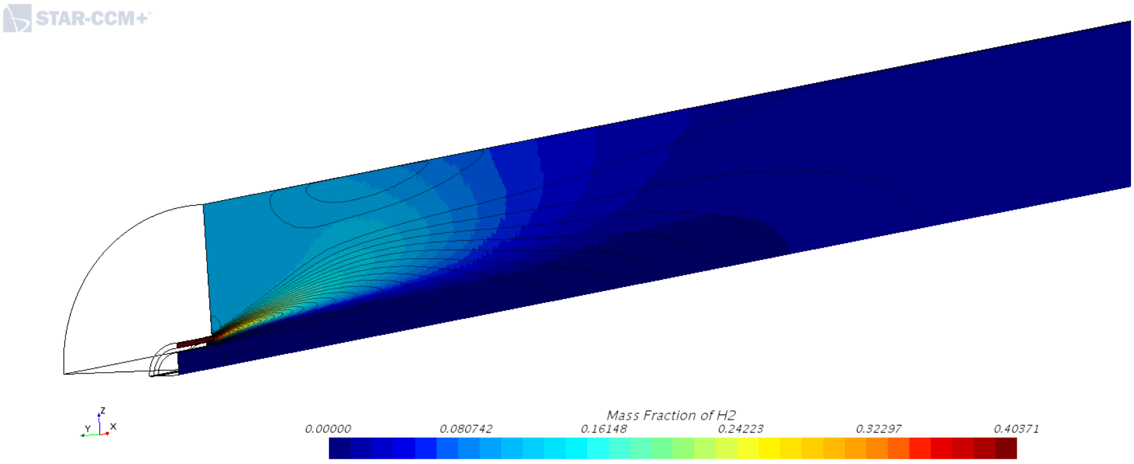

Figure A.1: Hydrogen concentration profile of the 30% recess length while maintaining the base case momentum ratio.

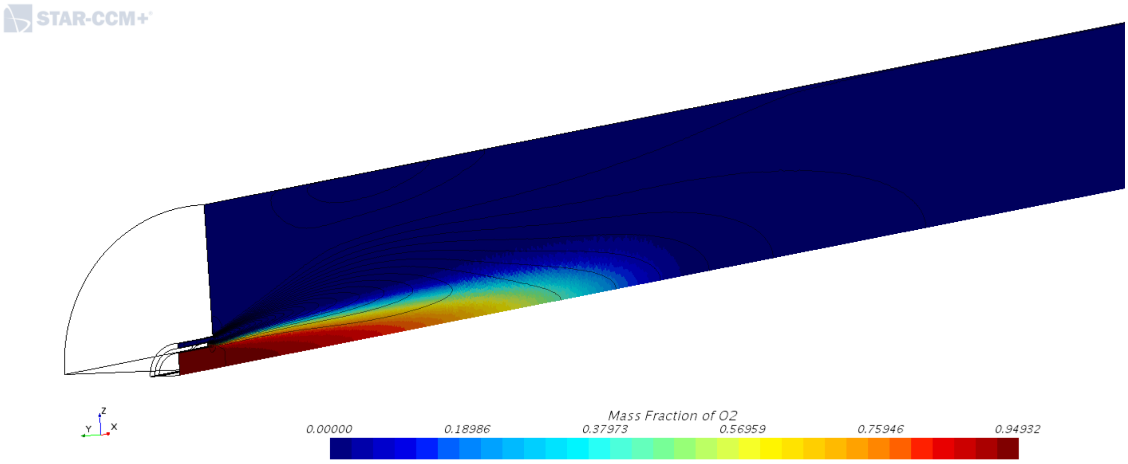

Figure A.2: Oxygen concentration profile of the 30% recess length while maintaining the base case momentum ratio.

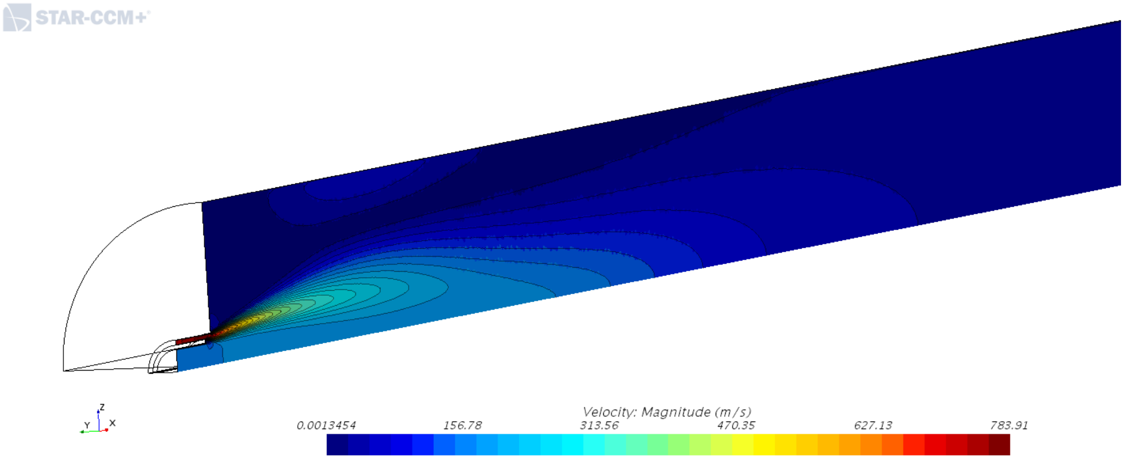

Figure A.3: Velocity magnitude profile of the 30% recess length while maintaining the base case momentum ratio.

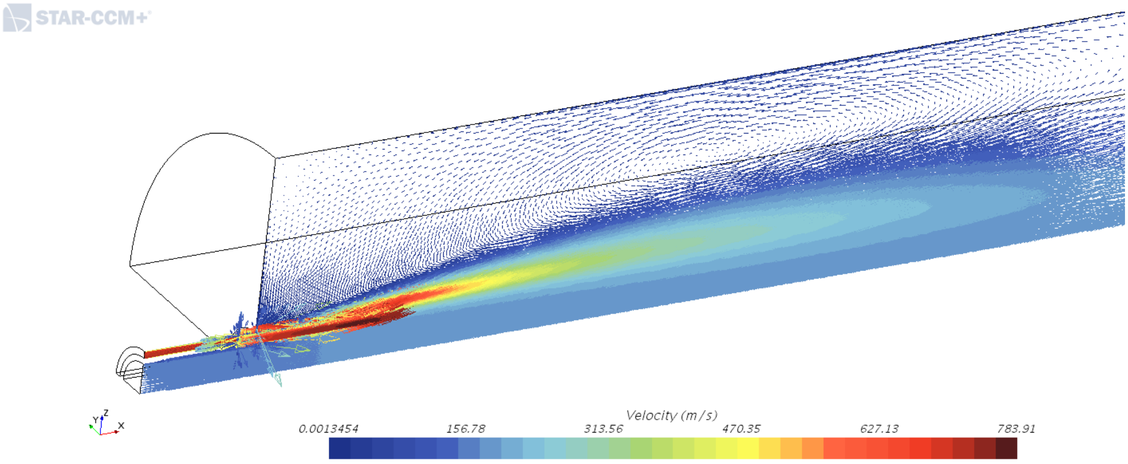

Figure A.4: Velocity vector profile of the 30% recess length while maintaining the base case momentum ratio.

Appendix B: Swirl Coaxial Injector

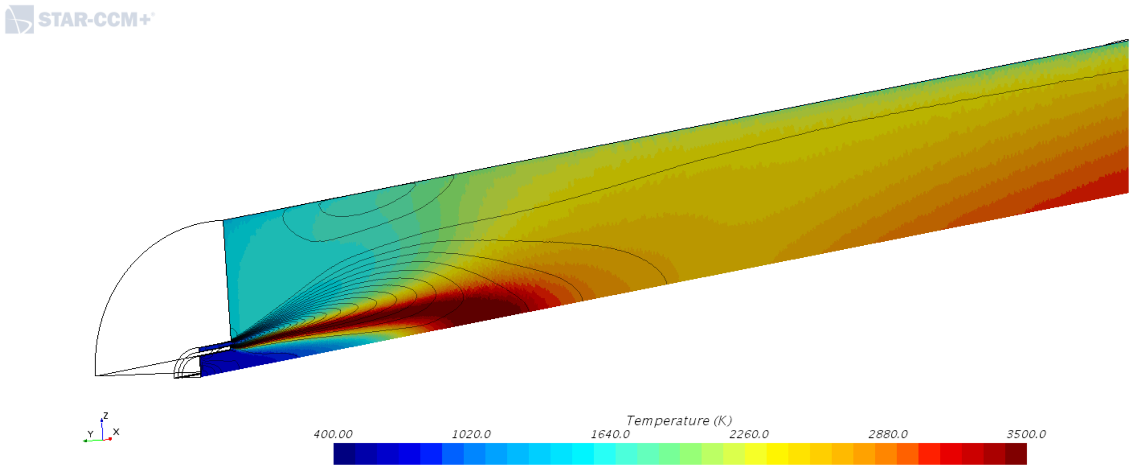

Figure B.1: Temperature profile of the swirl test case while maintaining the base case momentum ratio.

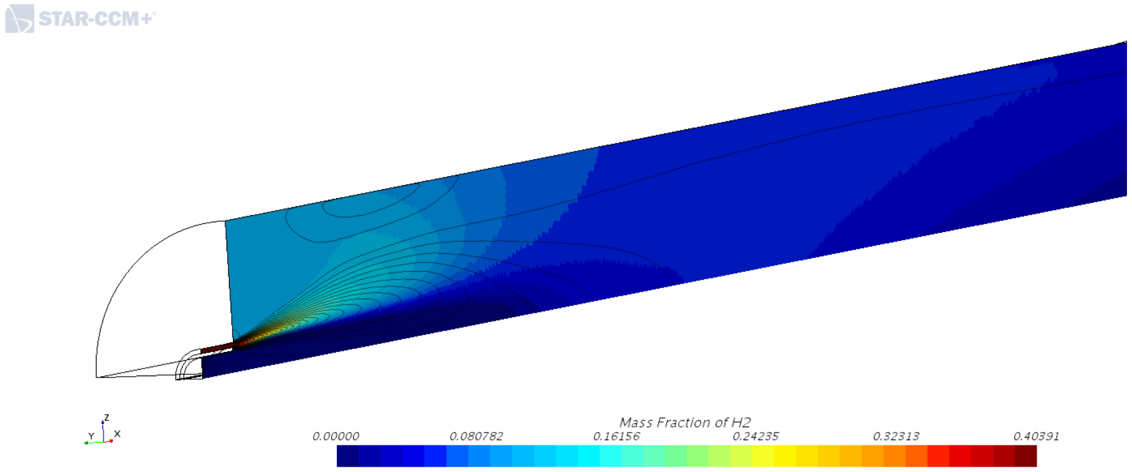

Figure B.2: Hydrogen concentration profile of the swirl test case while maintaining the base case momentum ratio.

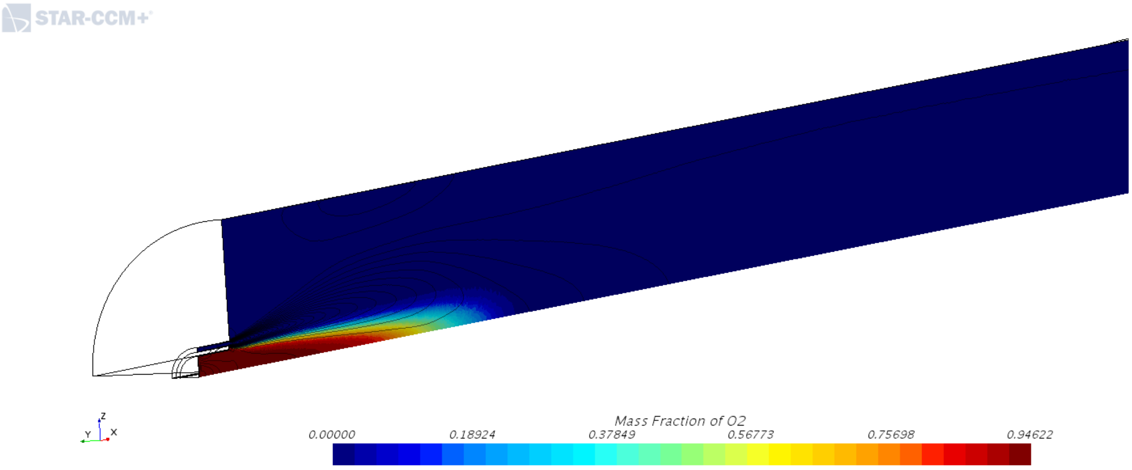

Figure B.3: Oxygen concentration profile of the swirl test case while maintaining the base case momentum ratio.

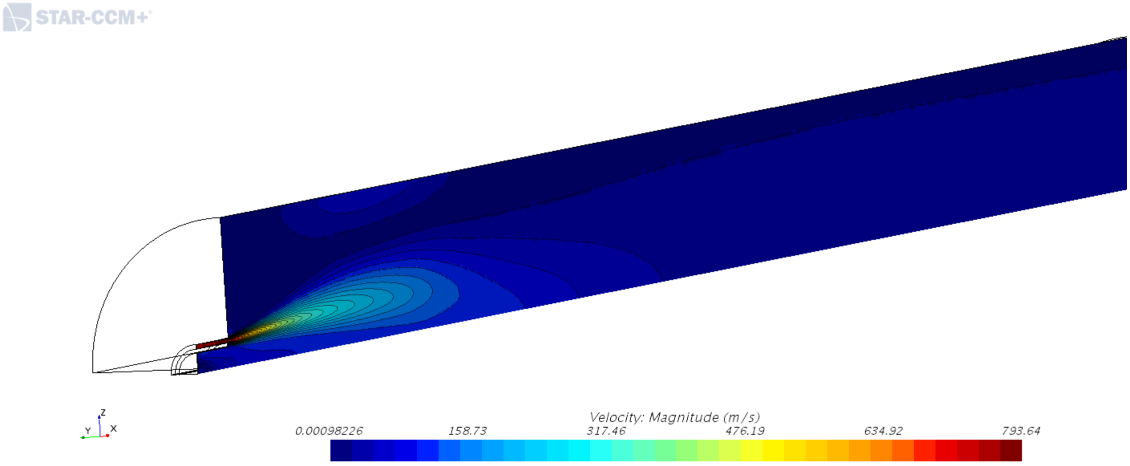

Figure B.4: Velocity magnitude profile of the swirl test case while maintaining the base case momentum ratio.

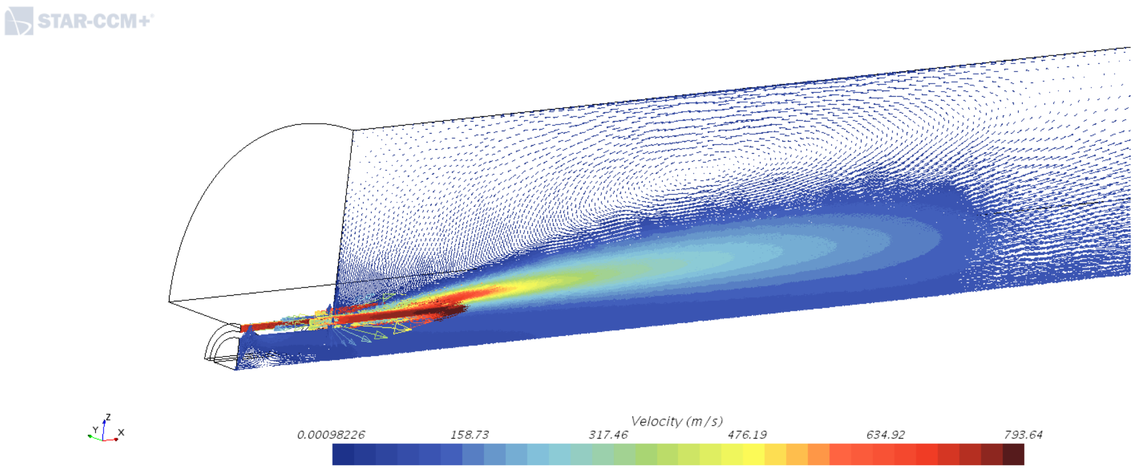

Figure B.5: Velocity vector profile of the swirl test case.